

Dissertation
submitted to the
Combined Faculties for Natural Sciences and Mathematics
of the Ruperto-Carola University of Heidelberg, Germany
for the degree of
Doctor of Natural Sciences

Put forward by

Diplom-physicist: Elisabeth Kierig
Born in: Frankfurt a.M.
Oral examination: 20. Mai 2009

AC-Control of Single Particle Tunneling

Referees: Prof. Dr. Markus Oberthaler
Prof. Dr. Jian-Wei Pan

Kontrolle der Tunneldynamik einzelner Atome

Das Ziel Quantensysteme in ihren internen und externen Freiheitsgraden zu kontrollieren ist für viele Bereiche der Physik und Chemie von großer Bedeutung. Starke, zeitlich veränderliche, externe Felder eröffnen die Möglichkeit eine solche kohärente Kontrolle zu realisieren.

In dieser Arbeit wird die experimentelle Realisierung eines Modell-Systems vorgestellt. Es wird demonstriert, wie mit Hilfe eines zeitlich periodischen, externen Feldes die Tunneldynamik einzelner Atome kontrolliert werden kann. In Abhängigkeit der Parameter des Treibens kann die Höhe der Tunnelrate gesteuert werden, im Extremfall bis hin zur kompletten Unterdrückung des Tunnelprozesses. Diese Art dynamischer Lokalisierung ist als “coherent destruction of tunneling” bekannt.

Der experimentelle Aufbau ermöglicht einen sehr direkten Zugang zur Tunneldynamik einzelner Atome in einem Doppeltopfsystem und lässt große Freiheit bei der Wahl der Parameter. So können nicht nur Doppeltopfpotential, Treibefrequenz und -amplitude, sondern auch die zeitliche und räumliche Symmetrie des Treibens variiert werden. Als Teilchenquelle dient ein kohärenter Strahl langsamer metastabiler Argonatome, die räumlich aufgelöst detektiert werden, was die direkte Beobachtung ihrer Tunneldynamik im Impulsraum ermöglicht.

AC-Control of Single Particle Tunneling

The aim to control the internal and external degrees of freedom of quantum systems is of great interest for many fields of physics and chemistry. One opportunity to realize such a coherent control is provided by strong, time depended, external fields.

In this work the experimental realization of a model-system is presented. The coherent control of the tunneling dynamics of single atoms by means of a time-periodic, external field is demonstrated. Depending on the parameters of the driving force the tunneling rate can be varied up to a total suppression of the tunneling process in the extreme. This type of dynamical localization is known as “coherent destruction of tunneling”.

The experimental setup allows a direct access to the tunneling dynamics of single atoms in a double well structure and enables great freedom concerning the parameters. Not only the double well potential, the driving frequency and the driving amplitude can be varied, but also the temporal and spatial symmetry of the driving. A coherent beam of slow, metastable argon atoms serves as source of particles, which can be detected spatially resolved enabling the direct observation of the tunneling dynamics in momentum space.

To my parents
To Stefan & Arthur

Contents

1	Introduction	5
2	Theoretical description of a strongly driven quantum system	9
2.1	Double well system	10
2.1.1	Light shift potentials	11
2.1.2	Atom-light coupling	13
	Asymmetry	17
2.2	Time evolution of an atom in an unperturbed double well potential .	18
2.2.1	Initial state	20
2.2.2	Near field measurements	21
2.2.3	Bragg Diffraction	24
2.3	Introducing time-dependent driving-field	24
2.3.1	Floquet approach	26
2.3.2	Symmetry dependence of CDT	32
2.3.3	Two-mode approximation	33
2.3.4	Split-step Fourier method	35
2.3.5	Comparing different methods	39
3	Experimental realization of ac-control of single atoms	43
3.1	Experimental setup	43
3.1.1	Coherence of the atomic beam	45
3.1.2	Detection	46
3.2	Double well structure	46
3.2.1	Working with a real mirror	49
3.3	Single particle tunneling	50
3.3.1	Bragg Scattering	51
3.3.2	Adiabaticity	51
3.3.3	Imaginary potential	52
3.3.4	Potential heights	53
3.3.5	Symmetry of the double well potential	54
	Influence of the AOD frequency onto the tunneling time . . .	55
3.3.6	First visualization of single particle tunneling	56
3.3.7	First systematic measurements	56

3.4	AC-driving	58
3.4.1	Frequency dependence	59
3.4.2	Breaking symmetry of the driving	60
3.4.3	Amplitude dependence	60
4	Non-spreading wave packets in imaginary potentials	63
5	Conclusion	69
A	Creating a coherent beam of slow atoms	73
	Bibliography	83

Chapter 1

Introduction

For quantum physics it was a long way from the first theoretical ideas developed in the beginning of the twentieth century until today's sophisticated techniques to manipulate light and matter. Still it remains a vital field of research especially as new techniques enable fundamental studies of quantum effects as well as initiate new technologies. For example the union of quantum mechanics and information science does not only try to make use of quantum mechanical phenomena for computation, but also has allowed great advances in the understanding of the quantum world and in the ability to control coherently individual quantum systems [1, 2]. Furthermore many topics of quantum mechanics as quantum chaos, coherence, transport etc. connect disparate branches of physics like quantum optics and solid state physics or even chemistry or biology making it an even more attractive field to work on.

It took only a few years from de Broglie's pioneering hypothesis stating that any moving particle had an associated wave - an idea he worked out in his thesis [3] and for which he won the Nobel Prize in Physics in 1929 - until its experimental verification. However this was only a starting point to a new field in physics that was especially pushed by the development of laser systems, which enable a rather direct experimental access to the quantum mechanics of atoms. Many schemes for cooling atoms were and still are developed [4] and with the experimental realization of a Bose-Einstein condensate [5, 6] and another Nobel prize for its creators even macroscopic matter-waves, sometimes called a "super atom", can now be studied.

Crucial about atom optics is that the roles of matter and light as they are classically known from optics are reversed. On the one hand interference effects, dispersion, diffraction etc. are also properties of matter due to its wave character, on the other hand the possibility to exert a force on particles with light enables the realization of lenses, mirrors, or beam splitters like crystals of light. An overview of this can be found among others in [7].

One of the most fundamental and astonishing effects of quantum theory is the tunneling of material particles through a classically impenetrable barrier. It was originally proposed by Hund [8] to explain the ammonium spectrum and employed in many modern technologies like Josephson junctions [9, 10] and SQUIDS [11],

Zener diodes or the scanning tunneling microscopes [12] as well as in nature, where many processes would not work without it, i.e., one of the most important biochemical processes, namely the photosynthesis [13, 14]. Neither would there be α -decay nor could the nitrogen atom in ammonia molecules flip-flop through the triangle of hydrogen atoms. But even though quantum tunneling has found its way into technology, is well understood and can be calculated exactly, there is no direct way to control or manipulate the tunneling dynamics of a particles.

Control is a widespread topic in the context of quantum states. The aim to control the internal and external degrees of freedom of atoms and molecules is addressed in many different fields [15]. The first move to coherently control the quantum states of atoms and molecules was done by I.I. Rabi, who introduced radio-frequency resonance techniques to molecular beams in 1938 [16]. In chemistry there exists the field of “femtochemistry” trying to control chemical reactions via ultrashort laser pulses. This technique, in which one tries to find the appropriate sequence of laser pulses needed to break a specific chemical bond, is also known as coherent control.

Coherent control of qubits is an important topic in quantum information as one of the major problems of realizing a quantum computer is keeping all components in a coherent state. There exist many different proposals for the stabilization of the coherence. For example Weihnacht et al. [17] report on the active manipulation of the shape of an atomic electron’s radial wave. Using a computer-controlled laser the quantum state is reshaped until it matches the target by reconstructing the wave function employing a variation of quantum holography and feeding this information back into the laser control system. Among others a theoretical approach by Fonseca-Romero et al. [18] points out a possible coherence stabilization scheme for a two-qubit gate employing an ac-field. Strong, time-periodic, external fields as in the latter example certainly represent an important method for controlling quantum systems [19].

The work at hand focusses on the role of time-dependent driving on the coherent tunneling process of a massive particle between two locally stable potential wells. Such a symmetric double well structure is the ideal candidate to study quantum tunneling and the effects of strong driving. Atom optics offers the straightforward experimental realization of such a model system utilizing light-shift potentials. That way the tunneling of single atoms can directly be observed in momentum space.

The Floquet formalism allows the solution of the time-dependent Schrödinger equation for such time periodic quantum systems. Analogues to the Bloch theorem for systems periodic in space the solutions, so-called Floquet-states, are a product of a time-periodic state-vector and a time-dependent phase factor. Quasienergies then substitute to some extent the eigenenergies of an autonomous systems. But they do only carry phase information and do not have the meaning of an absolute energy as they are only defined except for multiples of the driving field quantum and therefore can be mapped into a zone analogous to the first Brillouin zone known from solid state physics. This formalism bears the great advantage that it does not restrict the driving parameters and gives a descriptive access, allowing a full analysis of the experiments described in this work.

A very intriguing result of the Floquet analysis of such a double well system was pointed out by Hänggi and coworkers in 1991 [20], namely the so called effect of coherent destruction of tunneling (CDT). They found that for appropriately chosen parameters the driving would prevent any dynamics in the system, i.e., localizing the wavepacket in one well, which is astonishing, as the tunneling-effect is an intrinsic characteristic of the quantum world. A visualization of dynamical localization and CDT in curved waveguides was reported by Longhi et al. [21] and Della Valle et al. [22] respectively. A closely related effect in a periodic potential has been observed in the nonlinear dynamics of a Bose-Einstein condensate by Arimondo and coworkers [23].

Apart from slowing it is also possible to achieve an acceleration of the tunneling dynamics via ac-driving. In this context there exists work done by Steck et al. [24], who found that the tunneling rate between two stable islands in phase space can be enhanced by the presence of chaos in the corresponding classical dynamics, which is not only interesting in the context of control, but also gives fundamental insights into the relation between classical chaos and quantum mechanics.

In conclusion the ac-field should enable a full control of the tunneling dynamics of atoms in a double well potential.

Outline

This thesis consists of two parts, the first one giving the theoretical background for the experiments and a second one, in which the realization is described and the results are presented. In the theoretical part the time-independent double well structure is characterized before the consequences of the time dependence introduced by the added driving field are discussed. Especially the effect of coherent destruction of tunneling is explained and particular attention is paid to the differences between the model system to study this effect proposed by Grossmann et al. [20] and the experimentally realized one. Furthermore this chapter deals with different methods, that were employed to simulate the experimental reality.

In the second part the setup is discussed and all steps of the experiment are described in detail. The first topic is the implementation of a double well structure enabling adiabatic preparation of the ground state of the potential. Then the preparation process of a localized wave packet on one side of a double well is illustrated, before presenting the first measurements of single particle tunneling in the static potential. This is basis and starting point to study the influence of an external driving field on the dynamics of an atom in such a potential. Systematic measurements demonstrating coherent control of the quantum tunneling of massive particles are presented. Furthermore the results of measurements concerning the symmetry a discussion of the observation of the effect of CDT.

Thereafter a summary of an experiment realizing a non-spreading wavepacket is added. It is another experiment in the context of controlling quantum systems. Here it is the shape and the dispersion of a wave-packet that is actively controlled via an imaginary potential. The experiment is discussed in detail in the work of

Ralf Stützle [25] and Martin Göbel [26] and was performed during the first year of my PhD period.

At last a rough overview of the assembly to produce a coherent beam of slow argon atoms, which is the basis of the experiments is given in the appendix. This is only for completeness as there are many other works describing the setup in all its details.

Chapter 2

Theoretical description of a strongly driven quantum system

The development of laser systems opened new possibilities to interact with particles like atoms or molecules. A whole new branch of physics was created, namely the atom optics, that allowed new insight into the nature of such quantum systems. Especially the detailed dynamics of quantum systems exposed to time-dependent external fields is actively discussed by theorists as well as experimentalists. Such explicitly time-dependent quantum systems are rarely solvable exactly, but a variety of new phenomena can be observed.

This work deals with the intention to utilize a strong time-periodic external driving field to fully control the dynamics of a quantum mechanical system. The explicit time-dependence of the Hamiltonian makes it unaccessible within ordinary stationary quantum mechanics. Nevertheless a time-periodic driving field enables an ansatz using the Floquet-theorem to solve the time-dependent Schrödinger equation. This ansatz has the great advantage compared to commonly used perturbation theory that it does not make any restrictions concerning amplitude or frequency of the periodic or even only quasi periodic driving field.

Concerning the driving frequency different regimes can be distinguished. For very fast and very slow driving, when the inner timescales of the inherent dynamics of the unperturbed system and the external periodic driving are clearly separated, the two processes effectively uncouple. This yields a dynamics resembling that of the undriven case, whilst in the regime of intermediate driving frequencies the dynamics may deviate strongly.

Following the Floquet ansatz an intriguing result was found for the tunneling dynamics of an atom in a double well potential, namely, that an appropriately designed coherent cw-drive can not only manipulate the tunneling time but completely prevent the tunneling dynamics. This effect predicted by Hänggi et al. is known as coherent destruction of tunneling (CDT) [20].

As the effect of CDT and the paper mentioned above were the kick-off for the experiments described in this work the theoretical part follows their considerations,

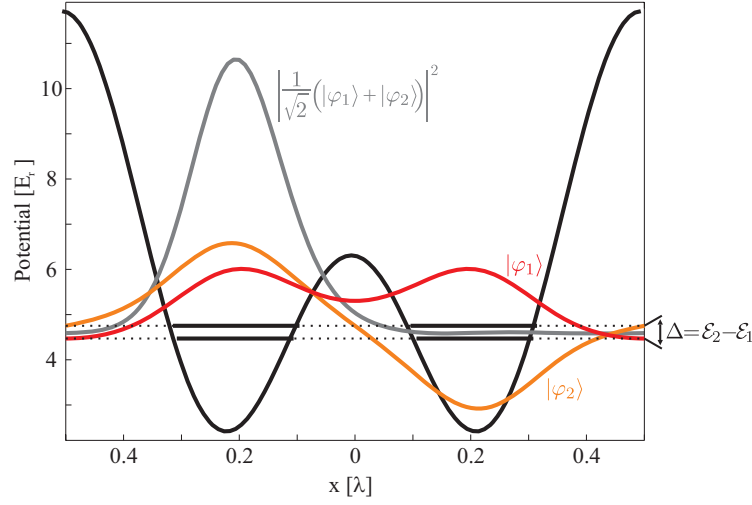


Figure 2.1: A double well potential is plotted with its lowest eigenstate doublet consisting of the symmetric state $|\varphi_1\rangle$ and the antisymmetric state $|\varphi_2\rangle$. The corresponding eigenenergies are indicated by horizontal lines and the localized state $\langle l|l\rangle = |\frac{1}{\sqrt{2}}(|\varphi_1\rangle + |\varphi_2\rangle)|^2$ is added. The units for the potential and the position x correspond to a realization via a light shift potential as will be described in the following. For the light with wavelength λ , the energy \mathcal{E}_r is the one-photon recoil energy an atom experiences (cf. eq. 2.21).

whereat the aim is to draw the direct connection to the experimental realization. The chapter is roughly split into two parts. The time evolution of an atom in an undriven double well potential is discussed in the first part. Then a time dependent driving field is introduced and analytical as well as numerical methods are described to solve the corresponding Schrödinger equation.

2.1 Double well system

The archetype system to study the fundamental and rather not intuitive effect of massive particle tunneling is a double well potential as depicted in fig. 2.1. A particle localized in one of the two wells of such a potential will be found in the other after some reasonable time, even though it does not carry the energy to classically overcome the barrier in the middle. This time it takes a particle to tunnel through the barrier can be calculated very straightforward by looking at the eigenstates of the double well potential. Those eigenstates form doublets each consisting of one symmetric and one antisymmetric state. The lowest doublet is depicted in red and orange in fig. 2.1. Hence it is obvious that a particle localized on one side of such a double well potential can be described utilizing only the ground state doublet,

namely as the sum or difference of the two lowest states $|\varphi_1\rangle$ and $|\varphi_2\rangle$:

$$\begin{aligned} |l\rangle &= \frac{1}{\sqrt{2}}(|\varphi_1\rangle + |\varphi_2\rangle) \\ |r\rangle &= \frac{1}{\sqrt{2}}(|\varphi_1\rangle - |\varphi_2\rangle), \end{aligned} \quad (2.1)$$

so that the time evolution of the ground state doublet yields the time evolution, i.e., the dynamics, of the particle:

$$|\psi\rangle_{\pm}(t) = \frac{1}{\sqrt{2}} \left(\exp(-i\frac{\mathcal{E}_1}{\hbar}t) |\varphi_1\rangle \pm \exp(-i\frac{\mathcal{E}_2}{\hbar}t) |\varphi_2\rangle \right). \quad (2.2)$$

Thus for a particle localized in the left well at time $t = 0$ the probability to find it in the right well is given by the projection of its wave function $|\psi_+(t)\rangle$ onto the state $|r\rangle$:

$$\begin{aligned} |\langle\psi_+(t)|r\rangle|^2 &= \left| \frac{1}{\sqrt{2}} \exp\left(i\frac{\mathcal{E}_1}{\hbar}t\right) \left(\langle\varphi_1|r\rangle + \exp\left(i\frac{\mathcal{E}_2 - \mathcal{E}_1}{\hbar}t\right) \langle\varphi_2|r\rangle \right) \right|^2 \\ &= \left| \frac{1}{\sqrt{2}} \exp\left(i\frac{\mathcal{E}_1}{\hbar}t\right) \left(\frac{1}{\sqrt{2}} - \exp\left(i\frac{\mathcal{E}_2 - \mathcal{E}_1}{\hbar}t\right) \frac{1}{\sqrt{2}} \right) \right|^2 \\ &= \frac{1}{4} \left| 1 + \exp\left(i\frac{\mathcal{E}_2 - \mathcal{E}_1}{\hbar}t\right) \right|^2 \\ &= \frac{1}{2} + \frac{1}{2} \cos\left(\frac{\Delta}{\hbar}t\right). \end{aligned} \quad (2.3)$$

This $\Delta = \mathcal{E}_2 - \mathcal{E}_1$ introduced in the last line is called the tunneling splitting as it defines the tunneling time:

$$T_t = \frac{2\pi\hbar}{\Delta}. \quad (2.4)$$

The experiments and the theoretical considerations described in the following are aimed at the control of this tunneling rate by means of an external field, i.e., without changing the basic characteristics of the double well potential like the barrier height and thus the energies \mathcal{E}_1 or \mathcal{E}_2 . A full control should maintain the possibility to either accelerate the tunneling dynamics or even to totally inhibit it, thus to realize CDT, which implies the realization of a dynamically localized quantum state.

2.1.1 Light shift potentials

In the theoretical prediction of the effect of coherent destruction of tunneling [20] the model system is a quartic double well potential, namely $H(x, t) = \frac{p^2}{2} - \frac{x^2}{4} + \frac{x^4}{64D}$, with the characteristic quantities barrier height $D = \frac{E_B}{\hbar\omega_0}$ in units of $\hbar\omega_0$ and the angular frequency ω_0 of harmonic oscillations on the bottom of each well. In the experiment described here it was plausible to choose a slightly different realization, namely a periodic arrangement of double well potentials generated by adding two

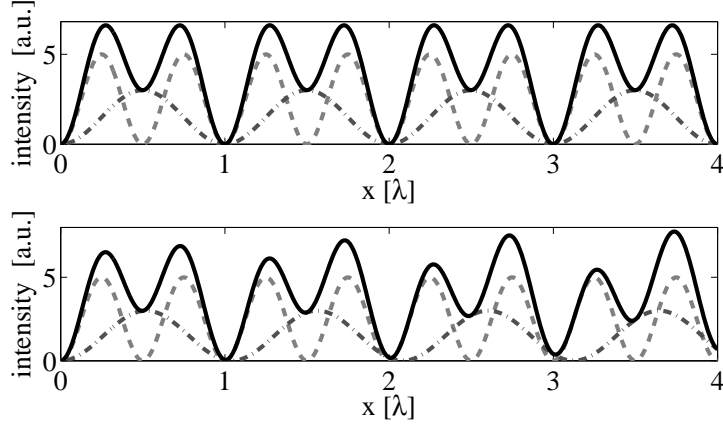


Figure 2.2: The upper plot shows an inverse continuous double well structure (black line) as result of adding two standing light waves with wavelengths λ_1 (light gray, dashed) and $\lambda_2 = 2 \cdot \lambda_1$ (dark gray, dot and dash). In the lower plot the wavelength λ_2 is not exactly twice λ_1 resulting in an asymmetry of the reversed double wells that depends on their position.

red detuned standing light waves with wavelength λ_1 and $\lambda_2 = 2\lambda_1$ and amplitudes E_1 and E_2 as depicted for the corresponding intensities in the upper plot of fig. 2.2. The electro-magnetic field for the region all light waves overlap reads:

$$\begin{aligned}
 E(x, t) &= E_1 \sin(k_1 x - \omega_1 t) + E_1 \sin(-k_1 x - \omega_1 t + \pi) \\
 &\quad + E_2 \sin(k_2 x - \omega_2 t) + E_2 \sin(-k_2 x - \omega_2 t + \pi) \\
 &= 2E_1 \sin(k_1 x) \cos(\omega_1 t) + 2E_2 \sin(k_2 x) \cos(\omega_2 t)
 \end{aligned} \tag{2.5}$$

in which π is the phase shift the reflected light wave experiences at a perfect conductive mirror. In the case of the chosen gold mirror, as for any real mirror, this is not completely true, yielding a constant phase shift between the two standing waves and therewith introducing some problems addressed in the experimental part of this work (cf. sec. 3.2 and sec. 3.3.5). For now it is enough to consider an ideal mirror.

The intensity of the light wave results in:

$$\begin{aligned}
 I(x, t) &= c\epsilon_0 |A(x, t)|^2 \\
 &= c\epsilon_0 \left(4E_1^2 \sin^2(k_1 x) \cos^2(\omega_1 t) + 4E_2^2 \sin^2(k_2 x) \cos^2(\omega_2 t) \right. \\
 &\quad \left. + 8E_1 E_2 \sin(k_1 x) \sin(k_2 x) \cos(\omega_1 t) \cos(\omega_2 t) \right) \\
 &= c\epsilon_0 \left(4E_1^2 \sin^2(k_1 x) \cos^2(\omega_1 t) + 4E_2^2 \sin^2(k_2 x) \cos^2(\omega_2 t) \right. \\
 &\quad \left. + 4E_1 E_2 \sin(k_1 x) \sin(k_2 x) [\cos((\omega_1 + \omega_2)t) + \cos((\omega_1 - \omega_2)t)] \right).
 \end{aligned} \tag{2.6}$$

In the experiment the wavelength λ_1 is chosen to be 811nm, and the frequency ω_2 is shifted by $\omega_{\text{AOD}} \approx 2\pi \cdot 40\text{MHz}$ in respect to ω_1 . Therewith the time dependence of the first two terms of the last result oscillate with a period in the range of femtoseconds, so does the term containing the sum of the two frequencies $\omega_1 + \omega_2$. For the very last term containing the difference of the two frequencies the chosen parameters yield an oscillation with a period of some nanoseconds. All these oscillations are fast compared to the experimental time scales, where an atom needs about a millisecond to tunnel through the middle barrier of a double well and the driving frequencies are in the same range of some kHz, i.e., milliseconds. Hence averaging over typical timescales $t > \frac{2\pi}{\omega_{\text{AOD}}}$ yields an intensity profile for the electro-magnetic field (with $k = k_1$ and hence $k_2 = \frac{k}{2}$):

$$I(x) = c\epsilon_0(4E_1^2 \sin^2(kx) + 4E_2^2 \sin^2(\frac{k}{2}x)), \quad (2.7)$$

which resembles a continuous row of reversed double wells as shown in the upper picture of fig. 2.2.

If the wavelength λ_2 of the second standing light wave is not exactly twice λ_1 they add up forming a row of asymmetric reversed double wells, whose asymmetry depends on their distance from the mirror surface as depicted in the lower plot of fig. 2.2. The intensity profile than reads:

$$I(x) = c\epsilon_0(4E_1^2 \sin^2(kx) + 4E_2^2 \sin^2(k \cdot (0.5 + \delta) \cdot x)). \quad (2.8)$$

2.1.2 Atom-light coupling

In this section a general concepts to describe the coupling between atoms and light is introduced enabling the detailed analysis of the tunneling system in the following. The whole system will be treated in a semiclassical picture, as the radiation field may be assumed a classical c-number field, whilst the atom has to be considered quantum mechanically.

Starting from the classical picture, the Hamiltonian describing the whole system of an atom in a radiation field can be written as the sum of the kinetic energy of all electrons, the electrostatic energy of the whole atom, i.e., electrons plus nucleus, and the potential energy of the electromagnetic fields $\mathbf{E}(\mathbf{r}, t)$ and $\mathbf{B}(\mathbf{r}, t)$:

$$\begin{aligned} H = & \underbrace{\sum_{\alpha} \frac{1}{2m_{\alpha}} (\mathbf{p}_{\alpha} - \frac{q_{\alpha}}{c} \mathbf{A}(\mathbf{r}_{\alpha}, t))^2 + \frac{1}{2} \int d^3r \rho(\mathbf{r}) \phi(\mathbf{r}, t)}_{H_A} \\ & + \underbrace{\frac{\epsilon_0}{2} \int d^3r \{ \mathbf{E}(\mathbf{r}, t) + c^2 \mathbf{B}(\mathbf{r}, t)^2 \}}_{H_R}, \end{aligned} \quad (2.9)$$

where \mathbf{r}_{α} denotes the relative coordinates of the electrons with respect to the position \mathbf{R} of the nucleus. The kinetic energy of the nucleus is neglected as it is small

compared to the electrons. Furthermore the term H_R may also be dropped as for classical fields \mathbf{E} and \mathbf{B} it represents only a constant energy offset.

As the wavelength of the light is large compared to the dimensions of an atom, the light potential is assumed to be constant in the range of the atom, which combined with a unitary transformation into a rotating frame yields an extra term, called the electric dipole coupling term:

$$H_{ED} = -\mathbf{d} \cdot \mathbf{E}(\mathbf{R}, t) \quad (2.10)$$

Thus the Schrödinger equation of the coupled system becomes:

$$i\hbar \frac{\partial}{\partial t} |\psi\rangle = (H_A + H_{ED}) |\psi\rangle. \quad (2.11)$$

Now changing to the semiclassical description, the radiation field is still treated classically, i.e., considering a single-mode laser field, it can be written as:

$$\mathbf{E} = \mathbf{e}E_0 \cos(\omega t + \phi), \quad (2.12)$$

but the atom is described quantum mechanically. Thus the term H_A denoting the time independent Hamiltonian of the atomic structure is determined by the eigenstates and eigenvectors of the atom: $H_A |\phi_n\rangle = \hbar\omega_n |\phi_n\rangle$ and the state vector can be expanded in those base states:

$$|\psi\rangle = \sum_n c_n(t) e^{-i\omega_n t} |\phi_n\rangle. \quad (2.13)$$

For a two-level atom with ground state $|g\rangle$ and excited state $|e\rangle$ with an energy difference of $\hbar\omega_0$ between them, and introducing the Rabi frequency Ω_R :

$$\Omega_R(x) = -\frac{\langle e | \mathbf{d} | g \rangle \cdot \mathbf{e}E_0(x)}{\hbar} e^{i\phi}, \quad (2.14)$$

the Schrödinger equation yields the two differential equations:

$$\begin{aligned} i\hbar \dot{c}_g &= \hbar\Omega_R e^{-i\phi} \cos(\omega t + \phi) e^{-i\omega_0 t} \cdot c_e \\ i\hbar \dot{c}_e &= \hbar\Omega_R^* e^{i\phi} \cos(\omega t + \phi) e^{i\omega_0 t} \cdot c_g. \end{aligned} \quad (2.15)$$

Again the reference frame is changed, as the best insight into the dynamics of the coupled system is provided by the dressed-state picture. The name indicates that the “bare” states $|g\rangle$ and $|e\rangle$ are transformed into states “dressed” with the light field. Therefore the system is transferred by a unitary transformation to a frame rotating with the laser frequency ω , whereat $\delta = \omega - \omega_0$ denotes the detuning of the laser light in respect to the inner atomic transition frequency ω_0 :

$$\begin{aligned} c'_g(t) &= c_g(t) \\ c'_e(t) &= c_e(t) e^{i\delta t}, \end{aligned} \quad (2.16)$$

so that the differential equations 2.15 become:

$$i\hbar \frac{\partial}{\partial t} \begin{pmatrix} c'_g \\ c'_e \end{pmatrix} = \begin{pmatrix} 0 & \frac{\hbar\Omega}{2} \\ \frac{\hbar\Omega^*}{2} & -\hbar\delta \end{pmatrix} \begin{pmatrix} c'_g \\ c'_e \end{pmatrix}. \quad (2.17)$$

For this equations the following eigenenergies can be found:

$$\begin{aligned} \mathcal{E}_{\pm}(x) &= -\frac{\hbar}{2}(\delta \pm \sqrt{\Omega_R^2(x) + \delta^2}) \\ &= -\frac{\hbar}{2}(\delta \pm \Omega_{\text{eff}}), \end{aligned} \quad (2.18)$$

with the corresponding eigenstates, the dressed states:

$$\begin{aligned} |+\rangle &= e^{-i\frac{\phi}{2}} \sin(\theta)|g\rangle + e^{i\frac{\phi}{2}} \cos(\theta)|e\rangle \\ |-\rangle &= e^{-i\frac{\phi}{2}} \cos(\theta)|g\rangle - e^{i\frac{\phi}{2}} \sin(\theta)|e\rangle \end{aligned} \quad (2.19)$$

whereat θ is defined by $\cos 2\theta = -\frac{\delta}{\Omega_{\text{eff}}}$ and $\sin 2\theta = \frac{|\Omega_R|}{\Omega_{\text{eff}}}$.

Considering the dependence of the dressed states onto the laser detuning δ , illustrated in fig. 2.3, it appears that for resonant laser light, i.e., $\delta = 0$, the dressed states become an equal superposition of the “bare” states $|g\rangle$ and $|e\rangle$. If an atom enters adiabatically a far detuned light field with $|\delta| \gg |\Omega_R|$ its ground state $|g\rangle$ will be transferred into one single dressed state. For a red detuning, i.e., $\delta < 0$, as chosen in the experimental realization this will be the $|+\rangle$ -state and thus only the corresponding eigenenergy \mathcal{E}_+ has to be accounted for:

$$\begin{aligned} \mathcal{E}_+(x) &= -\frac{\hbar\delta}{2} + \frac{\hbar\delta}{2} \sqrt{1 + \frac{\Omega_R^2}{\delta^2}} \\ &\approx -\frac{\hbar\delta}{2} + \frac{\hbar\delta}{2} \left(1 + \frac{\Omega_R^2}{2\delta^2}\right) \\ &= \frac{\hbar\Omega_R^2}{4\delta} = V(x). \end{aligned} \quad (2.20)$$

It is common to quantify such a light shift potential in units of the recoil energy \mathcal{E}_r

$$\mathcal{E}_r = \frac{\hbar^2 k^2}{2m}, \quad (2.21)$$

being the energy a particle with mass m gains absorbing a photon of the standing light wave forming the potential.

Thus the double well potential realized by the superposition of two standing light beams as explained in the previous chapter can be formulated as dipole potential:

$$V(x) = V_1 \cos^2(kx) + V_2 \cos^2\left(\frac{k}{2}x\right) \quad (2.22)$$

with $V_{1,2}$ being the corresponding potentials according to eq. 2.20 for the two standing waves with amplitudes E_1 and E_2 . As for red detuned light the atoms are

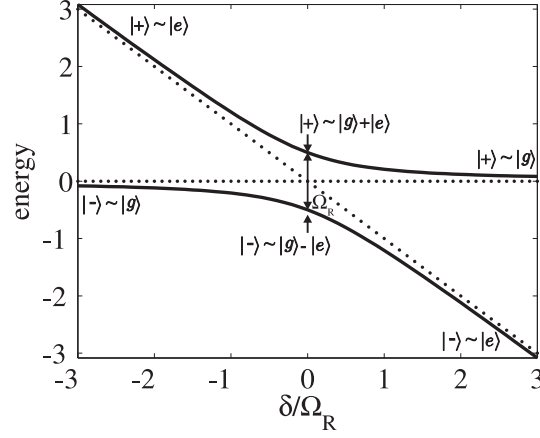


Figure 2.3: Dressed states for $\Omega_R = 1$ and $\hbar = 1$ to illustrate their dependence on the laser detuning. The dotted lines indicate the asymptotic behavior for $|\delta| \gg 1$.

attracted to the maxima of the intensity the sines of eq. 2.7 were replaced by cosine here and the potential reversed resulting in the double well shape as plotted in fig. 2.4.

Therewith the total Hamiltonian describing the experimental situation of an atom propagating in a continuous double well light shift potential is:

$$H_0(x) = -\frac{\mathbf{p}^2}{2m} + V_1 \cos^2(kx) + V_2 \cos^2\left(\frac{k}{2}x\right). \quad (2.23)$$

Spontaneous emission, i.e., the coupling of the atom with the vacuum modes, is neglected here, because it does not play a role for far detuned light fields as realized in the experiments.

The characteristic parameters used in [20] now depend on the amplitudes of the two standing light waves as follows:

$$\begin{aligned} x_{\min} &= \frac{1}{k} \arccos\left(-\frac{V_2}{4V_1}\right) \\ \omega_0 &= \sqrt{\frac{k^2}{m} \left(2V_1 - \frac{V_2^2}{8V_1}\right)} \\ E_B &= V_1 - \frac{V_2}{2} + \frac{V_2^2}{16V_1} \\ \tilde{E}_B &= V_1 + \frac{V_2}{2} + \frac{V_2^2}{16V_1}. \end{aligned} \quad (2.24)$$

As depicted in fig. 2.4 x_{\min} denotes the very first potential minimum of the continuous double well potential, ω_0 the angular frequency of harmonic oscillations on the bottom of each well, E_B is the height of the barrier in the middle of a double

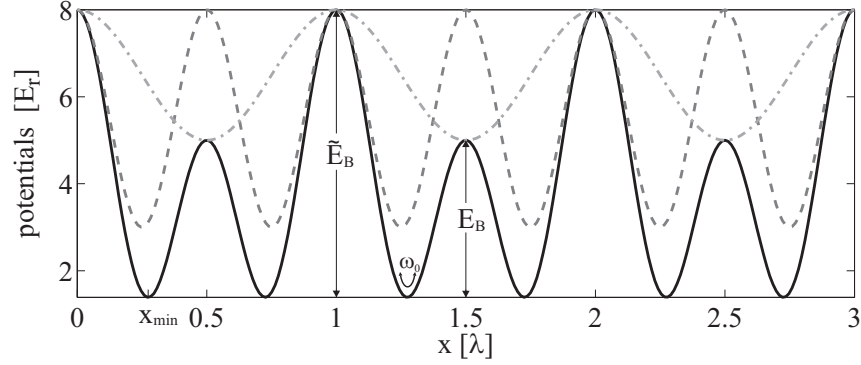


Figure 2.4: Continuous double well potential resulting from the combination of two far red detuned standing light waves plotted in units of the recoil energy \mathcal{E}_r . E_B denotes the barrier height of the barrier in the middle of each double well, \tilde{E}_B is the height of the barrier separating two double wells and ω_0 corresponds to the harmonic oscillation at the bottom of each well.

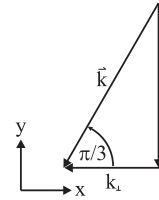
well and \tilde{E}_B correspondingly refers to the barrier height separating two neighboring double wells.

In contrast to the quartic potential in this realization the atoms will not only tunnel between the two wells of one double well unit cell, i.e., through barrier E_B , but also between different double wells, because of the finite height of \tilde{E}_B . However for appropriately chosen amplitudes $V_{1,2}$ the latter tunneling time is larger than the duration of the experiment, so that it can be neglected. The experimental parameters are always set the way that only on very long time scales not even in the scope of the experimentally measurable time a localized wave packet will spread out over many wells.

Asymmetry

As mentioned before particular attention has to be paid to the symmetry of the double wells. For $\lambda_2 = 2\lambda_1$ the resulting potential is a row of perfectly symmetric double wells, but already a slight deviation causes an asymmetry depending on the distance from the mirror, leading to significant changes of the tunneling dynamics. Among others this sensitivity of the tunneling dynamics onto the symmetry is adopted to verify the realization of a perfectly symmetric double well potential in the experiment as this is a crucial precondition to observe CDT.

In the experiment the wavelength λ_2 is achieved by impinging light with the wavelength λ_1 onto the mirror under an angle $\alpha = \pi/3$. The wavelength of the standing wave that is formed by this in x -direction is exactly twice as large as λ_1 . Hence an asymmetry of the double well results from a deviation of this angle α from $\pi/3$.



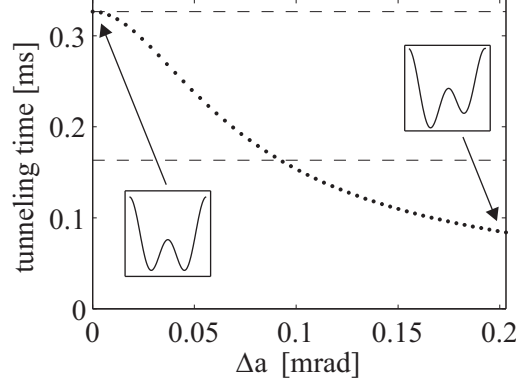


Figure 2.5: The tunneling time is plotted versus the deviation from the $\pi/3$ yielding perfectly symmetric double wells. The upper dashed vertical line corresponds to the tunneling time for the symmetric potential, while the lower line indicates half of this value. Already a deviation of $87\mu\text{rad}$ results in half the tunneling period.

For a typical distance of the atoms from the mirror the resulting tunneling time is plotted as a function of $\Delta\alpha = \alpha - \pi/3$ in fig. 2.5. Already a deviation of $87\mu\text{rad}$ results in a tunneling dynamics twice as fast as in the corresponding symmetric double well, showing the sensitivity, that makes the tunneling time perfectly suited to check the symmetry of the realized potential.

2.2 Time evolution of an atom in an unperturbed double well potential

To learn about the dynamics of the atom in the double well light-shift potential as eq. 2.22 the time-dependent Schrödinger equation for the Hamiltonian $H = H_0(x)$ (eq. 2.23) has to be solved:

$$i\hbar \frac{\partial}{\partial t} |\Psi(x, t)\rangle = H(x, t) |\Psi(x, t)\rangle. \quad (2.25)$$

Due to the spatial periodicity of the potential this can be done by adopting Bloch's theorem [27]. Hence the ansatz for the wavefunction, a Bloch wave, consists of the product of plane waves, that have accumulated multiples of the lattice momentum $\hbar k$ and their corresponding probability amplitude a_n :

$$\Psi(x, t) = \sum_{n=-\infty}^{\infty} a_n e^{inkx}. \quad (2.26)$$

Fitting this to the Schrödinger equation, utilizing the Euler expansion $\cos^2(kx) = \frac{1}{2} + \frac{1}{4}(e^{i2kx} + e^{-i2kx})$ and shifting indices, yields:

$$i\hbar \sum_{n=-\infty}^{\infty} \dot{a}_n e^{inkx} = \sum_{n=-\infty}^{\infty} e^{inkx} \left[\frac{\hbar^2 n^2 k^2}{2m} a_n + \frac{V_1}{2} a_n + \frac{V_1}{4} (a_{n-2} + a_{n+2}) + \frac{V_2}{2} a_n + \frac{V_2}{4} (a_{n-1} + a_{n+1}) \right]. \quad (2.27)$$

As this has to be valid for all n , a differential equation for each probability amplitude a_n is given by:

$$i\hbar \dot{a}_n = \left(\frac{\hbar^2 n^2 k^2}{2m} + \frac{V_1}{2} + \frac{V_2}{2} \right) a_n + \frac{V_1}{4} (a_{n-2} + a_{n+2}) + \frac{V_2}{4} (a_{n-1} + a_{n+1}). \quad (2.28)$$

For this methods only multiples of the wave vector k can be devolved, which is correct for a row of perfectly symmetric double wells. A slight asymmetry, as could be the case in the experiment, if λ_2 is not exactly two times λ_1 , has to be accounted for approximately as an added phase. The Potential in this approximation looks like: $V = V_1 \cos^2(kx) + V_2 \cos^2(\frac{k}{2}x + \phi)$, yielding an equation for the probability amplitude a_n :

$$i\hbar \dot{a}_n = \left(\frac{\hbar^2 n^2 k^2}{2m} + \frac{V_1}{2} + \frac{V_2}{2} \right) a_n + \frac{V_1}{4} (a_{n-2} + a_{n+2}) + \frac{V_2}{4} (a_{n-1} e^{2i\phi} + a_{n+1} e^{-2i\phi}), \quad (2.29)$$

or as vector equation

$$i\hbar \begin{pmatrix} \dot{a}_{-N} \\ \vdots \\ \dot{a}_{-1} \\ \dot{a}_0 \\ \dot{a}_1 \\ \vdots \\ \dot{a}_N \end{pmatrix} = M \cdot \begin{pmatrix} a_{-N} \\ \vdots \\ a_{-1} \\ a_0 \\ a_1 \\ \vdots \\ a_N \end{pmatrix}, \quad (2.30)$$

with

$$M = \begin{pmatrix} \frac{\hbar^2 (-N)^2 k^2}{2m} + \frac{V_1}{2} + \frac{V_2}{2} & \frac{V_2}{4} e^{-2i\phi} & \frac{V_1}{4} & 0 & \cdots & \cdots & 0 \\ \frac{V_2}{4} e^{+2i\phi} & \ddots & \ddots & \ddots & & & \vdots \\ \frac{V_1}{4} & \ddots & \ddots & \ddots & \ddots & & \vdots \\ 0 & \ddots & \ddots & \frac{V_1}{2} + \frac{V_2}{2} & \ddots & \ddots & 0 \\ \vdots & & & & \ddots & \ddots & \frac{V_1}{4} \\ \vdots & & & & \ddots & \ddots & \frac{V_2}{4} e^{-2i\phi} \\ 0 & \cdots & \cdots & 0 & \frac{V_1}{4} & \frac{V_2}{4} e^{+2i\phi} & \frac{\hbar^2 N^2 k^2}{2m} + \frac{V_1}{2} + \frac{V_2}{2} \end{pmatrix}, \quad (2.31)$$

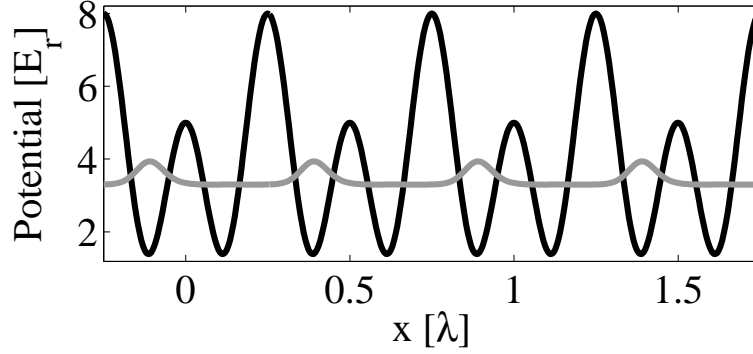


Figure 2.6: The initial state $|\Psi_0\rangle$ for a continuous double well potential is a superposition of the two lowest eigenstates of the potential $|\varphi_1\rangle$ and $|\varphi_2\rangle$, which can be found by diagonalizing the matrix M in 2.31.

which can be calculated utilizing a standard Runge-Kutta method (ode45) provided by the software package MATLAB. This method is referred to as diffraction method in the following and for all calculations presented N was restricted to a finite number of 21.

2.2.1 Initial state

For a continuous double well potential the initial condition to observe the tunneling dynamics is that the atoms at time $t = t_0$ are localized in every second well only, i.e., in the left (or right) well of each double well in the row. For a single double well this localized state could be described as sum or difference of the lowest eigenstate doublet. This is also true for a continuous double well potential. Its eigenstates Ψ_n follow from eq. 2.26 with the probability amplitudes given by the eigenvectors of the matrix M (eq. 2.31). Therewith the initial state of a wave packet localized in every second well of a continuous double well potential constant in time reads $|\Psi_0\rangle = |+\rangle = \frac{1}{\sqrt{2}}(|\varphi_1\rangle + |\varphi_2\rangle)$ or $|\Psi_0\rangle = |-\rangle = \frac{1}{\sqrt{2}}(|\varphi_1\rangle - |\varphi_2\rangle)$ and yields oscillations between the two minima of each double well with a periodicity of the tunneling splitting Δ as anticipated. Such an initial state is plotted in fig. 2.6

Of course feeding in a perfectly localized initial state does not comply with the experimental reality. To reproduce the experimental preparation process the incoming atoms are represented by a plane wave $\Psi(t = 0) = a_0 = 1$. They are loaded into the symmetric ground state of the potential by slowly switching on the light shift potential, so that the atoms follow adiabatically. Then atoms are removed from every second well by absorbing them, which is described theoretically by an imaginary potential [28]. Practically such a complex potential emerges from the interaction of near resonant light with an open two-level system [29, 30, 31], or in other words, atoms are pumped from a metastable state via open transition to the

absolute ground state using suitable light. Which means, that the ground state $|g\rangle$ in the considerations before is a metastable state of the atom, whose lifetime is longer than the duration of the experiment and the absolute ground state of the atom is not detected and therefore those atoms in the absolute ground state are “deleted” from the setup. Accounting for this new standing light wave with amplitude V_{abs} the complete light shift potential has to be written as:

$$V(x, t) = V_1(t) \cos^2(kx) + V_2(t) \cos^2\left(\frac{k}{2}x\right) + i\hbar \cdot V_{\text{abs}}(t) \cos^2\left(\frac{k}{2}x + \phi_{\text{abs}}\right), \quad (2.32)$$

at which the absorptive potential is shifted by ϕ_{abs} against the double well potential, so that its minima coincide with one well of each double well and the maxima are close to the other well as indicated in fig. 2.7. Thus atoms are predominantly removed from every second well only. The constant phase shift is only an approximation of the experimental situation, a topic addressed in context of the experimental realization (sec. 3.3).

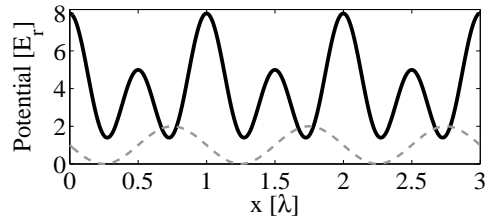


Figure 2.7: Double well potential (black) and shifted imaginary potential (gray, dashed).

The time dependence of the potentials $V_{1,2}$, i.e., the adiabatic increase, is experimentally realized using a specially designed optical gray filter. To be able to include it to the numerics as accurate as possible it is measured employing a ccd-camera image (cf. fig. 3.6) and then the profiles are fitted with an error function. The time dependence and position of the imaginary potential V_{abs} is also determined by a gauss fit of the ccd-camera image. The amplitude of the imaginary potential is adjusted such that the decrease of the absolute number of atoms after the absorption process matches the experimentally adjusted one of typically 70%.

Therewith the probability amplitudes (eq. 2.29) for the Bloch-wave ansatz now read:

$$\begin{aligned} i\hbar\dot{a}_n = & \left(\frac{\hbar^2 n^2 k^2}{2m} + \frac{V_1(t)}{2} + \frac{V_2(t)}{2} + i\frac{V_{\text{abs}}(t)}{2} \right) a_n + \frac{V_1(t)}{4} (a_{n-2} + a_{n+2}) \\ & + \left(\frac{V_2(t)}{4} e^{2i\phi} + i\frac{V_{\text{abs}}(t)}{2} e^{2i\phi_{\text{abs}}} \right) a_{n-1} + \left(\frac{V_2(t)}{4} e^{-2i\phi} + i\frac{V_{\text{abs}}(t)}{2} e^{-2i\phi_{\text{abs}}} \right) a_{n+1}. \end{aligned} \quad (2.33)$$

In the following discussions the preparation process, i.e., the imaginary part of the potential $i\hbar \cdot V_{\text{abs}}(t) \cos^2(\frac{k}{2}x + \phi_{\text{abs}})$ is left out for clarity, where it is not relevant. It can always be added to reproduce the experimental occurrences ab initio.

2.2.2 Near field measurements

The combination of two periodic structures under an angle or with slightly different periods creates so called Moiré patterns [32]. In this interference patterns new struc-

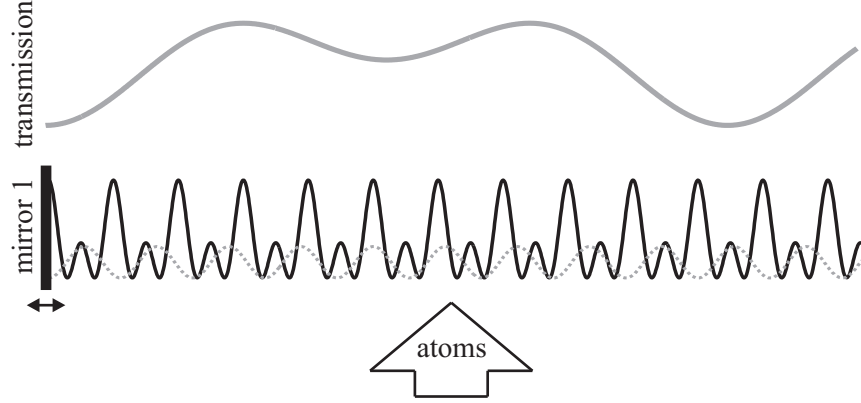


Figure 2.8: A sketch of the setup measuring the near field distribution of the atoms. Due to the varying phase shift between the double well potential (black) and the absorptive potential (gray, dashed) moving the mirror, i.e., scanning the atoms along the potentials is like moving a grating over the atom distribution in one double well yielding an image of distribution of the atoms in the potential.

tures appear with periodicities proportional to the angle or the sum and difference of the two periods respectively.

In the experiment the combination of the periodic double well structure with $\cos^2(k_1 x) + \cos^2(\frac{k_1}{2} x)$ and the imaginary potential with a spatial frequency of $\cos^2(\frac{k_2}{2} x)$ yields due to their different periodicities the following Moir'e pattern:

$$I_{\text{interfered}} = I_{\text{dw}} + I_{\text{abs}} \propto \cos\left(\frac{k_1 + k_2}{2} x\right) \cdot \cos\left(\frac{k_1 - k_2}{2} x\right) + \frac{1}{2} \cos(2k_1 x) \quad (2.34)$$

where new spatial frequencies appear. A slow oscillation with $k_1 - k_2$ forms an envelope of a faster one with $k_1 + k_2$ and is combined with an oscillation with two times k_1 .

This intensity profile can be tested utilizing the atoms by varying their distance from the mirror and measuring their total transmission as depicted in fig. 2.8 (see also sec. 3.3.3). As the imaginary potential removes atoms it is comparable to a grid letting the atoms pass only at the position of its minima and the double well structure localizes the atoms at its potential minima. The profile resulting from the combination of those two structures resembles a double well only upside down and with a period of $k_1 - k_2$. Furthermore it reveals the position at which the atoms are perfectly prepared, i.e., a minimum of the imaginary potential coincides exactly with one well of the double well structure and the atoms are completely removed from the other. This is given for the position of the maxima of this upside down double well structure.

For a row of perfectly equivalent double wells the near field measurement results in a transmission shaped symmetrically, i.e., with two maxima of same height, as

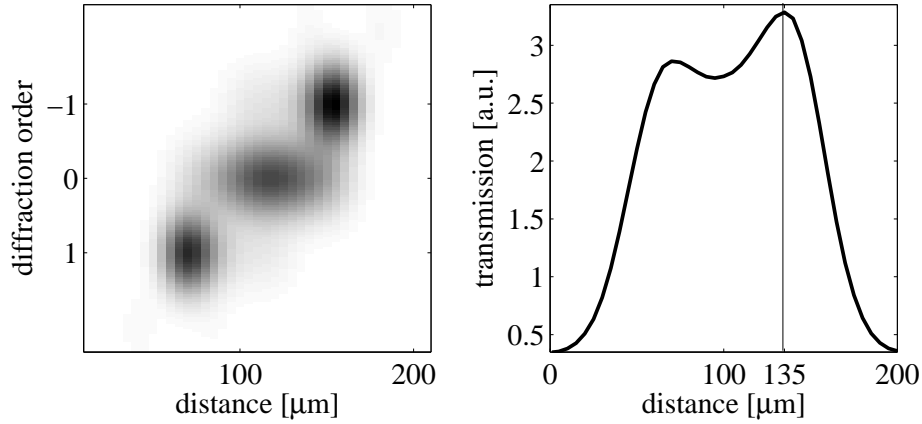


Figure 2.9: Testing the Moiré pattern of the double well structure combined with the absorptive potential. The diffraction efficiencies (left) and total transmission (right) is simulated as a function of the phase ϕ_{abs} , corresponding to the distance from the mirror in the experimental realization for a double well potential combined with an imaginary potential. The vertical line in the right picture indicates the x -position corresponding to the phase shift ϕ_{abs} that yield a preparation of a localized state.

sketched in the upper part of fig. 2.8. Due to a constant phase shift between the two standing waves forming the double wells and for $\alpha = \pi/3$, all wells will have the same asymmetry and so will the transmission spectrum. For an angle α , that is not exactly $\pi/3$ the double wells scanned in the experiment are all different, so that the resulting shape of the transmission is a mixture of all kinds of double wells and can not be utilized as indicator for the symmetry of the potential at a particular position x . But it still gives a good impression of the localization of the initial wave-packet. In the simulations this is accounted for by changing the shape of the double well, i.e., the phase ϕ in eq. 2.33, while ϕ_{abs} is scanned. The expected shape of the transmission as a function of the distance from the mirror is depicted on the right hand side of fig. 2.9. It still reveals two maxima but they will never be of the same height. Still at the mirror position for which the transmission is maximal the phase shift between double well potential and imaginary potential is just such that the minima of the latter coincide with the first and second well respectively, resulting in a localized wave packet either in the right or left well, which can be used as initial state for the experiment. For this calculation the beat period of double well and imaginary potential was assumed $210\mu\text{m}$ suggesting that an atom passing the mirror at a distance of $135\mu\text{m}$ will be localized in the right well after the preparation, i.e., absorption process. The left hand side of fig. 2.9 shows the corresponding diffraction efficiencies in the different orders underlying the transmission spectrum. The weight of the zeroth order depends on the absorption rate, i.e., the amplitude of the imaginary potential V_{abs} .

2.2.3 Bragg Diffraction

Bragg diffraction [33] is a well understood effect that is employed for adjusting the incidence angle of the atoms onto the standing light waves. It is crucial for the measurements to guarantee a perpendicular incidence of the atomic beam onto the potential. The sensitivity of the effect of Bragg diffraction to this angle and its simple feasibility makes it a perfect tool for this adjustment. For matter waves interacting with light shift potentials Bragg diffraction was realized for the first time in 1988 by David Pritchard [34]. It appears for weak potentials in the so called Bragg regime, which is given if the potential maximum is smaller than its recoil energy \mathcal{E}_r . In this case significant scattering only occurs if the incident wave impinges under the Bragg angle $\pm\theta_B$ with

$$\sin(\theta_B) = \frac{n\lambda_{dB}}{\lambda_L}, \quad (2.35)$$

and only exactly one diffraction order is observed. This regime can be described by the dynamical diffraction theory, which was derived for the first time for x-rays by Ewald [35]. As carried out in [29] the diffracted intensity can be calculated as:

$$I(b_s, V_s, \theta_s) = \frac{\sin^2(2\pi V_s b_s \sqrt{\xi^2 + 1})}{\xi^2 + 1} \quad \text{with} \quad \xi = \frac{1}{2} \frac{\theta_s}{V_s} \quad (2.36)$$

for the scaled magnitudes

$$\begin{aligned} b_s &= \frac{b}{L_{\text{Talbot}}} \\ V_s &= \frac{V}{\mathcal{E}_r} \\ \theta_s &= \frac{\theta_B - \theta}{\theta_B}, \end{aligned} \quad (2.37)$$

with b being the width of the light-shift potential and $L_{\text{Talbot}} = \frac{\lambda^2}{2\lambda_{dB}}$ the Talbot length [36]. The sensitive dependence onto the angle of incidence and the symmetric appearance for $\pm\theta_B$ allows to determine the perpendicular incidence of the atoms onto the standing wave.

2.3 Introducing time-dependent driving-field

The simplest way of driving a double well potential is adding a linear potential rocking around the symmetry point of the double well with some time-dependence $f(t)$ as assumed by Grossmann et al. [20] and plotted in fig. 2.10(a). For a continuous double well potential this reads:

$$H_{\text{th}}(x, t) = \underbrace{\frac{\mathbf{p}^2}{2m} + V_1 \cos^2(kx) + V_2 \cos^2(\frac{k}{2}x)}_{H_0(x)} + \underbrace{S\tilde{x} \cdot f(t)}_{H_{\text{d,th}}(x, t)} \quad (2.38)$$

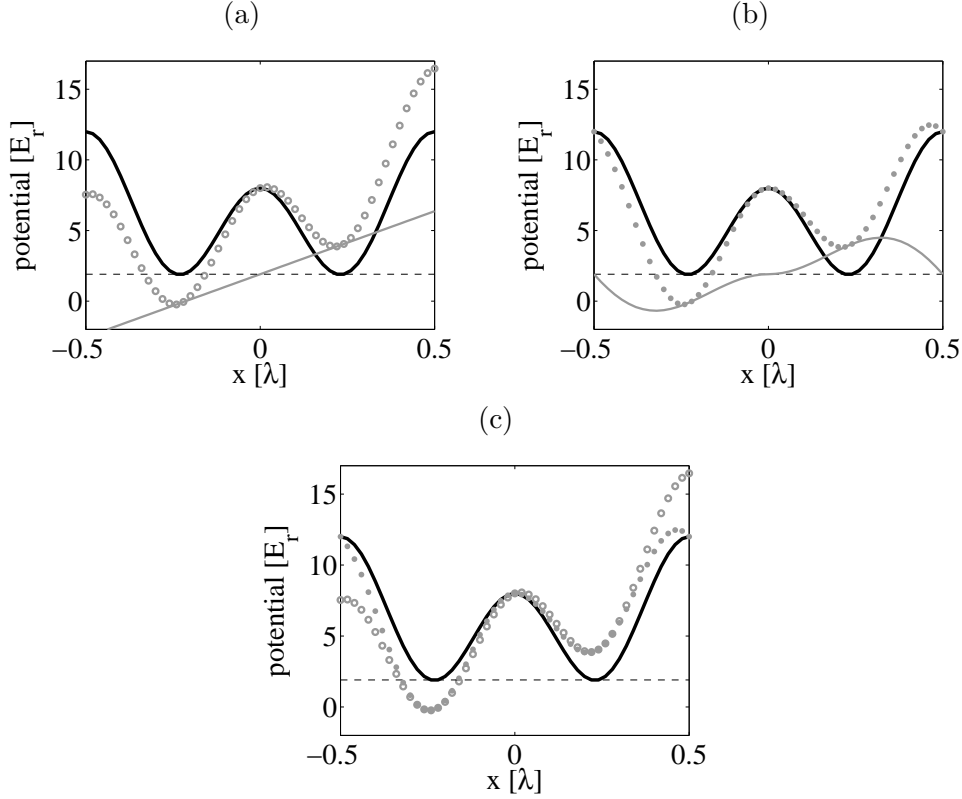


Figure 2.10: (a) Illustration of a double well potential driven with a linear rocker. (b) A double well with a sinusoidally shaped driving. (c) Comparing the potentials resulting from a linear rocking driving field (open circles) and one, where the driving is sinusoidally shape (dots).

where \tilde{x} denotes the distance to the symmetry point of each double well. This might be simple from a theoretical point of view. In the experiment however it is straightforward to realize the driving by changing the angle α which yields a phase shift between the two light shift potentials creating the double wells. Instead of a linear potential this is approximately equivalent to adding a sinus rocking around the symmetry point. The time-dependent Hamiltonian describing the experimentally realized system reads as follows:

$$H(x, t) = \frac{\mathbf{p}^2}{2m} + V_1 \cos^2(kx) + V_2 \cos^2(kx \cdot \cos\{\alpha + \epsilon f(t)\}), \quad (2.39)$$

where ϵ is the deviation from the incidence angle $\alpha = \pi/3$ corresponding to the amplitude of the driving and $f(t)$ is its time dependence with the characteristic driving frequency $\omega_d = 2\pi/T_d$. Even for strong driving ϵ will be small compared to α , so that close to the mirror surface (for small x) the approximation $(\sin(\epsilon x) \approx \epsilon x)$

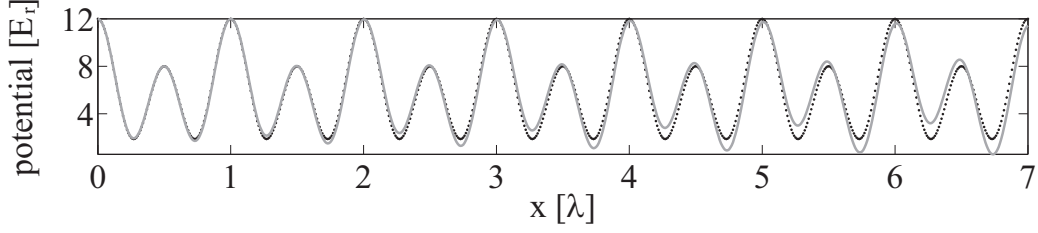


Figure 2.11: The picture depicts the dependence of the driving amplitude onto the distance from the mirror, the unperturbed potential is added as reference (black dots).

yields a Hamiltonian of the same form as eq. 2.38:

$$H(x, t) = \underbrace{\frac{\mathbf{p}^2}{2m} + V_1 \cos^2(kx) + V_2 \cos^2\left(\frac{k}{2}x\right)}_{H_0(x)} + \underbrace{Sx \sin(k\tilde{x}) \cdot f(t)}_{H_d(x, t)}, \quad (2.40)$$

with S being the amplitude of the driving that now reads:

$$S = \sin(\alpha) \cdot V_2 k \epsilon. \quad (2.41)$$

In fig. 2.10(b) this sine shaped rocking around the symmetry point is depicted and in (c) it is compared to the theoretically assumed linear rocker. An important point is that the x -dependence (not \tilde{x}) of the sine shaped rocking yields different driving amplitudes depending on the distance of a double well from the mirror and of course a very slight asymmetry of the driving of each double well as well as a small movement of the barrier in the middle of each double well as illustrated in fig. 2.11. Still simulations show (cf. sec. 2.3.4) that all these deviations from the ideal liner rocker do only marginally change the effects of the driving. In particular the effect of CDT can be realized employing this form of driving as the generalized symmetry of the system is conserved. The symmetry dependence of CDT comes from the fact, that it appears due to an exact crossing of those eigenenergies dominating the tunneling dynamics, which may only happen, if the system obeys the generalized parity symmetry and the two states belong to different parity classes. Otherwise only avoided crossing appear.

2.3.1 Floquet approach

In the majority of the cases solving the Schrödinger equation for time-dependent Hamiltonians is not possible analytically. Separation of variables as is done conventionally for time independent hamiltonian operators can not be applied as the hamiltonian operator of a time-dependent quantum system is not invariant up to an arbitrary time translation and therefore the energy of the system is not conserved.

The periodicity of the time dependence introduced by the driving however enables a solution of the dynamics. Analogues to the Bloch-theorem [27] helping to find solutions for spatially periodic quantum systems the solutions for time periodic quantum systems can be found by means of the Floquet-theorem [37]. The nice thing about this method is that it does not constrain the parameters of the driving in contrast to the often used perturbation theory.

As the Hamiltonian operator (eq. 2.40) is periodic in time, $H(t + T_d) = H(t)$, it is invariant up to the translation $t \rightarrow t + T_d$, where T_d is the period of the driving. According to the theorem for such time periodic Hamiltonians there exist Floquet-state solutions $|\Psi_\alpha(x, t)\rangle$ to the Schrödinger equation (eq. 2.25) that have the form

$$|\Psi_\alpha(x, t)\rangle = e^{-i\epsilon_\alpha t/\hbar} |\Phi_\alpha(x, t)\rangle, \quad (2.42)$$

where $|\Phi_\alpha(x, t)\rangle$, a so-called Floquet mode, is again periodic in time ($|\Phi_\alpha(x, t)\rangle = |\Phi_\alpha(x, t + T_d)\rangle$). Due to the periodicity the time evolution of the system can be separated into a long-term behavior and a short-time evolution.

Introducing the Hermitian operator $\mathcal{H}(x, t) \equiv H(x, t) - i\hbar \frac{\partial}{\partial t}$ the problem is reduced to solving the eigenvalue equation for the quasi energies ϵ_α and eigenstates $|\Phi_\alpha\rangle$

$$\mathcal{H}|\Phi_\alpha(x, t)\rangle = \epsilon_\alpha |\Phi_\alpha(x, t)\rangle \quad (2.43)$$

in the composite Hilbert space $\mathcal{R} \otimes \mathcal{T}$ consisting of the Hilbert space of time integrable functions and the space of functions periodic in t with period T_d . This displays the great benefit of this method: it reduces the problem to solving the time-independent Schrödinger equation.

Another nice thing about this method is that it respects the periodicity at all levels of approximation and avoids the occurrence of so-called secular terms, i.e., linear or not periodic in the time variable, unlike conventional time-dependent perturbation theory.

It has to be noted that the Floquet modes Φ_α and $\Phi_{\alpha'} = \Phi_\alpha e^{in\omega_d t}$ with n being an integer yield identical physical solutions, so that the quasi energies ϵ_α are defined except for multiples of $\hbar\omega_d$, where $\omega_d = \frac{2\pi}{T_d}$ is the driving frequency. This reveals that those quasi energies do not denote absolute energies and allows to project them to a zone $(-\frac{\hbar\omega_d}{2} \leq \epsilon \leq \frac{\hbar\omega_d}{2})$ comparable with the first Brillouin-zone known for spatially periodic systems. This is also where the name comes from: The “quasi” reflects the formal analogy with the quasi momentum $\hbar k$ in a Bloch wave function. Following from the Bloch wave description this Bloch wave vector k is unique only up to multiples of the reciprocal lattice vector G , so that the problem can be reduced to the first Brillouin zone, i.e., a primitive cell of the reciprocal lattice. In contrast to the quasi momentum that is a continuous variable, the quasi energies in the Floquet theory are quantized.

To learn about the long-time dynamics of the system a time propagator $U(nT, t_0)$ can be introduced:

$$|\Psi(x, nT)\rangle = U(nT, t_0)|\Psi(x, t_0)\rangle, \quad U(t_0, t_0) = 1, \quad (2.44)$$

generating a discrete quantum map for any initial state $|\Psi(x, t_0)\rangle = \sum_{\alpha} c_{\alpha} |\Psi_{\alpha}(x, t_0)\rangle$. Setting $t_0 = 0$ the temporal autocorrelation function is defined by:

$$\begin{aligned}
 P_n &= |\langle \Psi_n | \Psi_0 \rangle|^2 \\
 &= |\langle \Psi(x, nT) | \Psi(x, t_0) \rangle|^2 \\
 &= \sum_{\alpha} c_{\alpha}^* e^{in\epsilon_{\alpha}T/\hbar} \langle \phi_{\alpha}(x, t_0) | \Psi_0 \rangle \cdot \sum_{\beta} c_{\beta} e^{-in\epsilon_{\beta}T/\hbar} \langle \Psi_0 | \phi_{\beta}(x, t_0) \rangle \\
 &= \sum_{\alpha=\beta} |\langle \phi_{\alpha}(x, t_0) | \Psi_0 \rangle|^4 + \sum_{\alpha \neq \beta} e^{in(\epsilon_{\alpha}-\epsilon_{\beta})T/\hbar} \cdot |\langle \phi_{\alpha}(x, t_0) | \Psi_0 \rangle|^2 \cdot |\langle \phi_{\beta}(x, t_0) | \Psi_0 \rangle|^2.
 \end{aligned} \tag{2.45}$$

Comparing this to the findings for the tunneling dynamics in a time constant double well potential it is obvious that the second term in the last row containing all quasi energy differences $\epsilon_{\alpha} - \epsilon_{\beta}$ is alike eq. 2.3, where the dynamics is ruled by the energy difference $\Delta = \mathcal{E}_2 - \mathcal{E}_1$. Thus due to driving many quasi energy differences mix up yielding a more complex dynamics of beats of more than one tunneling frequency. At least this may happen, but as these frequencies add up proportional to their overlap with the initial state $|\psi_0\rangle$, one finds, at least for the experimental situation described in this work, that the time evolution of the system is dominated by only one or two differences, i.e., frequencies for most driving parameters. The first term of eq. 2.45 represents a long-time average of the autocorrelation function P_n .

Due to the Floquet theorem the dynamics of a particle in a time periodically driven double well can be derived by solving eq. 2.43 numerically. Therefore the time periodic function Φ_{α} is expanded in Fourier coefficients choosing the eigenstates $\varphi_k(x)$ of the unperturbed double well potential as an orthogonal basis:

$$|\Phi_{\alpha}(x, t)\rangle = \sum_{n=-\infty}^{\infty} \sum_{k=1}^{\infty} c_{\alpha,k}^n(x) |\varphi_k(x)\rangle e^{in\omega_d t}, \quad c_{\alpha,k}^n(x) \in \mathbb{R}. \tag{2.46}$$

As the energy is no longer conserved for the time-dependent function $H(t)$ the averaged energy over one period of driving is considered instead. With the inner product for the composite Hilbert space

$$\langle\langle \Phi_{\alpha'} | \Phi_{\beta'} \rangle\rangle := \frac{1}{T} \int_0^T dt \int_{-\infty}^{\infty} dx \Phi_{\alpha'}^*(x, t) \Phi_{\beta'}(x, t) = \delta_{\alpha', \beta'} = \delta_{\alpha, \beta} \delta_{n, m} \tag{2.47}$$

and multiplying with $\langle \varphi_j | e^{im\omega_d t} \equiv \langle \varphi_j m |$ equation 2.43 becomes:

$$\begin{aligned}
 \sum_{n=-\infty}^{\infty} \sum_{k=1}^{\infty} \langle\langle \varphi_j m | \mathcal{H} | \varphi_k n \rangle\rangle c_{\alpha,k}^n(x) &= \epsilon_{\alpha} \sum_{n=-\infty}^{\infty} \sum_{k=1}^{\infty} \langle\langle \varphi_j m | \varphi_k n \rangle\rangle c_{\alpha,k}^n(x) \\
 \sum_{n=-\infty}^{\infty} \sum_{k=1}^{\infty} \langle\langle \varphi_j m | \left(H_0(x) + Sx \sin(k\tilde{x}) \cdot \sin(\omega_d t) - i\hbar \frac{\partial}{\partial t} \right) | \varphi_k n \rangle\rangle c_{\alpha,k}^n(x) &\dots \\
 &= \epsilon_{\alpha} c_{\alpha,j}^m(x)
 \end{aligned} \tag{2.48}$$

with $\sin(\omega_d t) = \frac{1}{2}(e^{i\omega_d t} - e^{-i\omega_d t})$ this yields:

$$\sum_{n=-\infty}^{\infty} \sum_{k=1}^{\infty} \left\{ (E_k + n\hbar\omega_d) \delta_{j,k} \delta_{m,n} + \frac{S}{2} \langle \varphi_j | \tilde{x} \sin(kx) | \varphi_k \rangle \cdot \dots \right. \\ \left. (\delta_{m,n+1} - \delta_{m,n-1}) \right\} c_{\alpha,k}^n(x) = \epsilon_{\alpha} c_{\alpha,j}^m(x). \quad (2.49)$$

Introducing the following basis

$$\begin{pmatrix} (\varphi_1, -N) \\ (\varphi_1, -N+1) \\ \vdots \\ (\varphi_1, +N) \\ (\varphi_2, -N) \\ \vdots \\ (\varphi_2, +N) \end{pmatrix} \quad (2.50)$$

and restricting to a finite number of eigenstates as well as fourier coefficients eq. 2.48 can be written as a vector equation:

$$M c_{\alpha} = \epsilon_{\alpha} c_{\alpha}, \quad (2.51)$$

with the Matrix M consisting of the diagonal elements

$$M_{ii} = \begin{pmatrix} E_i - N\hbar\omega_d & & & 0 \\ & E_i - (N-1)\hbar\omega_d & & \\ & & \ddots & \\ 0 & & & E_i + N\hbar\omega_d \end{pmatrix}, \quad (2.52)$$

and the off-diagonal elements

$$M_{ij} = \begin{pmatrix} 0 & -\frac{S}{2} \tilde{x}_{ij} & & 0 \\ \frac{S}{2} \tilde{x}_{ij} & 0 & -\frac{S}{2} \tilde{x}_{ij} & \\ & \ddots & \ddots & \\ 0 & & & 0 \end{pmatrix} \quad \text{for } (i < j), \quad (2.53)$$

and $M_{ij} = M_{ji}^*$ for $i > j$, whereat x_{ij} denotes the transition matrix element $x_{ij} = \langle \varphi_i | \tilde{x} \sin(kx) | \varphi_j \rangle$ at which all even-even or odd-odd transitions are zero. For all results shown in the following the 15 lowest energy eigenstates are taken into account. Solving this eigenvalue problems yields a bunch of quasi energies ϵ_{α} as shown in fig. 2.12 (left) as a function of the driving frequency and for a set of parameters typical for the experimental realization.

Of course not all those eigenstates are relevant for the dynamics of an atom in the potential. As for describing the initial state of localized particle in the double well only the two lowest of all eigenstates where needed, only those quasi energies

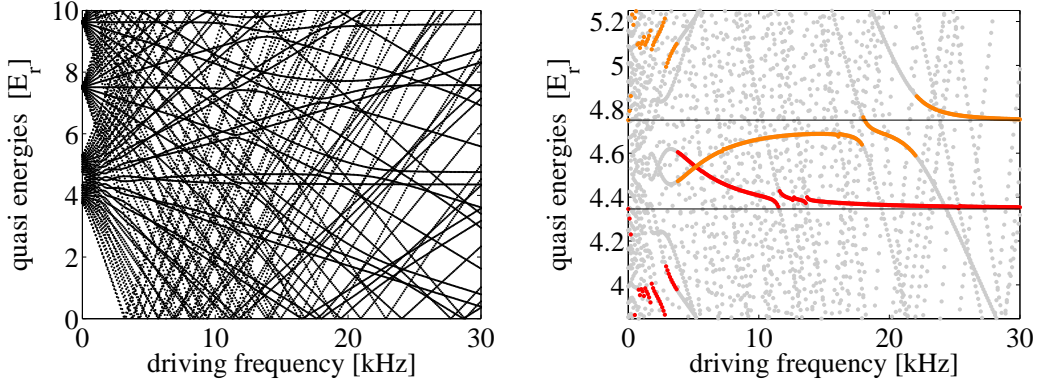


Figure 2.12: (left) With help of the Floquet theorem solutions to the driven double well can be found in form of quasi energies, here plotted as a function of driving frequency. (right) The dynamics of the system is reflected by those quasi energies having the biggest overlap with the ground state. The parameters are $V_1 = 6.25\mathcal{E}_r$, $V_2 = 5.40\mathcal{E}_r$ and $S = 7353\mathcal{E}_r$, which corresponds to a lift of $0.93\mathcal{E}_r$ of the wells out of equilibrium.

having an overlap with this ground state doublet do contribute. This overlap is calculated by projecting $|\Psi_0\rangle = \frac{1}{\sqrt{2}}(|\varphi_1\rangle + |\varphi_2\rangle)$ (cf. sec. 2.2.1) onto the Floquet states:

$$|\langle\Psi_0|\Phi_\alpha(x,t)\rangle|^2 = \frac{1}{2}(|c_{\alpha,1}^0|^2 + |c_{\alpha,2}^0|^2 + c_{\alpha,1}^0 c_{\alpha,2}^{0*} + c_{\alpha,2}^0 c_{\alpha,1}^{0*}). \quad (2.54)$$

In fig. 2.12 (right) the local Floquet spectrum is shown, zoomed into the picture depicted on the left. Furthermore those quasi energies having the biggest overlap with the ground state doublet $(\varphi_1, 0)$ and $(\varphi_2, 0)$ are highlighted, i.e., those dominating the dynamics of the system. However this is a simplification as the spectrum can not always be reduced to only two energy levels. In the parameter range where there are more than two eigenstates with relevant overlap with the initial state complicated beats of various tunneling frequencies may appear. Generally it can be noted that for very high and very low driving frequencies, where this frequency is not of the order of the system's inherent timescales and therefor the processes uncouple, the spectrum will resemble that of the unperturbed system, i.e., will be dominated by only two states. If this is the case it is appropriate to use the two-state approximation, which will be introduced in sec. 2.3.3, instead of the full Floquet analysis to describe the systems dynamic.

As a reference the eigenenergies of the undriven double well potential are indicated by the horizontal lines in the left picture of fig. 2.12. If two eigenenergies dominating the dynamics approach each other, this implies a slowing of the tunneling. If they literally cross, as can be observed in this picture for a driving frequency of $\omega_d = 5\text{kHz}$, this yield an absence of any dynamics. This means switching on an external field with appropriate parameters enables to totally suppress the tunnel-

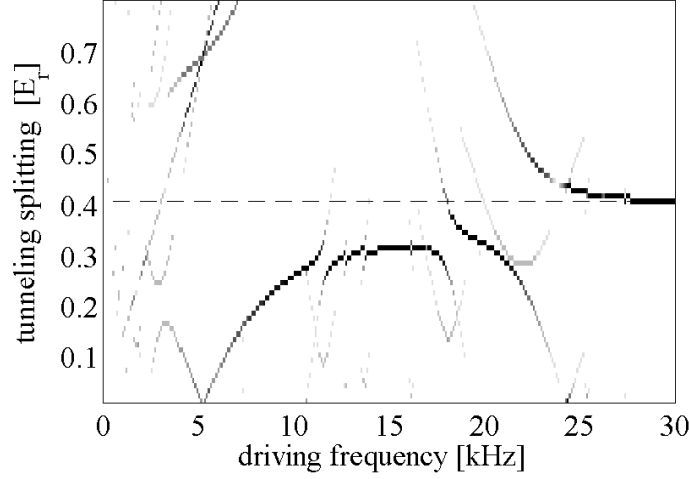


Figure 2.13: Tunneling splitting as function of the driving frequency for typical experimental parameters calculated using the Floquet matrix method. Plotted are all quasi energy differences, whereat the gray shading corresponds to the overlap of the corresponding Floquet states with the initial state, i.e., the ground state doublet.

ing of a particle and therewith to localize it without changing the properties of the double well. This is what is called CDT.

As is pointed out in [38] such crossings of the two relevant quasi energies depend on special combinations of the parameters S and ω_d forming a one-dimensional manifold in the (S, ω_d) parameter-space of an approximately linear shape. Hence finding suitable parameter values on this manifold is the precondition to dynamically localize atoms, i.e., to realize CDT.

To compare the theoretical predictions to the experimental findings the tunneling splitting is calculated, i.e., the energy gaps between the different quasi energies, shown in fig. 2.13, at which the gray shading represents the overlap of the particular eigenstates with the ground state doublet. The dashed line indicates the tunneling rate for the unperturbed double well. Everything above implies a faster dynamics, everything below is slower. One can see, that in the range between 10 – 20 kHz only one tunneling frequency dominates the tunneling, which is only a bit below the unperturbed rate. For decreasing driving frequency approaching $\omega_d = 5\text{kHz}$ the dynamics slows continuously till the splitting reaches a complete zero, indicating CDT. For the frequency range between 20 and 25kHz a resonance appears, namely the fundamental resonance $\Omega = \mathcal{E}_3 - \mathcal{E}_2$, implying that it should also be possible to observe a significant increase of the tunneling rate due to coupling to the next excited eigenstate.

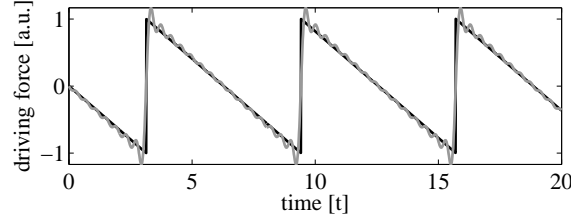


Figure 2.14: The sawtooth shape driving as function of time (black) compared to the fourier series (eq. 2.56) with 15 coefficients that is implemented in the simulations.

2.3.2 Symmetry dependence of CDT

Such a crossing of quasi energies as mentioned in the previous section, being the key to suppress the tunneling dynamics, can only occur for eigenstates belonging to different parity classes. Would the states belong to the same parity class they would form an avoided crossing, i.e., approach each other and then separate again without crossing.

Due to the generalized parity symmetry P of the Hamiltonian in eq. 2.40

$$P : \quad x \rightarrow -x, \quad t \rightarrow t + \frac{T_d}{2}. \quad (2.55)$$

the Floquet states and corresponding quasi energies can be separated into two classes. Only quasi energies belonging to different parity classes can form exact crossings, and only if the parity symmetry is fulfilled for the system. This implies that the effect of CDT depends not only on the combination of driving frequency and driving amplitude but also on the parity symmetry of the driving, i.e., the function $f(t)$. If this function does not obey the generalized parity symmetry only avoided crossings may appear.

Hence this symmetry dependence may be used to verify the realization of CDT. Experimentally it is straightforward to break the generalized parity symmetry P by changing the time dependence of the driving. Instead of sinusoidally driving with $f(t) = \sin(\omega_d t)$ a sawtooth is applied, which is still periodic in time with period T_d , but is not invariant under the translation $t \rightarrow t + \frac{T_d}{2}$. In the calculations the sawtooth dependence is implemented with a Fourier series

$$f(t) = \sum_{k=1}^{\infty} (-1)^{k-1} \frac{\sin(k\omega_d t)}{k}, \quad (2.56)$$

whereat up to 15 coefficients were taken into account, which is illustrated in fig. 2.14. The resulting quasi energy spectrum is shown on the left hand side of fig. 2.15, where the same parameters are used as for the sinusoidally driven case, which was presented in fig. 2.12. Clearly the exact crossing does not exist anymore. The tunneling dynamics still slows down a bit around a driving frequency of $\omega_d = 5\text{kHz}$, but not at all to the same amount as in the symmetric case.

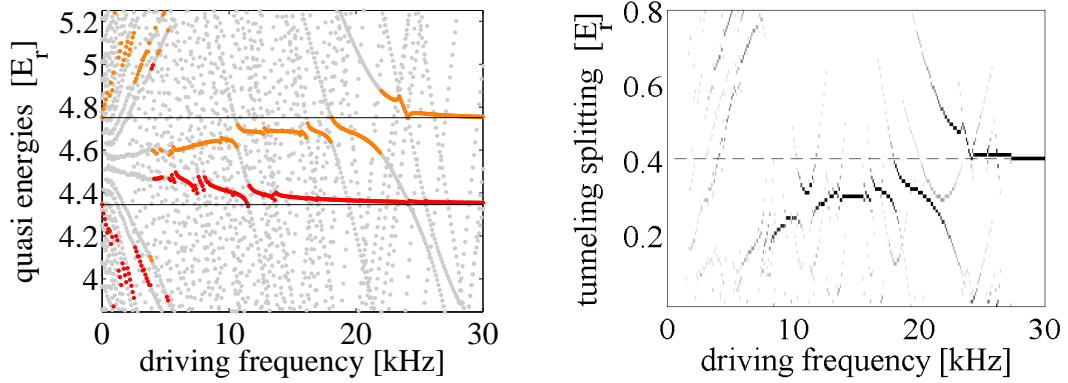


Figure 2.15: Breaking the generalized parity symmetry destroys the effect of CDT. The pictures show the quasi energy spectrum (left) and the corresponding tunneling splitting (right) for the same parameters as in the former fig. 2.12, but with a sawtooth time dependence of the driving field. As this does not comply with the generalized parity symmetry the exact crossing of the dominant quasi energies, i.e., the effect of CDT, does not occur anymore. Only a slight slowing of the tunneling dynamics around a driving frequency of 5kHz can be observed, which is not all like the immense effect of a symmetric driving force.

The corresponding tunneling splitting as function of the driving frequency is presented on the right hand side of fig. 2.15. The structure still is comparable to the symmetrically driven case in fig. 2.13, but no longer tunneling rate slower than about half of the unperturbed tunneling frequency occurs.

Another variant of breaking the generalized symmetry of the driving is to add a constant linear field to the sinusoidally oscillating driving field, so that $f(t)$ reads:

$$f(t) = \sin(\omega_d t) + d_{\text{offset}} \cdot \tilde{x}, \quad (2.57)$$

where \tilde{x} again is the distance to the symmetry point of each double well. This as well does not satisfy the generalized parity P and is experimentally realizable (cf. sec. 3.4.2).

2.3.3 Two-mode approximation

For not too strong driving forces and in the deep quantum regime the system can be simplified by assuming that only the lowest eigenstate doublet contributes to the dynamics. Following the considerations in [39] the Hamiltonian and state vector in the localized basis $|l\rangle$ and $|r\rangle$ (cf. eq. 2.1) denote as follows:

$$|\Psi(t)\rangle = \begin{pmatrix} c_1 e^{-i \frac{Sx_{12}}{\hbar\omega_d} \sin(\omega_d t)} \\ c_2 e^{+i \frac{Sx_{12}}{\hbar\omega_d} \sin(\omega_d t)} \end{pmatrix} \quad (2.58)$$

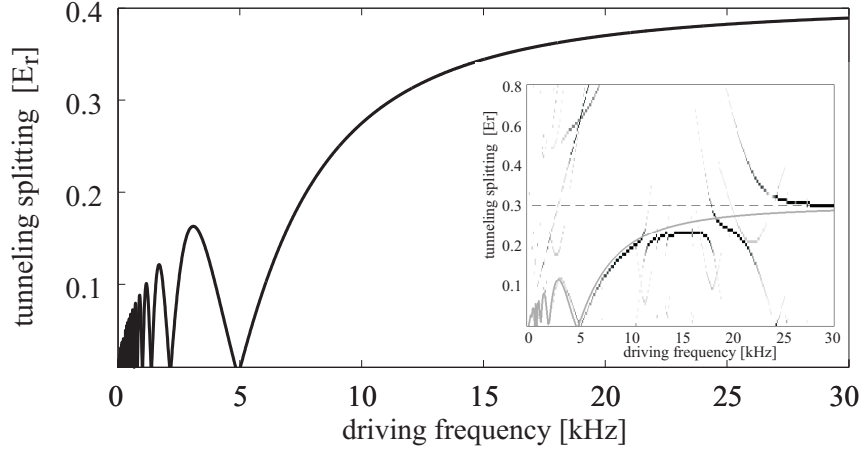


Figure 2.16: The theoretical prediction of the tunneling splitting in the two-state approximation according to eq. 2.61 plotted for typical experimental parameters. The inset shows the corresponding results of the Floquet state analysis with the two-state approximation included as solid gray line.

$$H = \begin{pmatrix} \hbar S x_{12} \cdot \sin(\omega_d t + \phi) & -\frac{\Delta}{2} \\ -\frac{\Delta}{2} & -\hbar S x_{12} \cdot \sin(\omega_d t + \phi) \end{pmatrix} \quad (2.59)$$

with x_{12} denoting the matrix element $x_{12} = \langle \varphi_1 | x | \varphi_2 \rangle$.

Setting $\phi = \pi/2$ one obtains from the Schrödinger equation:

$$i \frac{d}{dt} c_{1,2}(t) = -\frac{\Delta}{2} e^{\pm i \frac{2Sx_{12}}{\hbar\omega_d} \sin(\omega_d t)} c_{2,1}(t). \quad (2.60)$$

For large frequencies ($\omega_d \gg \Delta$) and averaged over a full period T_d making a high-frequency approximation yields an effective tunneling splitting

$$\Delta_{\text{eff}} = J_0\left(\frac{2Sx_{12}}{\hbar\omega_d}\right) \cdot \Delta, \quad (2.61)$$

whereat

$$J_0(x) = \frac{\omega}{2\pi} \int_0^T \exp[ix \cdot \sin(\omega s)] ds \quad (2.62)$$

is the zeroth-order Bessel function of the first kind. The subsequent dependence of the tunneling splitting onto the driving frequency is plotted in fig. 2.16 for the same parameters as before. In the inset the approximation is compared to the results of the full Floquet analysis, revealing that it holds for the intermediate frequency range of 5kHz to about 17kHz and can even be used to describe CDT. The resonances occurring for driving frequencies higher than 17kHz can of course not be described with this approximation. Also not in the scope of this approximation is the low frequency range for driving frequencies lower than 5kHz.

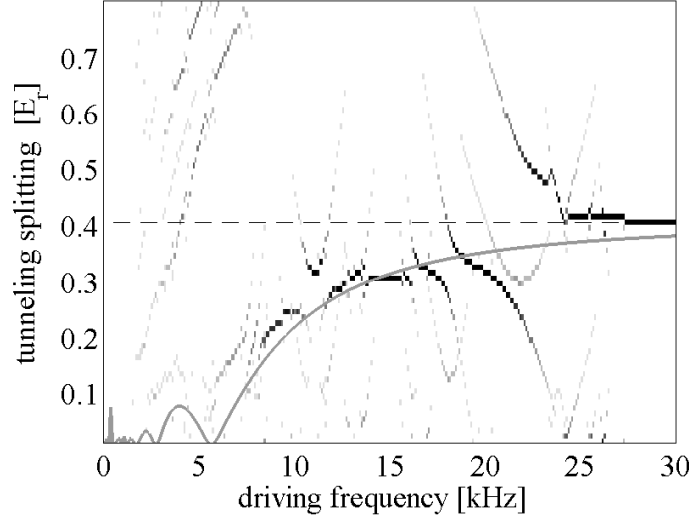


Figure 2.17: The results of the two-state approximation for sawtooth time dependence of the driving (solid gray line) is compared to the results of the full Floquet analysis (gray shading). It is obvious that for this set of parameters the approximation cannot display the dynamics as more than two states contribute in the region of the slowing of the tunneling, i.e., for driving frequencies lower than 10kHz.

For a driving force that is not sinusoidal, but sawtooth shaped, the differential equation 2.60 becomes:

$$\begin{aligned}
 i \frac{d}{dt} c_{1,2}(t) &= -\frac{\Delta}{2} e^{\pm i \frac{2Sx_{12}}{\hbar\omega_d} \sum_k (-1)^k \sin(k\omega_d t)} c_{2,1}(t) \\
 &= -\frac{\Delta}{2} \prod_k e^{\pm i \frac{2Sx_{12}}{\hbar\omega_d} (-1)^k \sin(k\omega_d t)} c_{2,1}(t).
 \end{aligned} \tag{2.63}$$

In figure 2.17 the results are compared to the findings of the full Floquet theory. It is obvious that two-state approximations does deviate massively due to the fact that there are more than two states involved in the dynamics, which is not in the scope of this approximation. Therefore only the results from the full Floquet state analysis and the findings of the split-step Fourier method described in the following section will be plotted and compared to the experimental results in the case of sawtooth driving.

2.3.4 Split-step Fourier method

Another possibility to find a solution of the time-dependent Schrödinger equation numerically is to utilize a “spectral method” called split-step Fourier [40], that is well known in quantum optics as it is the most commonly used numerical scheme for solving the nonlinear Schrödinger equation.

As stated before the dynamics of a quantum mechanical wave function can be found applying the time-evolution operator $U(t_1, t_0)$ [41], with $\Psi(x, t_1) = U(t_1, t_0)\Psi(x, t_0)$, which for a time-dependent Hamilton operator is given by:

$$U(t, t_0) = e^{-\frac{i}{\hbar}H(t-t_0)}. \quad (2.64)$$

The split-step Fourier scheme works splitting the interval $(t_1 - t_0)$ into many small time steps dt and accomplishing them alternately in real and momentum space. Therefor the Hamiltonian is decomposed into a kinetic term $K(k) = -\frac{\hbar^2 k^2}{2m}$ and a time and space dependent term $V(x, t)$, which in this case is the sum of all light-shift potentials (cf. eq. 2.32). Following the Baker-Campbell-Hausdorff formula for two not commuting operators [40, 42] the time evolution operator can be written as:

$$\begin{aligned} U(dt) &= e^{-\frac{i}{\hbar}(K(k)+V(x,t))dt} \\ &= e^{-\frac{i}{\hbar}K(k)dt} \cdot e^{-\frac{i}{\hbar}V(x,t)dt} \cdot e^{(\frac{1}{2}\frac{1}{\hbar^2}[K(k), V(x,t)]dt^2 + \dots)} \\ &\approx e^{-\frac{i}{\hbar}K(k)dt} \cdot e^{-\frac{i}{\hbar}V(x,t)dt}. \end{aligned} \quad (2.65)$$

Due to the approximation in the last step the time propagation can now be done separately for the two operators. The only condition is that the time steps have to be small enough as the dominant error is of the order of $\mathcal{O}(dt^2)$. The advantage is that the kinetic part can now be easily calculated in momentum space via fourier transformation \mathcal{F} as there it is diagonal and therefor reduced to a multiplication:

$$\Psi(x, t + dt) = \mathcal{F}^{-1} \left(e^{-\frac{i}{\hbar} \frac{\hbar^2 k^2}{2m} dt} \cdot \mathcal{F}(\Psi(x, t)) \right) = \hat{P}\Psi(x, t), \quad (2.66)$$

followed by a time step in real space:

$$\Psi(x, t + dt) = e^{-\frac{i}{\hbar}V(x,t)dt} \cdot \Psi(x, t) = \hat{R}\Psi(x, t). \quad (2.67)$$

The error made can even be reduced by symmetrizing the scheme, i.e. symmetrically splitting the operators. This is done by simply starting with a $dt/2$ step in momentum space, denoted by the operator $\hat{P}_{1/2}$, and completing the other half in the end, so that the full split-step scheme looks as follows:

$$\Psi(x, t_1) = \hat{P}_{1/2} \hat{R} \left[\hat{P} \hat{R} \right]^{N-1} \hat{P}_{1/2} \Psi(x, t_0). \quad (2.68)$$

This is the approximation after applying twice the Baker-Campbell-Hausdorff formula, so that the leading error term becomes of the order of $\mathcal{O}(dt^3)$.

One advantage of this numerical method, for example compared to finite difference schemes, is that it is very fast, as the Fourier transformations can be performed using the fast Fourier transform algorithm (FFT) [43].

The potential distribution achieved by analyzing the ccd-camera image as shown in fig. 3.6 is included to reproduce the preparation process in the calculations.

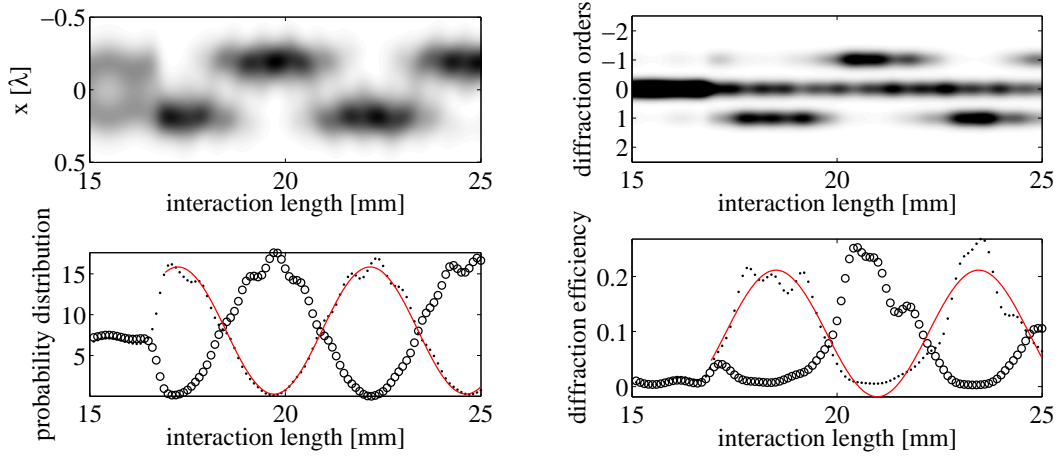


Figure 2.18: Tunneling dynamics of a particle in real space (left) and in momentum space (right) calculated utilizing the split-step Fourier method. The upper left picture shows the probability density over a complete double well, underneath the profiles are plotted for the upper (open circles) and lower (dots) well. The upper right picture displays the diffraction efficiencies for all diffraction orders and the profiles for $+1$ (dots) and -1 (open circles) diffraction order beneath (for the profiles only one row is evaluated). The periodicity of the oscillation is the same in real and momentum space as well as its starting position. The only difference is the phase. The oscillation of the diffraction efficiencies lags the oscillation between the wells in real space by a quarter of the oscillation period.

In fig. 2.18 the findings for the tunneling in an unperturbed potential, as it will be realized in the following, with $V_1 = 3.53\mathcal{E}_r$ and $V_2 = 3.98\mathcal{E}_r$ are plotted in real space as well as momentum space, revealing the equivalence of the tunneling frequency and the oscillations of the diffraction efficiencies in momentum space. The upper left picture shows the probability density for an atom in one double well as a function of interaction length, the figure beneath displays the probability density at the center of the lower (open circles) and in the upper (dots) well. The upper right picture shows the corresponding diffraction efficiencies in the different diffraction orders, whereas the lower pictures displays only the first (dots) and minus first (open circles) one. The red curves are sinusoidal fits to the data yielding a periodicity of $4.911 \pm 0.014 \text{ mm}$ according a tunneling frequency of $5.498 \pm 0.015 \text{ Hz}$ for the tunneling in real space and a periodicity of $4.942 \pm 0.035 \text{ mm}$ corresponding a frequency of $5.4634 \pm 0.039 \text{ Hz}$ for the oscillations of the diffraction efficiencies in momentum space, which is the same periodicity within the error margin. Also the starting position is the same, merely the phase is different. The oscillations in momentum space are shifted by exactly one quarter of a period, comprehensible as the atoms are prepared, i.e., localized first (first maximum of the probability density), then as the atom moves to the other well

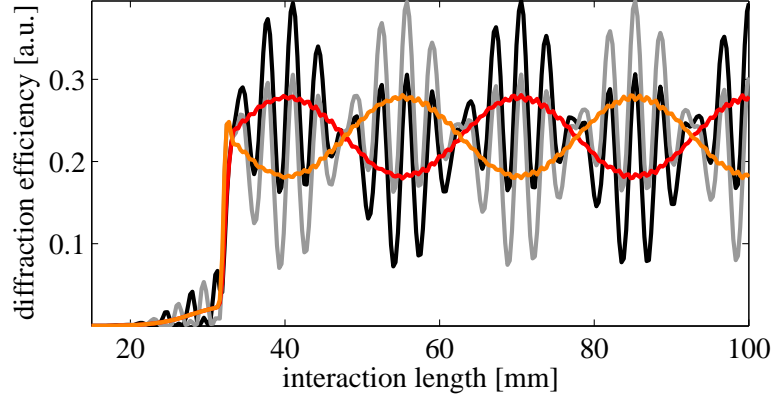


Figure 2.19: Diffraction efficiencies of the first and minus first diffraction order for an atom in a driven double well potential. In black and gray the diffraction efficiencies for one fixed initial phase of the driving at the moment the atoms enter the potential are displayed. The higher frequency that can be seen equates the driving frequency of 9kHz, which corresponds with an interaction length of 3.28mm. In red and orange the corresponding averages over all possible initial phases are depicted, which complies with the experimental reality. The fast oscillation is almost averaged out and the left over slow oscillation corresponds the tunneling dynamics.

its momentum becomes maximal and so on. Due to this the experimental setup to observe the momentum distribution of atoms in a double well potential is perfectly suited to visualize the tunneling dynamics of atoms.

Also to be seen in fig. 2.18 is the preparation phase. An imaginary potential is included into the calculations at a position of 17mm and with a waist of $350\mu\text{m}$ generating a wave packet localized in the “lower” well. Before this the wave packet is distributed equally over both wells and the resulting diffraction is symmetric and with a clear maximum in the zeroth order.

For an atom in a driven double well with $V_1 = 8\mathcal{E}_r$ and $V_2 = 2\mathcal{E}_r$ the resulting diffraction efficiencies for the first and minus first order are plotted in black and gray in fig. 2.19. The dynamics starts at 23cm of interaction length, which is the position of the absorptive potential for this calculation. The driving frequency is chosen to be 9kHz resulting in a slowing of the tunneling dynamics of about 10%. It is the envelope of the fast oscillations of the gray and black line, i.e., the slower frequency that can be observed, that accords to the tunneling frequency expected for the assumed potential heights and driving frequency. The fast oscillation matches exactly the driving frequency. A nice thing about the experimental realization is, that the initial phase of the driving at the point of time atoms enter the potential is arbitrary, so that in the experiment it is averaged over all possible phases. This corresponds to summing over all phases from 0 to 2π in the calculations yielding

the red and orange line added in fig. 2.19. Now the diffraction efficiencies do only display the tunneling frequency and do not include other information anymore.

Using the split-step Fourier method all stages of the experiment are simulated and compared to the experimental data giving good agreements. Furthermore it could be checked beforehand if the discrepancies of the experimentally realized from the theoretically studied system in [20] were supposed to yield different results.

The consequences of the continuous potential, that shall be implemented instead of one single double well, were tested this way. It can be shown that on longer time scales the localized wave packet spreads out over many wells, though nothing like this happens during the short duration of the experiments described in this work.

Moreover it was checked beforehand that the changes of the symmetry of the double wells and the differences in the preparation does not have measurable effects onto the results. In particular it could be shown that CDT should be observable with the chosen setup.

2.3.5 Comparing different methods

To compare the different methods described to simulate the tunneling dynamics the results calculated for the set of parameters used before are plotted in the same figure, namely fig. 2.20. The gray shading corresponds to the Floquet matrix method, the orange solid line represents the two-state approximation and the red dots are the fits to the results of the split-step Fourier method. As one can see the two-state approximation only holds for driving frequency bigger than the tunneling splitting Δ and smaller than the fundamental resonance $\mathcal{E}_3 - \mathcal{E}_2$. Around the latter resonance higher energy levels begin to contribute to the dynamics that are not considered in the approximation. The slight deviation of the two-state approximation compared to the Floquet matrix method in the upper picture is due to the fact, that the parameter set does not represent the deep quantum regime, as can be seen looking at the double well and its eigenstates depicted in the inset. The barrier in the middle is not very high, so that the ground state doublet is just underneath the barrier and the next eigenstate is way above this barrier.

In fig. 2.21 the numerical findings for another set of parameters matching the experiment is shown ($V_1 = 8.27\mathcal{E}_r$, $V_2 = 2.68\mathcal{E}_r$ and $S = 0.85\mathcal{E}_r$). Here the two-mode approximation (orange solid line) fits perfectly the tunneling splitting predicted by the Floquet matrix method (gray shading), at least for the driving frequency range smaller than the fundamental resonance $\mathcal{E}_3 - \mathcal{E}_2$ as expected. It can be seen in the view of this double well potential, that its barrier is much higher, so that the ground state doublet is much lower than the barrier and even the next eigenstate is just below.

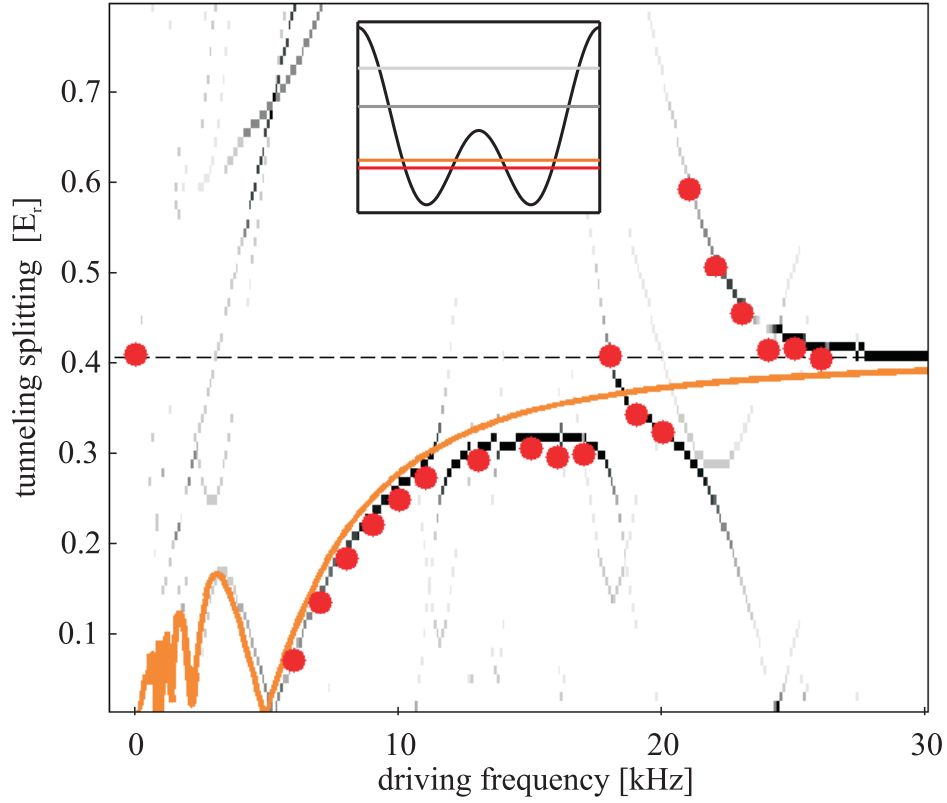


Figure 2.20: Comparing different numerical methods to solve the time dependent Schrödinger equation for a particle in a driven double well potential. The gray shading corresponds to the findings of the Floquet matrix method. The orange line represents the results of the two-state-approximation. Its deviation from the Floquet theory is a result of the fact that the parameters do not correspond to the deep quantum regime. The red dots are achieved by fitting the findings of the full integration of the time-dependent Schrödinger equation via split-step-Fourier method.

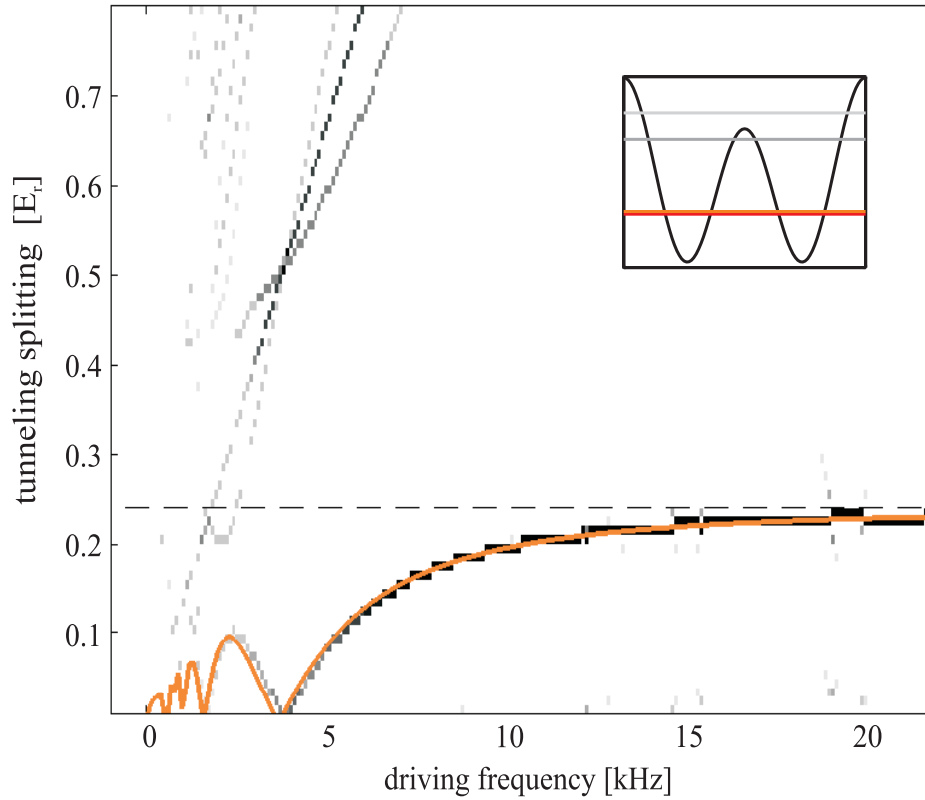


Figure 2.21: Another set of parameters being deeper in the quantum regime yield a perfect agreement of the two-mode approximation with the Floquet-state prediction for driving frequencies smaller than the fundamental resonance. This illustrates that the two-mode approximation can be employed to predict the dynamics of systems in the deep quantum regime, at least for driving frequencies in the range $\Delta < \omega_d < \mathcal{E}_3 - \mathcal{E}_2$.

Chapter 3

Experimental realization of ac-control of single atoms

3.1 Experimental setup

Since the physics described in this work is one dimensional a traditional well collimated atomic beam is perfectly suited as a particle source. It allows the examinations of quantum phenomena in an interaction free, i.e., linear regime. It is chosen argon ^{40}Ar , which as a noble gas is not reactive. Besides it exhibits a simple level scheme, since it owns no hyperfine structure due to its even-even nucleus. Furthermore a metastable state is chosen to function as ground state in the experiment, which is possible as its lifetime is significantly longer than the duration of the experiments. The specific state is selected due to the fact, that there are hardly no commercial laser systems available with a wavelength of about 100nm, which would match appropriate cooling transitions from the ground state of the argon atom. Up to now free-electron-lasers, e.g., at the linear accelerator TESLA [44], are the only source providing at least a viable wavelength, even though only in a pulsed form. Moreover the excitation energy of about 12eV of this metastable state allows a spatially resolved single particle detection using a micro-channel plate (MCP). Certainly the most relevant reason to choose argon for the experiments described in this work is the possibility to realize an open two-level system using the selected state $1s_5$. This state provides a feasible closed transition ($1s_5 \rightarrow 2p_9$) for laser cooling at $\lambda_L = 811\text{nm}$, where a whole lot of laser systems is available. Additionally imaginary optical potentials [28, 29] (cf. sec. 2.2.1) can be realized using resonant light at $\lambda_{\text{abs}} = 801\text{nm}$. This transition ($1s_5 \rightarrow 2p_8 \rightarrow 1s_2 \rightarrow 1s_1$) transfers the metastable state via some other states to the absolute ground state, which does not own the energy to be detected by the MCP and thus this transition is employed to “absorb” atoms from the experiment. The light-shift potential with 801nm light is therefor called absorptive potential V_{abs} in the following. A reduced level scheme showing the transitions that are relevant for the experiment is depicted in fig. 3.1.

For the atomic states the Paschen notation [45] is chosen. It does not reflect

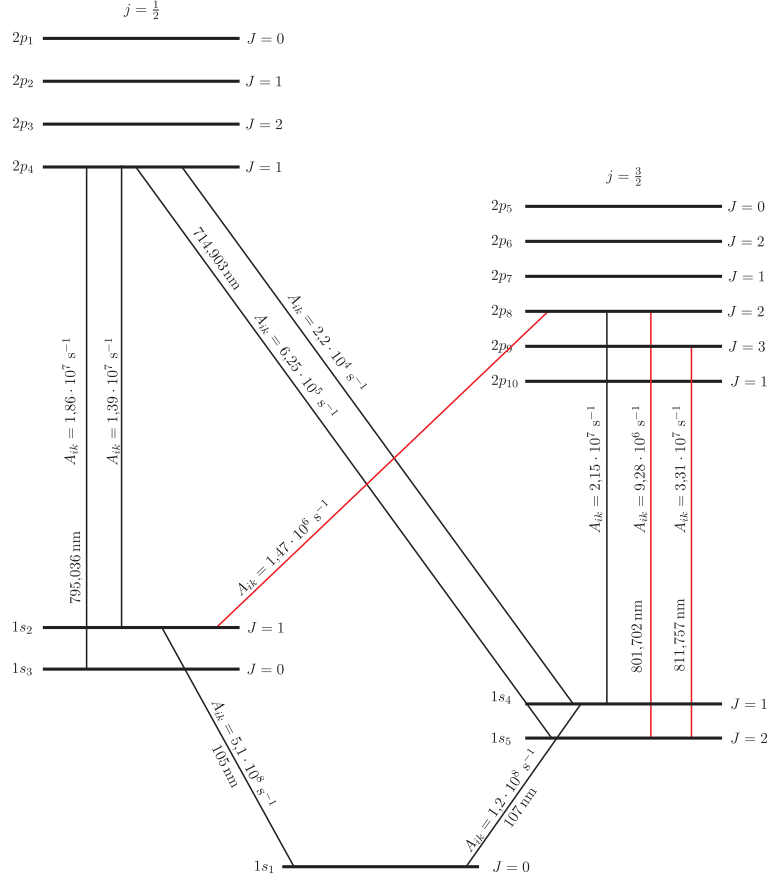


Figure 3.1: Reduced level scheme of ^{40}Ar in Paschen notation. The states $1s_5$ and $1s_3$ are metastable. A_{ik} denote the Einstein coefficients. The relevant transitions are indicated in red, at which $1s_5 \rightarrow 2p_9$ is a closed transition used for cooling and $1s_5 \rightarrow 2p_8$ is open and used for absorbing atoms.

the exact electronic configuration of the states but is a simplification often used as it only displays the essential information like energy and selection rules, i.e., the quantum number ruling the selection rules for dipole transitions. The sublevels are numbered serially following decreasing energy. The selection rules are reflected in the nomenclature as transitions between s and p are allowed, those between s and s or p and p are forbidden.

Since Argon is a heavy noble gas and therefore the distance of the excited electron to the core is very large, the LS -coupling scheme provides no good approximation. The energy levels depicted result from the more appropriate Racah- or jL -coupling. Like a quasi-one-electron-atom the angular momentum l of the valence electron couples to the total angular momentum j of the ion given by the coupling of its angular momentum L and its spin S . As the total angular momentum of the ion can

either be $j = \frac{1}{2}$ or $j = \frac{3}{2}$ the level scheme splits into two branches between which weaker transitions are possible.

The aperture to create a beam of slow and coherent metastable argon atoms is described in detail in [46], for completeness a summary is added in the appendix A.

To increase the time the atoms propagate through the light-shift potential their velocity is reduced to maximally $30 \frac{m}{s}$ by increasing the magnetic field of the Zeeman slower (see appendix A). This causes a serious decrease of the atomic flux primarily as a result of the fact that the diameter of the atomic beam as well as its divergence, i.e., the transversal velocity of the atoms leaving the zeeman slower is significantly increased as well as the number of atoms that turn around. Hence not all atoms leaving the Zeeman slower enter the funnel unit due to the finite size of the entrance opening. This could be partly compensated by increasing the flux density of the atomic beam due to a higher laser power in the cooling process, i.e., in the collimation stage and the zeeman slower and by widening the differential pumping stage between the collimation stage and the high vacuum part of the machine.

3.1.1 Coherence of the atomic beam

The coherence of the atoms is crucial to see any diffraction effects of the atoms. The smallest angle to be resolved in the experiment is half the Bragg angle $\theta_B = \lambda_{dB}/\lambda_L$. For atoms with a velocity of $v = 30 \frac{m}{s}$, which corresponds to a de Broglie wavelength of $\lambda_{dB} = 333pm$, and a standing light wave with $\lambda_L = 811nm$ this results in $\theta_B = 410\mu rad$, so that the transverse divergence must be smaller than $205\mu rad$. This is achieved utilizing two slits strongly confining the beam horizontally. As this goes along with a great loss of atoms the beam intensity beforehand has to be appropriately high. At the first slit with a fixed width of $d_1 = 25\mu m$ the atoms are diffracted yielding a cone of phase coherent atoms in the zeroth diffraction order. The second slit with a variable width $d_2 = 0 - 40\mu m$ follows after a distance of $l = 25cm$ to further decreases the width of the atomic beam. The final divergence angle of the atomic beam therefore results in $\beta = (d_1 + d_2)/l$. To be smaller than the required $205\mu rad$ the experiments were realized with $d_2 = 20\mu m$ giving a divergence angle of $180\mu rad$ (FWHM) and yielding an atomic beam that illuminates about 27 double wells of the continuous double well structure.

The beam divergence cannot be decreased arbitrarily reducing the width of the second slit d_2 due to diffraction effects appearing. For a width that is smaller than $d_2 < 5\mu m$ the width of the atomic beam begins to magnify again [26]. Furthermore for a better resolution of the diffraction orders on the MCP the distance the atoms propagate freely after leaving the light-shift potential and before hitting the detector was increased to 1m compared to earlier works with this atomic beam machine.

To preclude influences of magnetic stray fields, e.g. appearing in the vicinity of stepper motors used to adjust the mirror positions of the double well setup two strong permanent magnets are added outside the vacuum. Their magnetic field gradient is strong enough to deflect all atoms not in the substate $m_j = 0$, so that they do not reach the detector. Of course a great disadvantage is that 4/5 of the

atoms get lost that way, but the atomic beam reaching the detector is not blurred out anymore.

Another important influence on the coherence of the beam has the velocity distribution of the atoms. It has two effects onto the resolution of the diffraction orders. One is that the different velocities yield different distances of the orders, which means that the diffraction orders are broadened and this broadening increases linearly with the order. The coherence length, i.e., the number of diffraction orders that can be resolved, can be evaluated due to the width δv of the velocity distribution of the atoms in the beam:

$$l = \frac{\langle \lambda_{\text{dB}} \rangle^2}{\delta \lambda_{\text{dB}}} = \lambda_{\text{dB}} \frac{v}{\delta v} \quad (3.1)$$

As the interaction time of the atoms with the potential is adjusted by changing the width of the potential, the velocity distribution of the atoms has another crucial influence onto the measurements. Due to different velocities the atoms passing a standing wave of a certain length experience different interaction times, so that diffraction patterns for those different interaction times interfere with each other. For the tunneling dynamics to be observed here this means, that the oscillations between + and – first diffraction order smear out with increasing interaction time, i.e., increasing length of the potential.

3.1.2 Detection

To increase the resolution of the MCP-detector it is installed under an angle of 10° in respect to the axis along the beam propagation as depicted in fig. A.3 in the appendix. This yields an effective resolution of $17.2\mu\text{m}$ the total width being 256 pixel on a 1in diameter. As the detector is not perfectly orientated (angle in respect to axis) and the readout of the spatial position via a resistive anode is not at all aligned along this axis the resulting distortion of the data has to be corrected by first rotating the image to get a perpendicularly oriented image of the slit and than shearing it, so that the diffraction orders are at the same height as the slit, i.e., the zeroth order (see fig. 3.2). Then the diffraction efficiencies of the different orders are deduced by summing up the detected number of atoms in the corresponding angular windows.

3.2 Double well structure

The periodic arrangement of double wells is achieved employing standard light shift potentials (cf. sec. 2.1.1 et seq.). The incoming far red-detuned light beam is split into two beams utilizing an acousto optical deflector (AOD, IntraAction corp., ADM.4024) and then those beams are retro reflected by two gold mirrors as depicted in fig. 3.3. The first one is shone in onto mirror 1 at right angle forming the potential V_1 with periodicity $\lambda_L/2$ in x-direction. The second one is added impinging onto mirror 1 under an angle of $\alpha = \pi/3$ in respect to the first one, yielding a periodicity of $\lambda_L/(2\cos(\alpha)) = \lambda_L$ for the potential V_2 . The symmetry of the resulting double

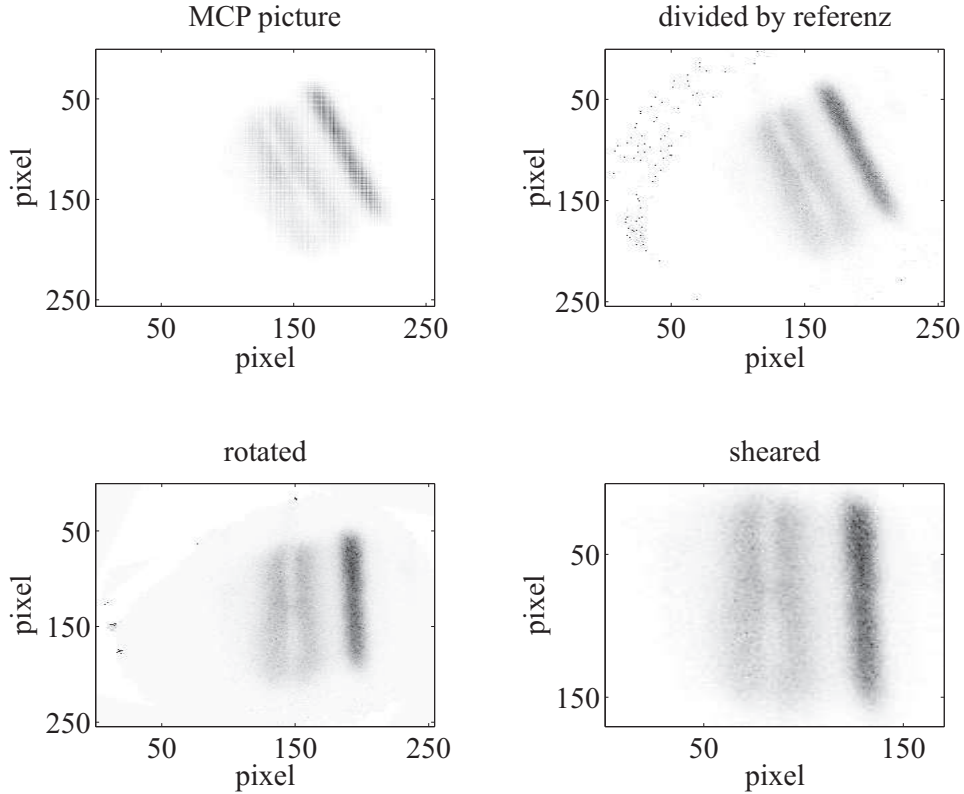


Figure 3.2: Illustration of the data processing. The pictures measured with MCP are divided pixel-wise by a reference to correct inhomogeneities. Then they are rotated such that the image of the slit, i.e., the zeroth diffraction order, is oriented perpendicular. At last the pictures are sheared so that the all diffraction orders are at the same height as the zeroth order.

well is critically depending on the angle α . A minimal deviation from those $\pi/3$ yields an asymmetry of the wells depending on the distance from the mirror surface (cf. fig. 2.2). To have a sensitive and direct control of this important parameter a realization employing the AOD and a fixed second mirror is chosen. Moreover this enables the possibility to implement the driving by simply changing the AOD frequency periodically. The relation between the change of this angle and the resulting driving amplitude is given by eq. 2.41.

The two light beams are strongly expanded in horizontal direction and only the central part of the Gaussian beam profile is used in the experiment, so that the intensity varies not more than 10%. The first idea to realize the adiabatic preparation was to directly use the slow increase of the intensity of such an expanded beam, which was not compatible with the installed gold mirror, as the increase of the intensity is not only much slower than needed for adiabaticity, but it is far too long for the dimensions of the mirror. Therefore all but the center of the beam was

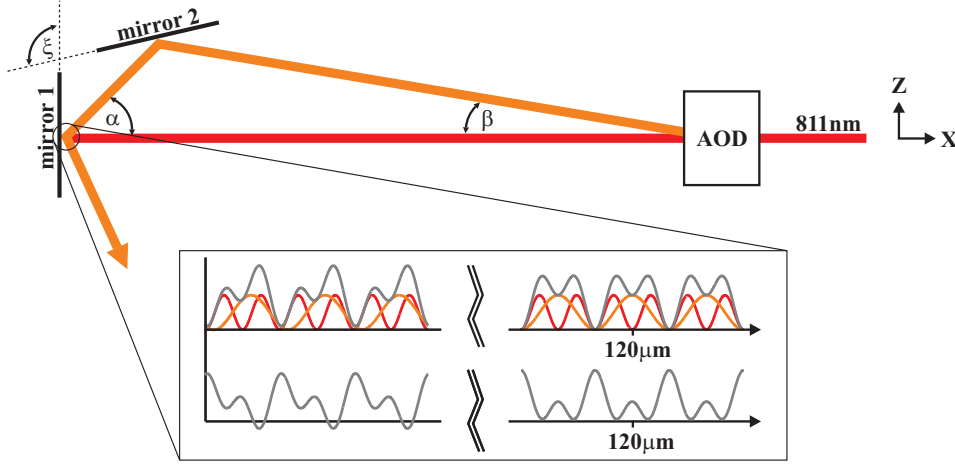


Figure 3.3: Creating the double well potential. The beam of 811nm light is split by an acousto optical deflector and reunited under an angle of nearly $\alpha = \pi/3$ forming a continuous series of double well potentials. Due to the different phase shifts, the two parts gain at the mirror surface, the angle is adjusted the way, that in a distance of $120\mu\text{m}$ from the mirror, where the atoms enter the potential, the double wells are symmetric as depicted in the inset.

blocked and a specially designed filter was integrated to realize the adiabatic slope, that will be discussed in sec. 3.3.2.

To observe the dynamics of the atoms in the potential the interaction time is changed by varying the width of the standing light waves along the propagation direction of the atoms utilizing a razor blade mounted on a stepper motor.

The AOD is designed for maximal diffraction efficiency at 40MHz resulting in an angle of $\beta = 8.125\text{mrad}$ between the undisturbed and the diffracted beam for 811nm light and a bandwidth of about 20MHz. A change of $\pm 1\text{MHz}$ at the AOD modifies the angle α by $\pm 203\mu\text{rad}$. To be able to run the AOD as close as possible to those 40MHz the angle between the two mirrors had to be adjusted to an angle of $\xi = \frac{2}{3}\pi - \frac{\beta}{2} = 2.0903\text{rad}$. This was adjusted beforehand outside the vacuum utilizing a goniometer (Newport, M-BGM50) and with an accuracy of $70\mu\text{rad}$ (for details see [47]).

For a perfectly symmetric double well the ratio of the two periods of the potentials V_1 and V_2 should be exactly 2 to 1. This means for an angle of exactly $\pi/3$ the beat period P between the potentials becomes infinitely large, a deviation however yields a finite beat period. Analytically the correlation between the beat period and the angle α is given by

$$P = \frac{\lambda_L}{2} \left(\frac{1}{1 - 2 \cos \alpha} \right). \quad (3.2)$$

Hence this should be a way to perfectly adjust this angle α . Therefor an interferometric setup is used by positioning the two potentials one right after the other in the

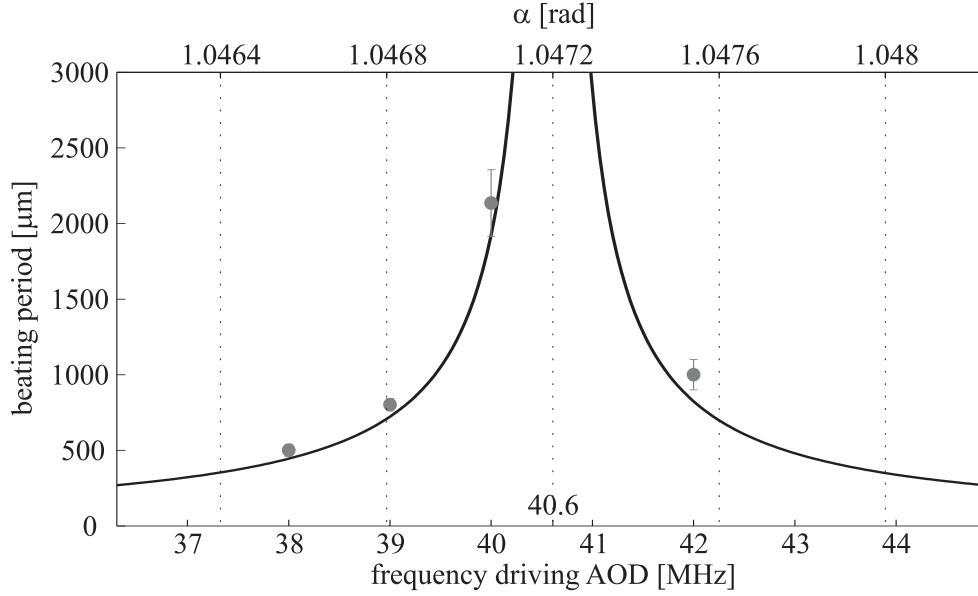


Figure 3.4: Beat period of the two standing waves forming the continuous double well potential plotted against the rf-frequency at the AOD defining the angle α between them. The solid line corresponds to the analytical expression in eq. 3.2.

atomic beam direction. That way atoms are diffracted by either of the two potentials and the first diffraction order of potential V_1 interferes with the second order of V_2 . Now the diffraction efficiency of this order depends on the phase between the standing light waves and can be measured against the mirror position (distance of the atomic beam from the mirror), i.e., the beat period can be sampled “moving” the atomic beam along the standing waves. In fig. 3.4 The measured periods are plotted against the rf-frequency driving the AOD. The theory (solid line) can be fitted to the data points, so that the resulting frequency giving an angle of $\alpha = \pi/3$ is hereafter about 40.6MHz.

3.2.1 Working with a real mirror

Unfortunately this counts only for a perfect node at the mirror surface for both standing light waves. As the gold surface is no perfectly ideal conductor (neither is its SiO coating) the standing light waves do not have a node ($\phi = 0$) exactly at the mirror surface but will experience a phase shift. This phase shift depends on the angle of incidence and the polarization of the impinging light and because of the former it is not equal for the two potentials $V_{1,2}$. To minimize the resulting phase shift between the two potentials the polarization is chosen perpendicular to the plane of incidence. Still the resultant double wells are not perfectly symmetric. Their asymmetry does not depend on the position, because it is due to a constant

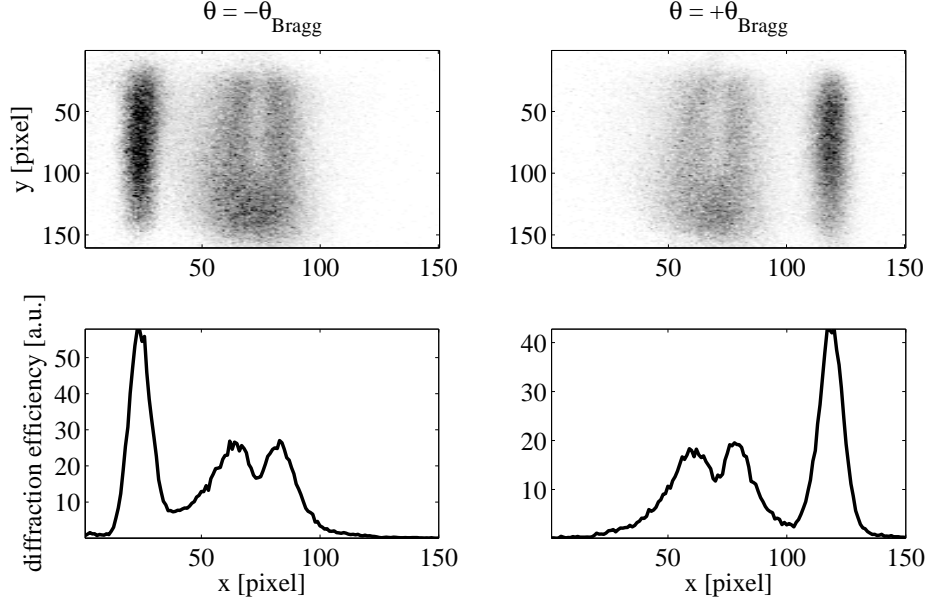


Figure 3.5: Adjusting the perpendicular incidence of the atoms onto the standing light wave via Bragg diffraction. The upper plots show the rotated and sheared picture, measured with the MCP/RAE Detector. The lower plots show the profiles, achieved by summing over some rows of the upper pictures.

phase shift. To compensate for this asymmetry the angle α is adjusted the way that in the distance from the mirror surface where the atoms pass the potential the double wells are symmetric, which is indicated in the inset of fig. 3.3. The procedure aligning the double wells and the atomic beam will be described in the following.

A theoretical estimation of the diffraction at the gold mirror surface can be done following Fresnel's equations [33] and yields a relative phase shift between the two standing waves of $\Delta\varphi = 0.1844$ for a polarization perpendicular to the plane of incidence and $\Delta\varphi = -0.3762$ for parallel polarized light waves [48, 49]. Experimentally the phase shift for perpendicularly polarized light was determined to be approximately $\Delta\varphi_{\text{exp}} = 0.1153$.

3.3 Single particle tunneling

Before introducing the driving field the accuracy of the initial state preparation is analyzed, i.e., it is tested if stationary Floquet states are prepared and the tunneling dynamics of the atoms in an unperturbed double well is investigated.

3.3.1 Bragg Scattering

The perpendicular incidence of the atoms onto the standing light wave, i.e., the parallel alignment of mirror 1 and the atomic beam is achieved utilizing standard Bragg scattering. This effect critically depends on the angle of incidence of the atoms onto the light wave as explained in sec. 2.2.3. The retro reflected 811nm light forms a light crystal, that can be tilted in respect to the atomic beam via a piezo crystal on which the gold mirrors are mounted. The mirror position (angle) is monitored using a resistive strain gauge, so that no effects due to hysteresis falsify the results. The mirror is positioned that way that Bragg diffraction into the +1. and then into the -1. diffraction order is observed as shown in fig. 3.5. Then it is repositioned to the mean value of those two settings, which corresponds to a parallel alignment of atomic beam and mirror with an accuracy of about 5% of the Bragg angle ($\theta_{\text{Bragg}} = 410\mu\text{rad}$ for a velocity of $v_{\text{atom}} = 30\frac{\text{m}}{\text{s}}$) [47]. The selectivity of the Bragg acceptance angle arising from the dynamical diffraction theory [29] allows this accuracy.

As the optics setup outside the vacuum was not as stable as the gold mirror position inside, the perpendicular incidence of the standing wave forming the potential V_1 was regularly tested and if necessary readjusted throughout the measurements by coupling the retro reflected light back into the fiber that originally transfers the light to the experiment and optimizing the intensity at the other end.

3.3.2 Adiabaticity

The light intensity profile along the atomic beam is shaped with a specially designed optical gray filter such that the motion of the atoms follows adiabatically the light shift potential. Employing a ccd-camera the intensity distribution of the light is measured. Therefor the light beams are deflected by a temporarily inserted mirror the way that they impinge on a scaled screen after covering the same distance as if impinging on mirror 1. Hence the position in the y -direction of the absorptive potential (dark spot) can be controlled that way as well as the slope of the two potentials forming the double well structure. Such a ccd-camera image is shown in the upper left part of fig. 3.6(a). The lower graph of the same figure shows the intensity profile of the three standing waves in y -direction revealing the slow increase of the potentials $V_{1,2}$.

The preparation of the ground state was tested by monitoring the propagation of the atoms in a double well potential with the absorptive potential switched off. As the ground state is a stationary state no dynamics at all is expected after the preparation process, i.e., after the potential reached its constant maximum. For the experimental setup this means that there is some diffraction efficiency to be observed into the first diffraction orders, but leveling at a constant value. The results showing the adiabaticity of a realized double well potential are presented in fig. 3.6(b).

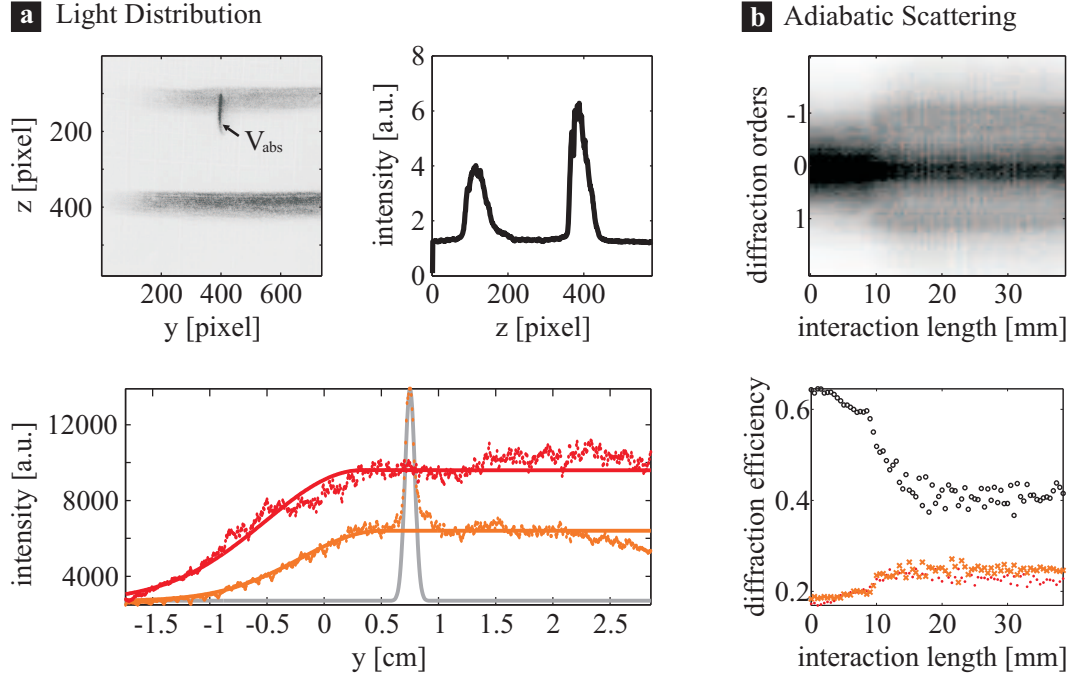


Figure 3.6: (a) Adiabatic beam profiles. The upper left picture shows the ccd-camera image of the three light beams. The lower beam corresponds to V_1 , the upper beam to V_2 . The imaginary potential, i.e., the 801nm light, is indicated with an arrow. The upper right picture displays a perpendicular cut of the ccd-camera image. In the lower picture the profiles, i.e., horizontal cuts, reveal the slow increase of the intensities, the position of the imaginary potential right after the slope and the following constant plateau. (b) Testing the adiabaticity of the double well potential. The absence of any dynamics in the diffraction orders after leveling demonstrates the preparation of the stationary ground state.

3.3.3 Imaginary potential

The initial state of atoms localized on one side of each double well only is achieved by absorbing the atoms in every second well via an imaginary potential (cf. sec. 2.2.1). Therefore a short standing light wave of 801nm light is positioned right after the adiabatic slope of the double well potential as can be seen in the lower graph of fig. 3.6(a). The periodicity of this potential has to be aligned the way that its minima coincide with every second well of the double well potential. This is attained by shining the light in under an angle, like it is done for the potential V_2 and shown in fig. 3.7. The right adjustment of this angle is achieved by measuring the dependency of the near field distribution of the atoms onto the mirror position, i.e., the distance of the atoms to the mirror surface. The principle idea is sketched in fig. 2.8. As the mirror is moved the atoms scan along the two potentials, so that the total atom

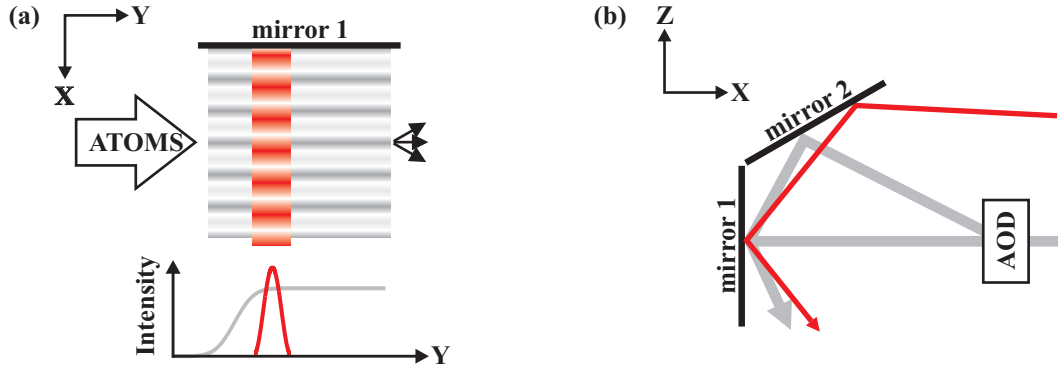


Figure 3.7: Introducing the imaginary potential. (a) Right after the adiabatic slop of the double well potential the atoms pass the imaginary potential of about $600\mu\text{m}$ width (FWHM). (b) To achieve the right periodicity the 801nm potential is fed in under an angle alike the potential V_2 .

number only depends on the relative phase between the double well structure and the absorptive potential. Again because of the phase shift at the gold mirror surface this is not totally true. As to cope for this the angle α is not perfectly $\pi/3$, so that the shape of the double wells also depends on their distance to the mirror surface. For the experiments the angle is adjusted such that only at a distance of $x = 120\mu\text{m}$ the double wells are perfectly symmetric. Still two maxima in the total atom number can be observed as they are indicated in the sketch, but their heights will never be the same for this experimental realization. Nevertheless this technique can be used to find the mirror position for the optimal preparation of the initial state, i.e., the best alinement of double wells and absorptive potential, which corresponds to the position of the maxima. In fig. 3.8 the measured data are compared to the calculations done following the diffraction method showing a perfect compliance of the transmission profiles. The fact that in the measurement the zeroth order is hardly not present is due to a very strong absorptive potential.

3.3.4 Potential heights

The potential heights are calibrated separately. For the potential with periodicity $\lambda/2$ the oscillations inside the potential are measured by projecting the atoms onto many eigenstates, i.e., by switching on the standing light wave abruptly. The resulting oscillation of the width of the wave packet yielding oscillations between the first diffraction orders and the zeroth order can be seen on the left hand side of fig. 3.9(a). They are compared to the numerical solutions found utilizing the Bloch-wave ansatz to determine the height. The damping of the measured diffraction efficiencies is due to the longitudinal velocity distribution of the atoms.

As the diffraction efficiencies for the potential with periodicity λ are significantly smaller for perpendicular incidence, another method is chosen to measure its

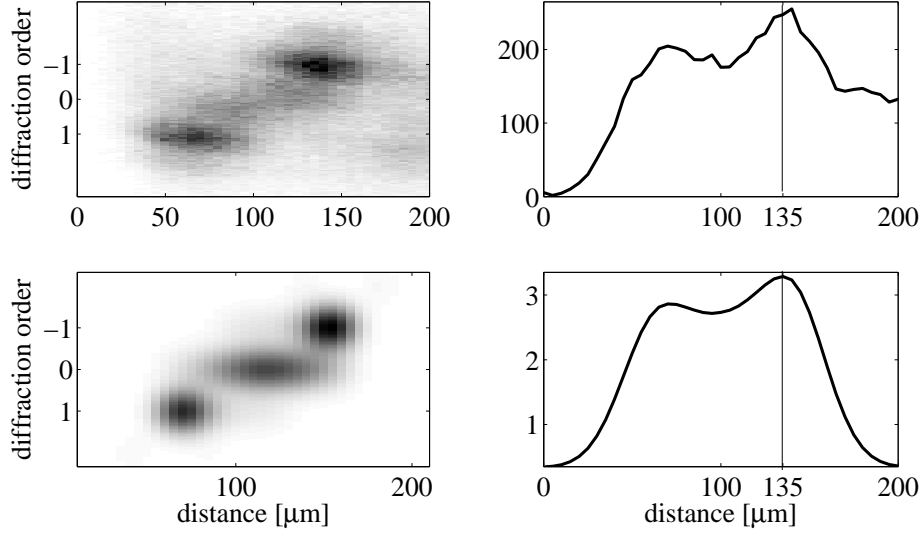


Figure 3.8: Comparing experimental findings of the near-field measurements (upper pictures) with theoretical predictions (lower pictures). On the right hand side the total transmission against the distance from the mirror is plotted. The corresponding diffraction efficiencies of the different diffraction orders are depicted on the left.

potential height. Therefor the atoms are primarily loaded into the ground state by switching on slowly. Then a wave packet is prepared, that is localized on one side of a potential well by absorbing everything on the other side using the absorptive potential phase shifted against the light shift potential. The swashing of the wave packet around the potential minimum results in oscillations between the $+1$. and -1 . diffraction order as for a tunneling particle, only the time scale is much faster. Measurements are presented on the right hand side of fig. 3.9(a).

The potential heights are adjusted such that the lowest eigenstate doublet is well below the barrier and the next eigenstates are slightly below or even above the barrier as shown in fig. 3.9(b). This guarantees that the dynamics observed is tunneling, but the tunneling time is feasible, though this does not guarantee to be in the deep quantum regime, i.e., the two-state-approximation is not necessarily applicable.

3.3.5 Symmetry of the double well potential

Since the method of measuring the beating of the two light shift potentials forming the double well fails, as explained in sec. 3.2, the best way to test the symmetry is via the tunneling dynamics of the atoms. After measuring the potential heights the tunneling periodicity expected for a symmetric potential is easily calculated due to its eigenenergies (cf. sec. 2.1). The actually measured tunneling periodicity can now

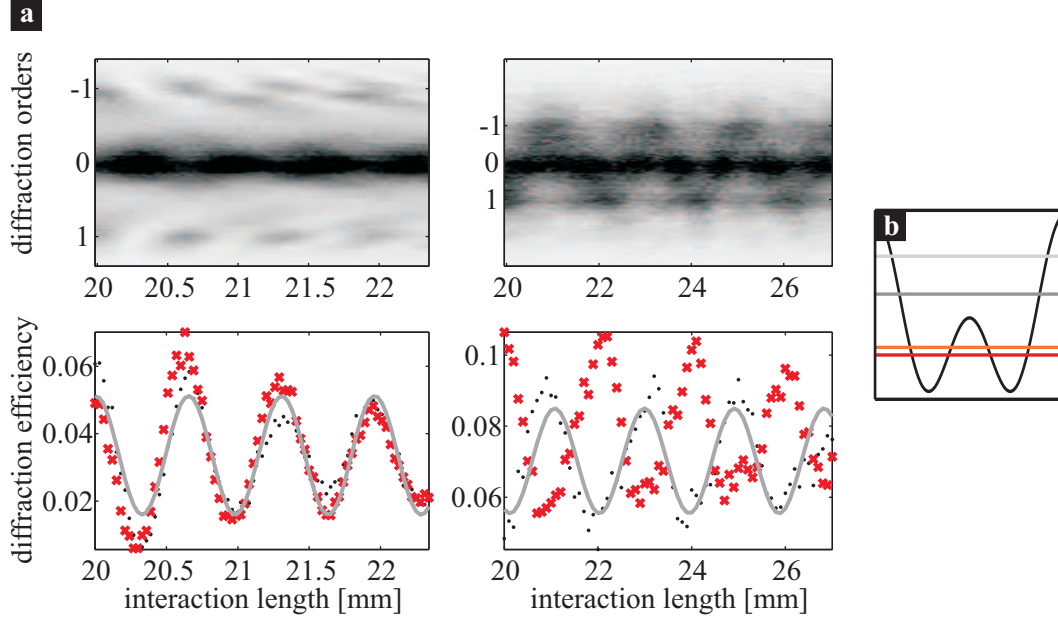


Figure 3.9: (a) Measuring the potential height. The upper pictures show the measured diffraction efficiencies for an atom prepared in an excited state in the potential V_1 (left) and swapping around the potential minimum of V_2 (right). In the lower row the fits to the profiles of the -1 . diffraction order is shown as solid gray line. (b) The resultant potential heights are $V_1 = 6.25\mathcal{E}_r$ and $V_2 = 5.40\mathcal{E}_r$, corresponding to a double well with the first doublet below the barrier and the next one above.

be compared to this prediction and only if they are consistent a symmetric double well is realized. For an asymmetry the tunneling periodicity will always be faster compared to the symmetric case and already for small aberrations this decrease of the tunneling time is significant as shown in fig. 2.5.

As this is a quite time consuming method, it is used for the fine-tuning. A first guess for the angle realizing symmetric double wells in the appropriate distance from the mirror can be made by analyzing the diffraction of an atom by a double well potential with abrupt rise and fall. If the double well structure is symmetric, minus and plus first diffraction orders should have the same efficiency. For an asymmetric double well there will always be an imbalance between the two sides.

There are more characteristics giving information about the symmetry of the double wells, e.g. the phase shift between the oscillations of $+1$. and -1 . diffraction order. For a perfectly symmetric potential this should be exactly π . For asymmetric double wells it differs depending on the asymmetry as plotted in fig. 3.10.

Influence of the AOD frequency onto the tunneling time

A difficulty using the tunneling frequency as indicator for the symmetry of the double well is that changing the AOD frequency, i.e., changing the angle α to adjust the

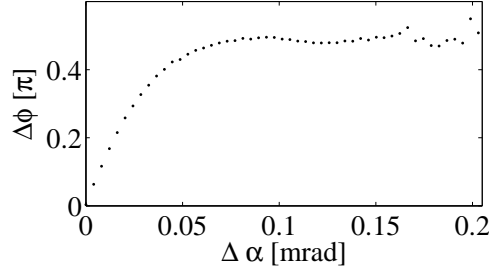


Figure 3.10: The dependence of the phase shift between the two potentials V_1 and V_2 on the angle they enclose can be used as indicator for the symmetry of the emerging double well potential. Plotted is $\Delta\phi = \phi - \pi$ against $\Delta\alpha = \alpha - \pi/3$.

symmetry also means changing the position in z-direction of the potential V_2 . This means that changing the AOD frequency also changes the potential height of V_2 that is seen by the atoms. Hence it is not possible to directly compare the tunneling period for a new AOD-frequency with the old predictions, but the potential height V_2 has always to be determined anew. A systematic analysis of this effect is presented in [50].

3.3.6 First visualization of single particle tunneling

The first observation of the tunneling of single particles is presented in fig. 3.11. It shows the tunneling dynamics in momentum space, i.e., the diffraction orders (upper row) and efficiencies (lower row) as a function of the length of the double well potential since for the measurements it is this length that is changed to scan the time of the atoms in the potential. The shown pictures start before the particle is prepared on one side of the potential, which is why the diffraction efficiencies on both sides of the zeroth order are quite the same in the beginning. Not until the position of about 17mm the preparation process is completed and the tunneling dynamics starts indicated by the out of phase oscillation of the efficiencies of plus and minus first diffraction order. The measured data is depicted on the right hand side, a numerical simulation via split-step-fourier method without free parameters on the left. One can see a very good agreement of the experimental findings with the theoretical prediction.

3.3.7 First systematic measurements

As a first test of the setup a systematic analysis of the tunneling period is done showing the good control of the symmetry and shape of the potential. Therefor the tunneling period is measured as a function of the ration $V_1/(V_1 + V_2)$, i.e., as a function of the amplitude of the voltage supplied to the AOD. That way pretty different double well structures are created from very small barrier heights to large

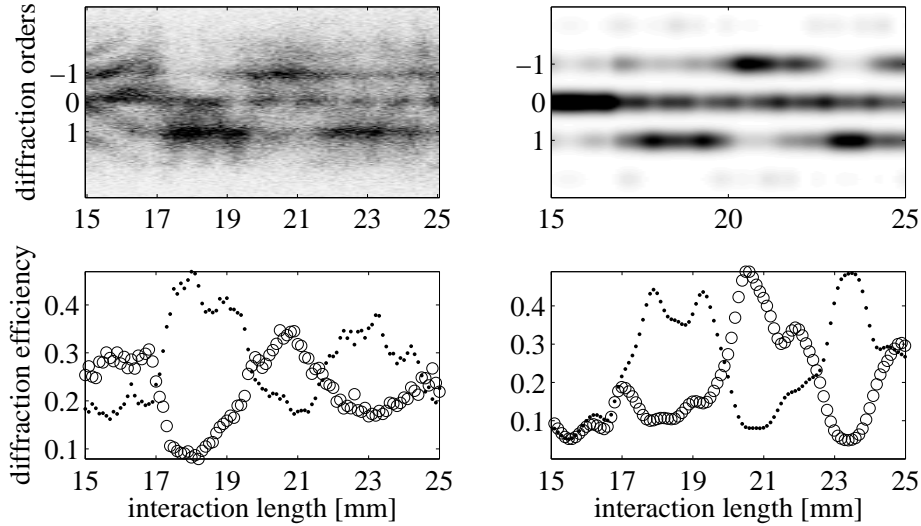


Figure 3.11: First signal of an atom tunneling in a double well light shift potential. The upper left picture shows the measured diffraction orders as function of the width of the double well potential in a gray shading corresponding the efficiencies. At a position of about 17mm the preparation process is completed and the tunneling dynamics begins, which can be discerned as the efficiencies of plus and minus first diffraction order (plotted in the lower picture) start oscillating π out of phase. On the right hand side the results of the simulations with the split-step Fourier method without free parameters are depicted.

barriers. This is done for three different total light intensities $V_{\text{total}} = V_1 + V_2$ and compared to the theoretical prediction as shown in fig. 3.12. From the left to the right the barrier is increased, so that the first data points on the left of the plot are strictly speaking no tunneling signal, but the frequency of an atom swapping over a small hump in the middle of a potential well, because the lowest eigenstate doublet of the corresponding double well potential is not below the barrier. Only increasing the ratio of V_1 this devolves into “real” tunneling.

Remarkably it turns out that in the case of symmetrically realized double wells all the curves for different total intensities intersect in a small region close to a ratio of $0.4 \frac{V_1}{V_{\text{total}}}$. As for a higher total potential V_{total} the oscillations at the bottom of the “barrier free” potential (V_1/V_{total} small) are faster, i.e., the tunneling period smaller, but for a high ratios V_1/V_{total} the barrier becomes larger, so that the tunneling period is longer compared to a smaller total potential, those curves have to intersect. That this happens for almost the same ratio is fortunate, as this is not the case for asymmetric double wells, where the crossing points of different curves occur for higher ratios and are spread over a greater range, so that this crossing points can act as an indicator for the symmetry of the double well. This is illustrated by the

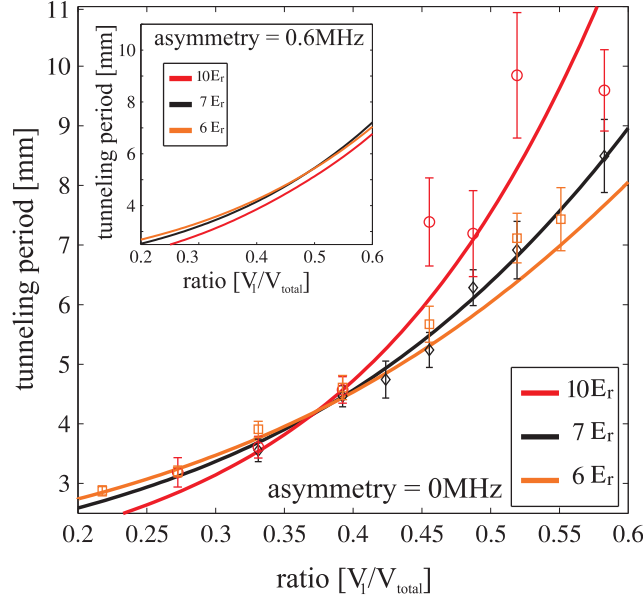


Figure 3.12: The tunneling period is measured as a function of the ratio between V_1 and V_2 for different absolute values of $V_{total} = V_1 + V_2$. The curves represent the theoretical predictions and show that for a symmetric realization of the double wells all curves intersect in one point. The inset shows the theoretically found curves for the same potential heights but with a slight asymmetry of double wells, where no mutual point of intersection appears anymore.

inset of fig. 3.12 where the theoretical predictions for the same total light intensities as before but with an asymmetry are shown. The asymmetry is implemented by increasing the angle of incidence α of the potential V_2 by a value that accords to an increase of the frequency driving the AOD by 0.6MHz compared to the symmetric case. The theoretical curves are obtained by the diffraction method (cf. sec. 2.2), whereat it is accounted for the fact that only 95% of the intensity deflected by the AOD contributes to the potential as arises from other measurements.

3.4 AC-driving

In the following the experimental findings for the frequency dependence of the tunneling splitting as well as the amplitude dependence are compared with the full Floquet analysis, the two-mode approximation and the full numerical solution of the time-dependent Schrödinger equation via split-step Fourier method.

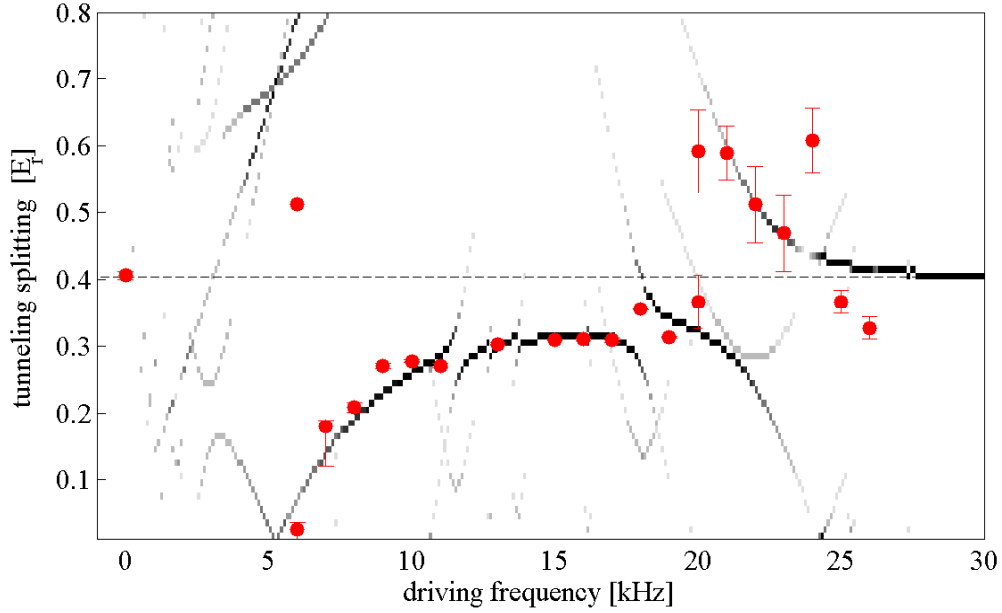


Figure 3.13: Dependence of the tunneling dynamics on the driving frequency. The measured data (red dots) show a good agreement with the theoretical prediction of the Floquet theory (gray shading).

3.4.1 Frequency dependence

The driving frequency can be changed easily over a wide range in the experiment. For a symmetrically realized double well with the potentials $V_1 = 6.25\mathcal{E}_r$ and $V_2 = 5.40\mathcal{E}_r$ and for a driving amplitude $S = 7353\mathcal{E}_r$, which complies to a lift of $0.93\mathcal{E}_r$ of each well out of equilibrium the results are compared with the theoretical prediction of the Floquet state analysis in fig. 3.13. The red dots represent the sinusoidal fits to the measured data and the Floquet-state solution is depicted by the gray shading, which is proportional to the overlap of the Floquet state with the ground state doublet, i.e., the initially prepared state.

The data points were obtained by sinusoidally fitting the measured diffraction efficiencies, at which the limited observation time made it difficult to obtain frequencies for very slow tunneling, where not even one full cycle could be tracked. This was compensated for by identifying the starting point of the tunneling dynamics, i.e., the end of the preparation face, as accurate as possible. Moreover the amplitude can be estimated and an upper limit was included to the fits. For faster tunneling periodicities it was also possible to verify the results of the sinusoidal fits by comparing them to the findings of a Fourier analysis of the data.

Not only a very good agreement of the measured data with the theoretical prediction can be observed in fig. 3.13, there is also an evidence for the realization of CDT for a driving frequency of $\omega_d = 6\text{kHz}$, where no tunneling at all was observed

during the duration of the experiment, as it is predicted theoretically.

3.4.2 Breaking symmetry of the driving

The symmetry dependence of the effect of CDT discussed in sec. 2.3.2 is as stunning as the effect itself. The art is to find the right values for amplitude and frequency, then a sinusoidal driving added to a quantum system is capable of stopping its inherent dynamics. On the other hand, if the shape of the driving does not match the generalized parity symmetry the driving force has hardly any effect on the systems dynamics.

This sensitivity to the symmetry of the driving shall be utilized to verify that it is the effect of CDT that was observed and presented in the section before. Hence the generalized parity symmetry P of the driving was broken and it could be observed that the driving with broken symmetry does not at all yield a suppression of the atoms tunneling.

One variation of breaking the generalized parity P is breaking the symmetry in time. Therefore instead of the sinusoidal time dependence of the driving a sawtooth like time dependence was realized, which is still periodic in time with period T_d , but not invariant under the translation $x \rightarrow -x$, $t \rightarrow t + \frac{T_d}{2}$. This is the easiest way to break the parity symmetry experimentally, as it is a knob at the function generator realizing the frequency variation of the AOD frequency.

The experimental results are presented in fig. 3.14, in which the diffraction efficiencies are plotted over time and the gray shaded area indicates the preparation process. In (a) the unperturbed tunneling (open circles) is compared to the realization of CDT (black dots). The black lines correspond to the sinusoidal fits to the data. Fig. 3.14(b) shows the result for the same driving frequency where CDT occurred only with a sawtooth shaped driving, i.e., with a generalized symmetry broken in time. Clearly the dynamics of the atoms is not suppressed but they are tunneling between the wells. As expected the periodicity of the tunneling is slightly slower than for the unperturbed potential.

Another possibility to break the generalized symmetry is to break the spatial symmetry. Experimentally this can be done by driving symmetrically, i.e., sinusoidally, an asymmetric double well potential. This is equivalent to driving a symmetric double well with $f(t) = \sin(\omega_d t) + d_{\text{offset}} \cdot \tilde{x}$ with \tilde{x} being the distance to the symmetry point of each double well. With this the system's Hamiltonian is not invariant under the translation $x \rightarrow -x$, $t \rightarrow t + \frac{T_d}{2}$. The experimental results for this, i.e., an asymmetric double well driven symmetrically with the frequency where CDT occurred, are shown in fig. 3.14(c). Again the tunneling dynamics is not at all suppressed, but only slightly slowed compared to the undriven tunneling rate.

3.4.3 Amplitude dependence

In contrast to the freedom in choosing the frequency of the driving the experimental setup allows only small driving amplitudes. Nevertheless it is also possible to vary

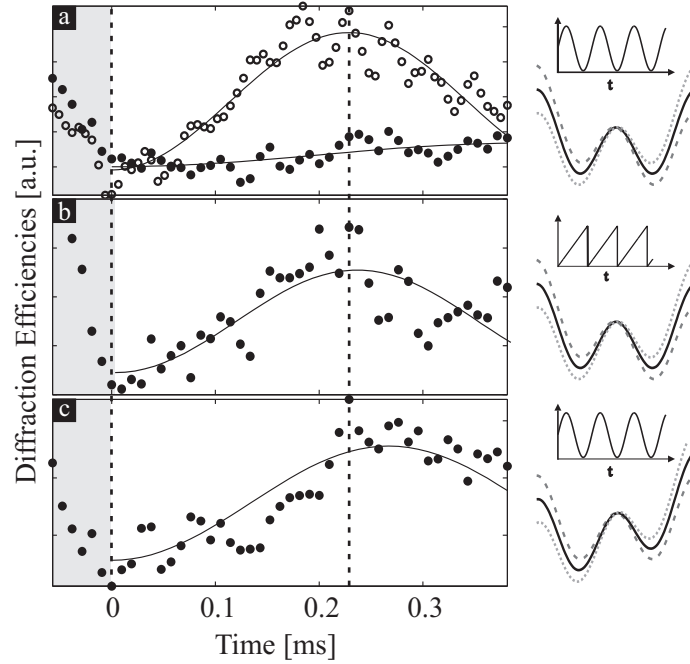


Figure 3.14: Breaking the symmetry of the driving in time and space. (a) The realization of CDT (black dots) is compared to the tunneling dynamics of an atom in a static double well potential (circles). The gray shaded area indicates the preparation phase and the black lines are sinusoidal fits to the data. (b) Breaking the generalized parity symmetry P in time by sawtooth shaped driving destroys the effect of CDT. (c) Breaking the spatial symmetry, here done by symmetrically driving an asymmetric double well, has the same effect of destroying CDT. In both cases the tunneling dynamics is slightly slower than in the undriven double well, as predicted by theory.

the driving amplitude at least to some extent for fixed driving frequency and to compare this to the predictions from the theory as an additional proof of the good controllability of atomic dynamics in the realized setup. Since the amplitude is realized by changing the angle of incidence of the potential V_2 the amount the two wells of one unit cell are shifted against each other depends on their distance from the mirror. For small deviations from the initial angle $\alpha = \pi/3$, the difference between the driving amplitudes of neighbored double wells is not considerable. The experimental results comply with the numerical simulations that verify that for small amplitudes the effect of the driving as realized here does not deviate from a driving force without an amplitude that depends on the position. For bigger variations of the angle of incidence those amplitude differences between neighboring wells become relevant. The atoms see significantly different driving amplitudes as they are spread over some 20 distinct double wells.

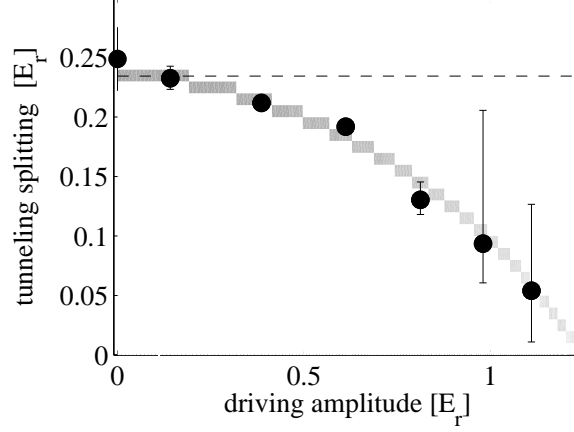


Figure 3.15: Dependence of the tunneling dynamics onto the driving amplitude for fixed driving frequency. The gray shading corresponds to the Floquet state prediction, the red dots represent the sinusoidal fits to the measured data and the dashed line indicates the tunneling splitting for the unperturbed double well.

For a reasonable range of amplitudes the dependence of the tunneling time on the driving amplitudes is shown in fig. 3.15. Again the data points (red dots) represent the sinusoidal fits to the measured data and the gray shading depicts the theoretical prediction of the Floquet-state method for potentials $V_1 = 8.27\mathcal{E}_r$ and $V_2 = 2.68\mathcal{E}_r$, as measured beforehand. Thereto the double wells were not perfectly symmetric, the asymmetry could be determined to $\delta_\alpha = 44.6\mu\text{rad}$, corresponding to an increase/decrease of $0.11\mathcal{E}_r$ of the minimum of the well right and left well respectively and is included to the Floquet analysis. The driving frequency was chosen to be $\omega_d = 6\text{kHz}$.

The two-mode approximation is not included to the figure, as it does not show any deviations from the full Floquet analysis in this range of small amplitudes that can be realized with the experimental setup.

Chapter 4

Non-spreading wave packets in imaginary potentials

A quantum mechanical phenomenon as fundamental as tunneling is the dispersion of a wavepacket. In contrast to light, matter wave packets do even spread in vacuum due to the form of the linear Schrödinger equation. But it was also Schrödinger himself, who pointed out, that it should be possible to create a non-spreading wave packet out of the eigenstates of a harmonic oscillator [51]. Those wave packets periodically recapture their original form, which was experimentally realized for Rydberg atoms by J. Yeazell et al. [52]. At that time it was the attempt to explain the transition from the microscopic world to the macroscopic one, namely to show that point-like particles could be described by wave packets. Today the context changed from the pure effort to understand the quantum mechanical theory and to prove it to the attempt to use it or control it. This ability to control the shape, as well as the motion of quantum states may lead to methods for bond-selective chemistry and novel quantum technologies, such as quantum computing [53, 17].

A theoretical work of Fedorov et al. [54] suggests the use of an imaginary potential to sculpture a wave packet, namely to create a non-spreading wave packet of gaussian shape, a quite amazing occurrence as the imaginary potential [28] does not actually exert a classical force. The effect relies on the absorption due to the imaginary potential compensating for the dispersion, i.e., the broadening due to dispersion of the wave packet competes against the diminishment of the wave packet width as a result of absorption. After a characteristic time t_0 those two processes balance resulting in a stationary, i.e., non-spreading, wave packet. Symptomatic features of this stationary solution are a complex Gaussian shape and a quadratic phase.

Such a non-spreading wave packet could be realized for the first time as presented in [55] added on the following pages. A detailed description of the setup and of the experiment can also be found in the works of Martin Göbel [26] and Ralf Stützle [25].

Observation of Nonspreading Wave Packets in an Imaginary Potential

R. Stützle,* M. C. Göbel, Th. Hörner, E. Kierig, I. Mourachko, and M. K. Oberthaler

Kirchhoff-Institut für Physik, Universität Heidelberg, Im Neuenheimer Feld 227, D-69120 Heidelberg, Germany[†]

M. A. Efremov,¹ M. V. Fedorov,¹ V. P. Yakovlev,² K. A. H. van Leeuwen,³ and W. P. Schleich⁴

¹*General Physics Institute, Russian Academy of Sciences, 38 Vavilov Street, Moscow, 119991 Russia*

²*Moscow Engineering Physics Institute (State University), 31 Kashirskoe shosse, Moscow, 115409 Russia*

³*Eindhoven University of Technology, P.O. Box 513, 5600 MB Eindhoven, The Netherlands*

⁴*Abteilung für Quantenphysik, Universität Ulm, D-89069 Ulm, Germany*

(Received 15 December 2004; published 8 September 2005)

We propose and experimentally demonstrate a method to prepare a nonspreading atomic wave packet. Our technique relies on a spatially modulated absorption constantly chiseling away from an initially broad de Broglie wave. The resulting contraction is balanced by dispersion due to Heisenberg's uncertainty principle. This quantum evolution results in the formation of a nonspreading wave packet of Gaussian form with a spatially quadratic phase. Experimentally, we confirm these predictions by observing the evolution of the momentum distribution. Moreover, by employing interferometric techniques, we measure the predicted quadratic phase across the wave packet. Nonspreading wave packets of this kind also exist in two space dimensions and we can control their amplitude and phase using optical elements.

DOI: 10.1103/PhysRevLett.95.110405

PACS numbers: 03.75.Be, 03.75.Dg, 42.50.Vk

Nonspreading wave packets have attracted interest since the early days of quantum mechanics. Already in 1926 Schrödinger [1] found that the displaced Gaussian ground state of a harmonic oscillator experiences conformal evolution because a classical force prevents the wave packet from spreading. Even in free space the correlations between position and momentum stored in an initially Airy-function-shaped wave packet can prevent spreading [2]. Here we propose and experimentally observe the formation and propagation of nondispersive atomic wave packets in an imaginary (absorptive) potential accessible in atom optics [3–5]. Although there is no classical force, there are correlations continuously imposed by Heisenberg's uncertainty relation resulting in the stabilization of the wave packet.

Localized wave packets due to stabilization are well known in the context of periodically driven quantum systems [6] and studied with increasing interest for electronic wave packets in Rydberg atoms [7–10]. Our approach to create nondispersive atomic wave packets relies on three ingredients: (i) an absorption process [11] cuts away the unwanted parts of a broad wave creating a packet that is continuously contracting in position space, (ii) this process leads due to Heisenberg's uncertainty relation to a broadening in momentum space and consequently to a faster spreading in real space, and (iii) the absorptive narrowing and the quantum spreading are balanced, leading to a nonspreading wave packet. In the following we will refer to such a wave packet as a Michelangelo packet [12].

Complex potentials for matter waves [13] emerge from the interaction of near resonant light with an open two-level system shown in Fig. 1(a). For a standing light wave tuned *exactly* on resonance an array of purely imaginary harmonic potentials arises. When the Rabi frequency Ω_0 is

of the order of the excited state linewidth Γ the local saturation parameter $|\Omega_0 \sin(kx)/\Gamma|$, and thus the upper level population, is of the order of unity except in a small vicinity of the field nodes. Consequently, our system de-

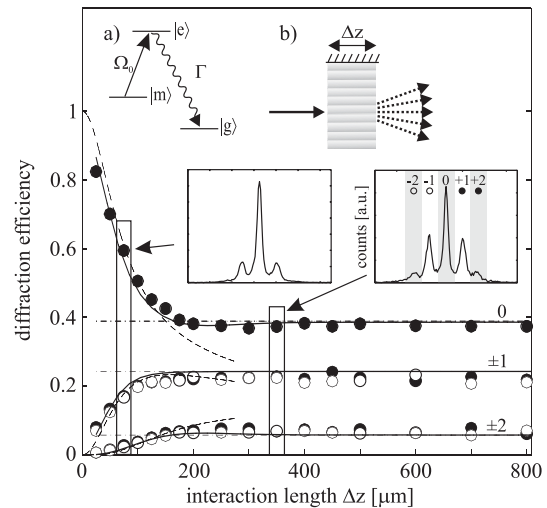


FIG. 1. Formation of a nonspreading Michelangelo wave packet for the center-of-mass motion of an open two-level atom (a). The resonant interaction with a standing light wave (b) leads to an array of harmonic imaginary potentials. The normalized diffraction efficiencies derived from the momentum distributions (inset) approach a steady state as a function of the interaction length Δz demonstrating the successful realization of stationary wave packets. The solid curves result from a numerical integration of the Schrödinger equation [17] with the Rabi frequency $\Omega_0 = 0.4\Gamma$. The dashed lines correspond to the Raman-Nath approximation, revealing that the interplay between absorption and quantum spreading is essential for obtaining a steady state.

cays approximately with the rate Γ . Therefore, in the time domain $t \gg 1/\Gamma$ the atomic wave function vanishes almost everywhere, except in the small vicinity δx of the field nodes. Here the saturation is small and our open system decays with the rate $(\Omega_0 k \delta x)^2 / \Gamma \ll \Gamma$. We estimate the time dependent size δx from the relation $(\Omega_0 k \delta x)^2 t / \Gamma \sim 1$ and find $\delta x(t) \sim (\Gamma/t)^{1/2} / (k\Omega_0)$.

The decrease of $\delta x(t)$ is accompanied by an increase of the width $\delta p(t) \sim 1/\delta x(t)$ in momentum space [14] leading to spatial spreading of the wave packet. Because of competition of the two processes—absorptive contraction and quantum spreading—the width $\delta x(t)$ reaches its minimal stationary value δx_0 . In this asymptotic regime the rate $\delta x(t)/t$ of absorptive contraction is obviously balanced by the rate $\delta p(t)/M$ of quantum spreading which yields the characteristic time $t_0 \equiv 1/\omega_0 \sim \Omega_0^{-1}(\Gamma/\omega_r)^{1/2}$ and the stationary width $\delta x_0 \sim (M\omega_0)^{-1/2}$ with the recoil frequency $\omega_r \equiv k^2/(2M) \ll \Gamma$.

The experiments are performed with a slow atomic beam of metastable argon ($v = 50$ m/s) produced with a standard Zeeman slower. The brilliance of the beam is significantly enhanced with a 2D-MOT setup [15]. The final collimation necessary for coherent illumination is obtained by two slits ($25 \mu\text{m}$ and $10 \mu\text{m}$) within a distance of 25 cm. Applying a Stern-Gerlach magnetic field we select the atoms in the internal state $1s_5$ ($J = 2$, $m_j = 0$). The imaginary potential is realized with a circularly polarized standing light wave by retroreflecting a laser beam resonant with the $1s_5-2p_8$ transition (801 nm). This setup realizes to a very good approximation an open two-level system since only 16% of the excited atoms fall back to the initial state (in contrast to 32% without magnetic state selection). In order to control the interaction length Δz , the laser beam passes an adjustable slit. By imaging the slit onto the retroreflecting mirror we avoid the spoiling effect of light diffraction. The detection of the metastable argon atoms is achieved by a microchannel plate detector allowing for spatially resolved single atom detection utilizing their internal energy (12 eV). Since the transverse coherence length of the incoming atomic beam is much larger than the optical wave length, the outgoing wave function is a coherent array of single Michelangelo wave packets, resulting in constructive interference in certain directions. The spatial resolution $\sim 50 \mu\text{m}$ of our atomic detector and the free flight distance ~ 0.5 m guarantee clearly resolving the resulting atomic diffraction pattern in the far field.

The diffraction efficiency is deduced by summing up the detected number of atoms in angular windows as indicated in the right inset of Fig. 1. After their initial dynamics the wave packets, i.e., the diffraction efficiencies do not change giving evidence to the formation of Michelangelo wave packets [16]. Our numerical simulations (solid line) of the open two-level Schrödinger equation take into account the longitudinal as well as the transverse velocity distributions $\Delta v_l = 10$ m/s and $\Delta v_t = 7$ mm/s of the

experiment. For $\Omega_0 = 0.4\Gamma$ we have a very good agreement with our experimental findings. Since this agreement depends critically on the Rabi frequency we can determine its absolute value. It is consistent within a factor of 2 both with a rough estimate, using the power measurement of the incoming light beam, and with the overall absorption of the atomic beam.

In order to stress that the interplay between absorptive narrowing and the quantum spreading is crucial for the formation of the Michelangelo packet, we have included the result of the Raman-Nath approximation (dashed lines). Since this approach is only valid as long as quantum spreading is negligible, it fails to predict the resulting dynamics after the characteristic time t_0 .

According to the arguments given above, Michelangelo wave packets emerge after a characteristic time $t_0 \sim 1/\Omega_0$. Our experimental results shown in Fig. 2 confirm the expected scaling with $\Omega_{\min} = 0.23\Gamma$.

We now show that a Michelangelo wave packet is a complex Gaussian wave packet with a quadratic phase. For this purpose we recall [17] that the solution of the Schrödinger equation

$$i \frac{\partial}{\partial t} \varphi(x, t) = \left(-\frac{1}{2M} \frac{\partial^2}{\partial x^2} - iU_2(x) \right) \varphi(x, t) \quad (1)$$

for the metastable state wave function $\varphi(x, t)$ in the vicinity of $x = 0$, where $U_2(x) = M\omega_0^2 x^2/2$ with $\omega_0 \equiv \Omega_0 \sqrt{2\omega_r/\Gamma}$ reads [5]

$$\varphi(x, t) = \sqrt{\frac{k/\pi}{\cosh \beta t}} \exp\left(-\frac{1}{2} \alpha x^2 \tanh \beta t\right), \quad (2)$$

with $\alpha \equiv M\omega_0 \exp(-i\pi/4)$ and $\beta \equiv \omega_0 \exp(i\pi/4)$.

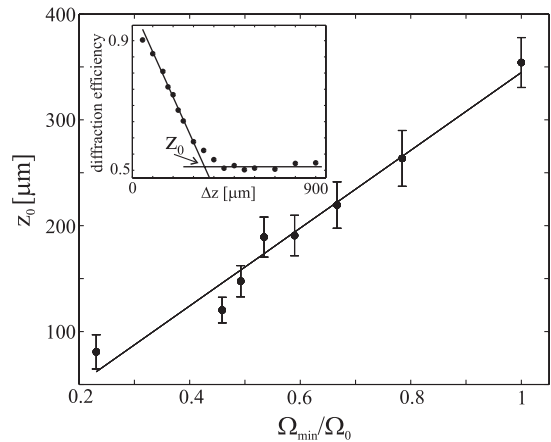


FIG. 2. Experimental verification of the scaling law $t_0 \sim 1/\Omega_0$ connecting the characteristic time $t_0 \equiv z_0/v$ when Michelangelo wave packets form and the Rabi frequency Ω_0 . The line is a guide to the eye. We measure the zeroth order diffraction efficiency as a function of Δz (inset) for different Rabi frequencies. The crossing point between the linear extrapolation of the short and long-time limits yields z_0 .

Hence, the probability density $|\varphi(x, t)|^2$ is a Gaussian with the time dependent width $\delta x(t) \equiv [\text{Re}\{\alpha \tanh(\beta t)\}]^{-1/2}$, which for $\omega_0 t > 1$ reaches its minimal stationary value $k\delta x_0 \equiv (\omega_r \Gamma / \Omega_0^2)^{1/4}$.

In this asymptotic regime Eq. (2) factorizes into a product of the time dependent function $\cosh^{-1/2}(\beta t)$, showing that the Michelangelo probability density decays exponentially in time with the rate $\Gamma_0 \equiv \omega_0 / \sqrt{2} \ll \Gamma$, and the position dependent complex Gaussian $\exp(-\alpha x^2/2)$ which contains the quadratic phase $\phi(x) \equiv M\omega_0 x^2 / \sqrt{8}$. A Fourier transformation of this wave packet with the stationary width δx_0 , yields the asymptotic behavior of the diffraction efficiencies shown in Fig. 1 by the dashed-dotted lines and is in perfect agreement with our experimental findings.

The predicted phase $\phi(x)$ of the Michelangelo packet can be deduced from the phases of the observed diffraction orders where the phase of the n th order with respect to the zeroth order is $\phi(n) = -2(\omega_r \Gamma / \Omega_0^2)^{1/2} n^2 \equiv \phi_2 n^2$. To measure the relative phases we realize a compact interferometer setup shown in Fig. 3(a). A thin near-resonant probing standing light wave (waist 30 μm) is placed di-

rectly behind the array of harmonic imaginary potentials. The wave function amplitude in each output direction is given as a superposition of different diffraction orders of the Michelangelo packet. By changing the relative phase between the two standing light waves we can measure an interference pattern and thus deduce the phase evolution as a function of the interaction length Δz .

The interferometric setup employs a probing standing wave at 801 nm realized by beams impinging on the mirror under an angle of 10° . Thus, moving the mirror allows us to scan the relative phase ϕ_s between the probing and the absorptive light wave (beating period 25 μm). The presence of a magnetic field in the interaction region enables us to realize a detuned (8 MHz) probing wave using the same laser for both standing light waves but different circular polarizations. By detuning the probing light wave the total flux through the interferometric setup is significantly increased in comparison to an exactly resonant probing field.

In order to deduce the absolute value of ϕ_2 we evaluate the interferometer output in the direction of the *third* diffraction order. For our experimental parameters this beam is always a *two-beam* interference of the first and second diffraction order of the array of Michelangelo packets. In contrast, the output in lower diffraction order directions is the result of *multiple-beam* interference and does not allow us easily to deduce the involved phases.

In order to find the phase difference $\phi(2) - \phi(1)$ we have to eliminate the offset phase arising mainly from the fact that the probing light field is not infinitely thin. For this purpose we take the difference between the measured phase in the long-time limit of the absorptive wave ($\Delta z > 400 \mu\text{m}$) and the phase for the experimentally achievable shortest interaction length (50 μm). For the Rabi frequency $\Omega_0 = (0.23 \pm 0.02)\Gamma$ we find the experimental value $|\phi(2) - \phi(1)| = 1.70 \pm 0.17$, which is in agreement with the prediction of the numerical integration $\phi(2) - \phi(1) = 3\phi_2$, that is $|\phi_2| = 0.57 \pm 0.1$. Moreover, the characteristic length $z_0 \sim 400 \mu\text{m}$ for leveling off the phases coincides with the one for leveling off the diffraction efficiencies. Furthermore, by increasing the Rabi frequency to $\Omega_0 = (0.4 \pm 0.05)\Gamma$ we experimentally deduce $|\phi_2| = 0.32 \pm 0.08$, which is in very good agreement with the prediction of the numerical integration $|\phi_2| = 0.27 \pm 0.04$.

So far we have concentrated on wave packets in $D = 1$ spatial dimensions. A straightforward generalization to $D = 2$ relies on two orthogonal linear polarized standing waves interacting with the appropriate atomic transitions and leads to the potential $-iM(\omega_x^2 x^2 + \omega_y^2 y^2)/2$ near the nodes. The frequencies ω_x and ω_y depend on the field intensities. A nonorthogonal configuration provides even additional parameters to control the form of the emerging two-dimensional Michelangelo wave packet.

We emphasize that Michelangelo wave packets are not restricted to the Gaussian form, Eq. (2), originating from the quadratic potential U_2 in Eq. (1). Indeed, with an

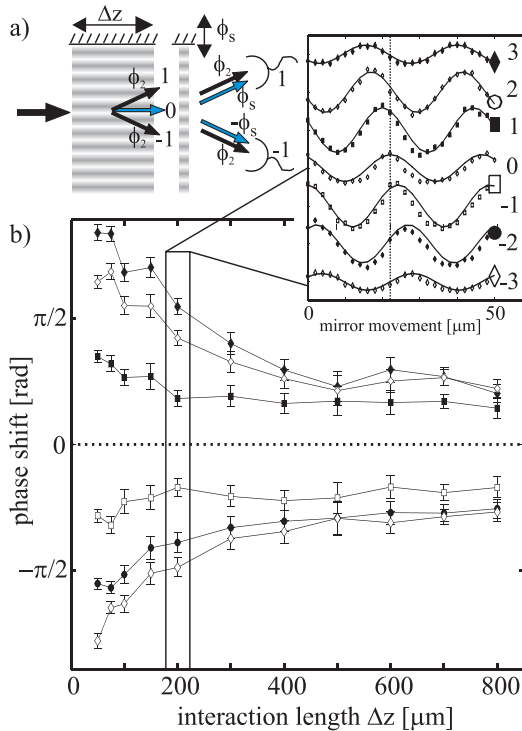


FIG. 3 (color online). Measurement of the phase of a Michelangelo wave packet using an interferometric setup (a) consisting of the absorptive and probing standing waves. The inset in (b) shows typical interference patterns for different output directions obtained by scanning the relative position of the second (thin) standing light wave for a given interaction length Δz . For large values of Δz the phase shifts (b) of the different interferometer outputs relative to the zeroth order level off, indicating stationary phases of the wave packet.

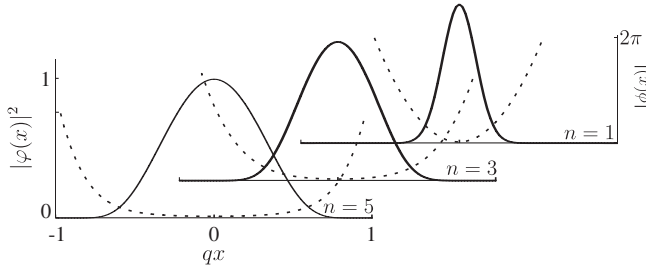


FIG. 4. Probability density $|\varphi(x)|^2$ (solid line) and absolute value of phase $|\phi(x)|$ (dotted line) of Michelangelo wave packets in the potential U_{2n} .

appropriate mask [18] we can create almost any behavior of the mode function close to the node, leading, for example, to a power law potential $U_{2n}(x) = (\Omega_0^2/\Gamma)(qx)^{2n}$. Here $q \ll k$ determines the characteristic width of U_{2n} .

The Michelangelo wave packets shown in Fig. 4 for $n = 1, 3$, and 5 are the “ground” state eigenfunctions of the corresponding stationary non-Hermitian Hamiltonians and can be obtained numerically. In the asymptotic regime only these functions survive because their complex energy “eigenvalues” have the smallest imaginary parts. Moreover, applying the general arguments above to the case of U_{2n} yields the following characteristic time and width:

$$t_0 \sim \frac{1}{\Omega_0^{2/(n+1)}} \left(\frac{\Gamma}{\tilde{\omega}_r^n} \right)^{1/(n+1)} \quad \text{and} \quad q\delta x_0 \sim \left(\frac{\Gamma}{\Omega_0^2 t_0} \right)^{1/2n}, \quad (3)$$

where $\tilde{\omega}_r = q^2/(2M)$. These scaling behaviors have been confirmed by numerical integration of the corresponding Schrödinger equation. We note that for $n = 1$ these expressions reduce to the ones of the previous case. For $n \rightarrow \infty$ the potential U_{2n} takes on the shape of a box, t_0 is independent of Ω_0 , and δx_0 is solely given by q .

In conclusion we present a new class of nonspreading wave packets resulting from the interplay between absorptive narrowing and quantum spreading. The developed theoretical description explains the experimental observation of both the phase and the amplitude of the wave packet quantitatively. The experimental realization of imaginary potentials strongly relies on spontaneous decay processes. Nevertheless, we show that coherence is maintained and can even be employed for deducing the phase of the Michelangelo packets. Since the wave packet arising in the long-time limit is weakly dependent on the initial wave function, this process is a robust tool for generating wave packets with well-defined amplitude and phase for further experiments.

We acknowledge fruitful discussions with A. Buchleitner and thank M. Störzer for his commitment in the early stage of the experiment which was funded by Optik-Zentrum Konstanz, Center for Junior Research Fellows in Konstanz, by Deutsche Forschungsgemeinschaft (Emmy Noether Program), and by the European

Union, Contract No. HPRN-CT-2000-00125. MVF, WPS, and VPY also thank the Alexander von Humboldt-Stiftung for its generous support during the course of this project, especially for the Humboldt-Kolleg at Cuernavaca, Mexico. This work was partially supported by the Landesstiftung Baden-Württemberg and the Russian Foundation for Basic Research (Grant Nos. 02-02-16400, 03-02-06145, 04-02-16734).

*Electronic address: stuetzle@kip.uni-heidelberg.de

†Electronic address: www.kip.uni-heidelberg.de/matterwaveoptics

- [1] E. Schrödinger, *Naturwissenschaften* **14**, 664 (1926).
- [2] M. V. Berry and N. L. Balazs, *Am. J. Phys.* **47**, 264 (1979).
- [3] D. O. Chudesnikov and V. P. Yakovlev, *Laser Phys.* **1**, 110 (1991).
- [4] M. K. Oberthaler *et al.*, *Phys. Rev. Lett.* **77**, 4980 (1996).
- [5] M. V. Berry and D. H. J. O’Dell, *J. Phys. A* **31**, 2093 (1998).
- [6] A. Buchleitner, D. Delande, and J. Zakrzewski, *Phys. Rep.* **368**, 409 (2002), and references therein.
- [7] G. P. Berman and G. M. Zaslavsky, *Phys. Lett. A* **61**, 295 (1977); K. Richter and D. Wintgen, *Phys. Rev. Lett.* **65**, 1965 (1990); J. Henkel and M. Holthaus, *Phys. Rev. A* **45**, 1978 (1992); D. Delande and A. Buchleitner, *Adv. At. Mol. Opt. Phys.* **35**, 85 (1994); I. Bialynicki-Birula, M. Kalinski, and J. H. Eberly, *Phys. Rev. Lett.* **73**, 1777 (1994); A. Buchleitner and D. Delande, *Phys. Rev. Lett.* **75**, 1487 (1995); M. V. Fedorov and S. M. Fedorov, *Opt. Express* **3**, 271 (1998); M. Kalinski *et al.*, *Phys. Rev. A* **67**, 032503 (2003).
- [8] H. Maeda and T. F. Gallagher, *Phys. Rev. Lett.* **92**, 133004 (2004).
- [9] L. G. Hanson and P. Lambropoulos, *Phys. Rev. Lett.* **74**, 5009 (1995).
- [10] X. Chen and J. A. Yeazell, *Phys. Rev. Lett.* **81**, 5772 (1998).
- [11] Absorption also plays a crucial role in the proposal [9] for and in the experiment [10] with an electronic nonspreading wave packet in a two-electron atom using atomic mode locking by loss modulation.
- [12] For Michelangelo, sculpturing means “releasing the desired form from a block of marble by cutting away unwanted materials”. See, for example, D. Preble, *Artforms* (Harper & Row, New York, 1978).
- [13] K. S. Johnson *et al.*, *Science* **280**, 1583 (1998); M. K. Oberthaler *et al.*, *Phys. Rev. A* **60**, 456 (1999); A. Turlapov *et al.*, *Phys. Rev. A* **68**, 023408 (2003).
- [14] Throughout the Letter we use $\hbar \equiv 1$.
- [15] A. Scholz *et al.*, *Opt. Commun.* **111**, 155 (1994).
- [16] This conclusion is only valid since our interferometric experiment discussed below exclude additional dynamics of the relative phases between diffraction orders.
- [17] M. A. Efremov *et al.*, *Laser Phys.* **13**, 995 (2003); M. V. Fedorov *et al.*, *JETP* **97**, 522 (2003).
- [18] U. Drodofsky *et al.*, *Appl. Phys. B* **65**, 755 (1997); M. Mützel *et al.*, *Phys. Rev. Lett.* **88**, 083601 (2002).

Chapter 5

Conclusion

The present work gives a summary of experiments concerning the control of quantum states. After concluding the study of the interaction of matter waves with imaginary potentials and the first experimental realization of non-spreading wave packets, i.e., the active control of the shape of a wave packet, an experimental setup was created to coherently control the tunneling dynamics of particles in a conservative double-well potential. A direct visualization of the tunneling of massive particles could be presented, as well as the realization of a control of this dynamics via an ac-driving field. Furthermore the effect of coherent destruction of tunneling (CDT) was observed and its critical dependence on the generalized parity symmetry of the driving field demonstrated.

Together with Ralf Sützle, Martin Göbel and Thomas Hörner the final measurements of a non-spreading wave packet could be realized, which was summarized in chapter 4. Those wave packets arise in the long-time limit of the interaction of an atom with an imaginary potential. The stationary solution appears due to two competing processes, the absorptive narrowing and the spreading due to dispersion, balancing after a certain time t_0 . For not only measuring the width of the wave packet and its leveling, but the whole wave function, the corresponding phase was determined in addition. These results also published in [55] do not only present the first experimentally realized non-spreading wave packet of Gaussian shape due to an imaginary potential, but also point out that the wave form depends primarily onto the chosen complex potential, making the method a viable instrument to generate wave packets with well-defined shape and phase, which can be chosen almost arbitrarily.

The starting point for the study of strong driving was a paper by Grossmann et al. [20] where they study the influence of a sinusoidal driving force onto the tunneling dynamics of a particle in a quartic double well potential. They predict an effect, naming it coherent destruction of tunneling, which implies that there exist parameter combinations of driving frequency and amplitude leading to a complete standstill of the tunneling dynamics. This is a quite astonishing result as the occurrence of tunneling is an intrinsic property of the quantum nature of the particles.

The experiments were done utilizing a slow and coherent beam of metastable argon atoms. For creating the double well potential a unit of two mirrors with an angle of $\xi = (2.0903 \pm 7 \cdot 10^{-7})\text{rad}$ was installed that reunites two beams under an angle of exactly $\pi/3$, which were diffracted by an acousto optical deflector beforehand. Close to the mirror, where all beams overlap the resulting light shift potential has the form of a continuous row of double wells, if red detuned light is used. The driving field then is realized by varying this angle between the two standing light waves. The atoms are diffracted by this periodic arrangement of equally formed double wells enabling the direct observation of the dynamic of the atoms in momentum space. Potential and driving field are not exactly what was proposed by Grossmann et al., but it could be proven by calculations beforehand that the deviations from the model system would not destroy the effect of CDT. Therefor a detailed theoretical analysis of the experimentally realized system was made using the Floquet theory as elaborated by Hänggi [19] as well as the split-step Fourier method enabling a full numerical solutions.

One of the main issues of this work was the realization of a stable double well potential, which was achieved allowing the direct observation of single particle tunneling. With this it was possible to demonstrate an experimental realization of ac-control of this tunneling dynamics and to study the symmetry dependence of the system.

The measured data are in excellent quantitative agreement with the predictions from the Floquet analysis as well as the finding of the split-step Fourier method. Both the dependence of the tunneling on the driving amplitude and the driving frequency was studied, whereat the chosen experimental implementation of the driving field enables a wide range of realizable driving frequencies, but limits the choice of the driving amplitudes. Only small amplitudes lead to reasonable results. For bigger amplitudes not all those double wells coherently illuminated by the atomic beam do experience the same lift of their wells as the amplitude depends on the distance from the mirror.

Varying the driving frequency the full control of the tunneling dynamics of the atoms could be demonstrated and even the complete suppression, i.e., CDT, was observed. The appearance of this effect was verified by studying its critical dependence on the generalized parity symmetry. As predicted only if the driving field suffices this symmetry condition the effect occurs, otherwise only a slight slowing of the tunneling process can be observed. Altogether the experiments illustrate the capacity of an external driving force for controlling quantum systems. These results are also published in [56].

The realization of a periodic double well potential, as reported here, with perfectly controllable parameters such as the symmetry of the unit cell as well as the driving makes it a general model system for studying strongly driven systems in the quantum regime. It clearly has the potency to prepare complex quantum states in many particle systems. For example it exists theoretical work proposing the usage of such an ac-driving to induce the transition from a superfluid to a Mott insulator [57], which would be an altogether different manner to drive this transition aiming

at obtaining genuinely new, nontrivial information on condensate dynamics.

The presented system should also be extendable to the regime of chaotic motion present in hamiltonian ratchets [58, 59], which could provide interesting insights into the relation between classical chaos and quantum mechanics.

Furthermore there exist a variety of suggestions towards coherence stabilization of qubits relying on the influence of external fields. This addresses one of the main challenges on the way to a working quantum computer, namely the unavoidable coupling to the environment. As proposed by Fonseca-Romero et al.[18] it should be possible to prevent the decoherence of a gate utilizing an ac-field. This is due to the effect of CDT, which is capable of shifting the coherent long-time dynamics the qubit towards lower frequencies where the spectral density of the considered ohmic bath is lower and, thus, the effective coupling is weaker.

During the last years quantum control has attracted enormous theoretical and experimental interest. Altogether one can expect further exciting results presenting tools to handle the quantum world, which reveal new insights or bring us even closer to a working quantum computer.

Appendix A

Creating a coherent beam of slow atoms



Figure A.1: Photo of the beam machine. On the left the nitrogen cooling of the atomic source can be seen, followed by a chamber containing the first collimation stage and the long arm with the Zeeman slower coils. The big vacuum chamber on the right contains the funnel and the first slit, followed by the chamber for the experimental setup and the long arm at which's end the detector is installed.

The experiments were realized with a coherent beam of slow argon atoms. Besides the coherence it was of great interest to slow the atoms down as far as possible while maximizing the flux.

Vacuum

To realize an experiment with single atoms the residual gas has to be minimized to avoid collisions, i.e., influences other than those experimentally studied. The vacuum aperture used here is split into two parts concerning the quality of the vacuum. In

the first two chambers of the apparatus the vacuum is with about 10^{-5} mbar and 10^{-6} mbar respectively a high vacuum (HV) produced by oil diffusion pumps each combined with one rotary vane pump as booster pump. This enable to evacuate big volumes in short time, so that the vacuum can be restored in a reasonable time (less than a day), which is necessary as this part has to be opened frequently to renew the wires functioning as cathode for the gas discharge (described in the following section). By a gate valve this part can be separated from the following, so that the vacuum in the rest of the apparatus is not affected. After a differential pumping stage the ultra high vacuum part of the apparatus follows. A pressure of about 10^{-8} mbar is achieved by two turbo-molecular pumps in combination with a turbodrag pump and two rotary vane pumps as booster pumps. (Later on the turbodrag pump was removed as it had no essential effect.)

Source of metastable argon atoms

A photo of the argon beam apparatus is shown in fig. A.1. On the left hand side one can see the nitrogen cooling of the atom source. It is a high voltage gas discharge producing slightly cooled metastable argon atoms (about 300m/s). The design of source follows a concept originally proposed for neon by Kawanaka et al.[60]. Four welding wires inside a glass tube function as cathode, a metal dist at the end of the source body as an anode. In the gas discharge primarily argon ions and free electrons are produced. The electrons then are accelerated to a second anode following in a distance, kept variable for optimization. The metastable argon atoms are generated from collisions of those electrons with the residual gas, which transfers the atoms into an excited state from which they relax into the metastable states $1s_3$ and $1s_5$. The cooling only works for the wanted $1s_5$ state, however also atoms in the $1s_3$ state will move into the direction of the beam. The selection of the state $1s_5$ happens later on in the funnel unit. The second anode also functions as differential pumping stage towards the next vacuum chamber.

Collimation

Metastable atoms that pass this pumping stage all have a preferential direction, the direction of propagation of the atomic beam, but this beam still is very divergent. Hence a first 2D-collimation stage is integrated increasing the flux of atoms through the next differential pumping stage by a factor of about 100. It is cooled by spontaneous emission sweeping the share of the wave vector of the cooling light, that is perpendicular to the atomic beam, synchronously with the decrease of the perpendicular velocity of the atoms. This is implemented as proposed by Shimizu et al.[61] by reflecting a blue detuned light beam repeatedly by two facing mirrors, that are slightly tilted towards each other as sketched in fig. A.2. Because of the tilde the direction of the wave vector is changed with each reflection realizing the sweep.

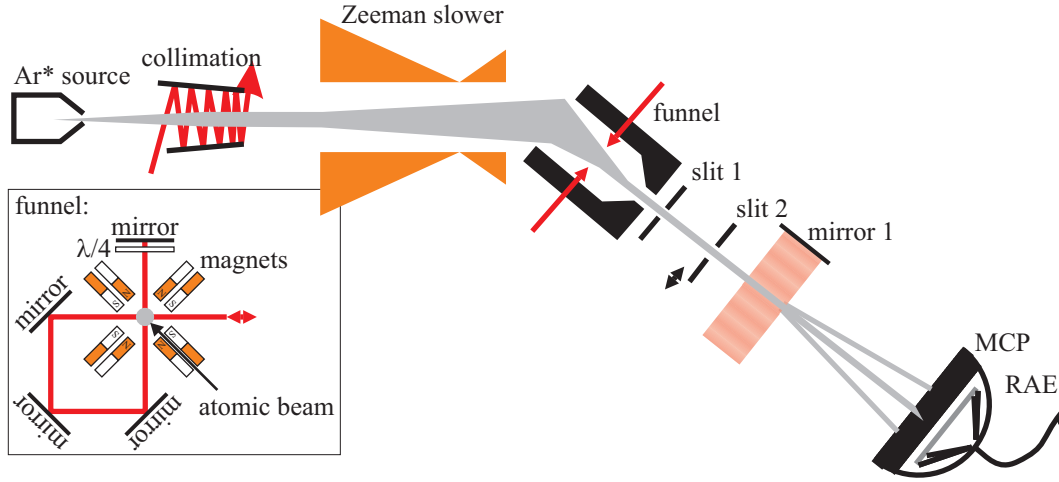


Figure A.2: Sketch of the beam machine. The argon atoms, excited to the metastable state by a gas discharge, pass a first collimation stage, are slowed by a Zeeman slower, collimated by a funnel and two following slits before they enter the experimental setup. The detector follows after a distance of 1m to increase the resolution of the diffraction orders. The inset shows the layout of the funnel.

Zeeman slower

The first unit of the high vacuum part is a σ^\pm Zeeman slower build by Andreas Schnetz [62] reducing the velocity of propagation of the atoms to 42m/s. The magnetic field is generated by two coils, poled contrarily, producing a zero-crossing of the magnetic field. This way huger values of the magnetic field are avoided, that could disturb other parts of the experiment. The final velocity is defined by the maximal value of the magnetic field of the second coil. However with the setup described here the velocity of the atoms can not be reduced further (beyond about 40m/s) by increasing this magnetic field as was verified experimentally. Probably due to the fact that the resonance has a finite width and the magnetic field does not fall to zero abruptly, atoms start turning around and moving back into the Zeeman slower for higher magnetic fields. As the velocity was not measured directly after the Zeeman slower but with the detector at the end of the complete setup, it may also be that the divergence for such a slow beam prevents too many atom to enter the following funnel, so that no atoms are detected in the end.

Funnel

After this main slowing unit the atoms enter a funnel constructed by Martin Störzer and Ralf Stützle [46, 25], whereat the mechanical design follows the design realized by Scholz et al. [63]. This is a 2D-MOT [64] installed under an angle of 42° in respect to the axis atom source - zeeman slower, further reducing the velocity of

the atoms by a factor of $\cos(42^\circ) \approx 0.74$. The angle has the great advantage that atoms not in the state $1s_5$ or UV-photons from the gas discharge will not reach the detector while flying straight on. The funnel is build using four permanent magnets, four mirrors and $\lambda/4$ -plates feeding in only one light beam. A scheme is depicted in the inset of fig. A.2. The cooling mechanism relies on the combination of an optical molasses and an inhomogeneous magnetic field. For the molasses two times two counter propagating laser beams of same polarization and intensity produce a force onto the atoms depending on their velocity, due to the varying Doppler shift. For red detuned light the atomic velocity is damped. For compressing the atomic distribution in real space the magnetic field is added introducing a dependence of the force strength onto the position due to Zeeman-splitting.

Final collimation

The final collimation of the atomic beam is achieved by two slits following the funnel after a few millimeters and some 25cm respectively. They are responsible for the coherence of the atoms necessary for the experiments (cf. sec. 3.1.1).

Directly after the chamber with the experimental setup two permanent magnets outside the vacuum apparatus are installed to remove all atoms not in the substate $m_j = 0$. As a result of the Stern-Gerlach effect they are deflected so that they do not reach the detector. This is to preclude any influences of stray fields.

Detector

The detector composed of two micro-channel plates (MCP), installed at the end of an arm of 1m length following the vacuum chamber with the experimental setup, enables the single atom detection utilizing their inner energy of 12eV. This is combined with a resistive anode following the MCPs, which allows the spatial resolution of the counts in two dimensions. With the distance of the detector from the experimental chamber the separation between the diffraction orders, i.e., their resolution, increases, however the arm has to be slightly lowered as the atoms drop in the terrestrial magnetic field. To increase the resolution the detector unit is installed under an angle of 10° in respect to the axis along the beam propagation. This yields a resolution of $17.2\mu\text{m}$ the total width being 256 pixel on 1in diameter.

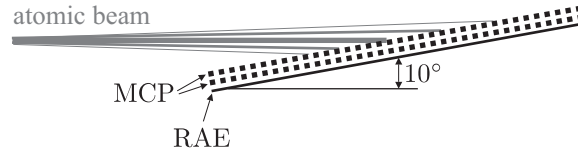


Figure A.3: Atomic beam hitting the detection unit under an angle to increase the resolution.

Laser system

All the light used for the preparation of the atomic beam is provided by a Tapered Amplifier (TA 100, Toptica) emitting light with a wave length of 811.757nm and a power of 400mW. A small part of the intensity is shifted by 18MHz via an acousto optical modulator (AOM) before doing Doppler-free saturation spectroscopy to obtain frequency stabilized light that is red detuned by -18MHz . This is the detuning needed for the funnel. Employing further AOMs the frequency is adapted to the different parts of the preparation process. The light used for the Zeeman slowing is -160MHz red detuned, for the Zeeman slowing and $+6\text{MHz}$ blue detuned for the collimation.

For the double well potential the light is delivered by a titan-sapphire laser (MBR 110, Coherent) pumped by a frequency doubled diode laser (Verdi V10, Coherent). The maximal Power at 811.757nm is 1.5W. As for the light shift potentials it must be far detuned from the intra atomic transition it suffices to stabilize the frequency via the internal reference resonator.

The complex potential is realized with the light of diode laser as stabilized to the resonance frequency of 801.702nm by Doppler-free saturation spectroscopy.

Bibliography

- [1] P. Lambropoulos and D. Petrosyan. *Fundamentals of quantum optics and quantum information*. Springer, Berlin, 2007.
- [2] W. P. Schleich and M. G. Raymer. Special issue on quantum state preparation and measurement. *Journal of Modern Optics*, 44:2021, 1997.
- [3] Louis-Victor de Broglie. *Recherches sur la théorie des quanta*. PhD thesis, Paris, 1924.
- [4] H. Metcalf and P. van Straten. *Laser Cooling and Trapping*. Springer, Berlin [u. a.], 1999.
- [5] M. H. Anderson, J. R. Ensher, M. R. Matthews, C. E. Wieman, and E. A. Cornell. Observation of Bose-Einstein condensation in a dilute atomic vapor. *Science*, 269:198, 1995.
- [6] K. B. Davis, M.-O. Mewes, M. R. Andrews, M. J. Van Druten, D. S. Durfee, D. M. Kurn, and W. Ketterle. Bose-Einstein condensation in a gas of sodium atoms. *Phys. Rev. Lett.*, 75:3969, 1995.
- [7] C.S. Adams, M. Siegel, and J. Mlynek. Atom optics. *Phys. Rep.*, 240:143, 1994.
- [8] F. Hund. Zur Deutung der Molekelspektren III. Bemerkungen über das Schwingungs- und Totationsspektrum bei Molekeln mit mehr als zwei Kernen. *Zeitschrift für Physik A Hadrons and Nuclei*, 43:805, 1927.
- [9] B. D. Josephson. The discovery of tunneling supercurrents. *Review of Modern Physics*, 46:251, 1974.
- [10] M. Albiez, R. Gati, J. Fölling, S. Hunsmann, M. Cristiani, and M.K. Oberthaler. Direct observation of tunneling and nonlinear self-trapping in a single bosonic Josephson junction. *Phys. Rev. Lett.*, 95:010402, 2005.
- [11] J. Clarke and A. I. Braginski, editors. *The SQUID Handbook: Fundamentals and Technology of SQUIDs and SQUID Systems*, volume I. Wiley-VCH, Weinheim, 2004.

- [12] G. Binning and H. Rohrer. Scanning tunneling microscopy. *IBM Journal of Research and Development*, 30:355, 1986.
- [13] D. Devault, J.H. Parkes, and B. Chance. Electron tunneling in cytochromes. *Nature*, 215:642, 1967.
- [14] V. Schünemann. *Biophysik: Eine Einführung*. Springer, Berlin, 2005.
- [15] Steven Chu. Cold atoms and quantum control. *Nature*, 416:206, 2002.
- [16] J. R. Zacharias I. I. Rabi, S. Millman, and P. Kusch. A new method of measuring nuclear magnetic moments. *Physical Review*, 53:318, 1938.
- [17] T. C. Weinacht, J. Ahn, and P. H. Bucksbaum. Controlling the shape of a quantumwavefunction. *Nature*, 379:233, 1999.
- [18] K. M. Fonseca-Romero, S. Kohler, and P. Hänggi. Coherence stabilization of a two-qubit gate by ac fields. *Phys. Ref. Lett.*, 95:140502, 2005.
- [19] edited by W. Domcke, P. Hänggi, and D. Tannor. Driven quantum systems. *Chem. Phys.*, 217:117, 1997.
- [20] F. Grossmann, T. Dittrich, P. Jung, and P. Hänggi. Coherent destruction of tunneling. *Phys. Rev. Lett.*, 647:516, 1991.
- [21] S. Longhi, M. Marangoni, M. Lobino, R. Ramponi, P. Laporta, E. Cianci, and V. Foglietti. Observation of dynamic localization in periodically curved waveguide arrays. *Phys. Rev. Lett.*, 96:243901, 2006.
- [22] G. Della Valle, M. Ornigotti, E. Cianci, V. Foglietti, P. Laporta, and S. Longhi. Visualization of coherent destruction of tunneling in an optical double well system. *Phys. Rev. Lett.*, 98(26):263601, 2007.
- [23] H. Lignier, C. Sias, D. Ciampini, Y. Singh, A. Zenesini, O. Morsch, and E. Arimondo. Dynamical control of matter-wave tunneling in periodic potentials. *Phys. Rev. Lett.*, 99:220403, 2007.
- [24] D. A. Steck, W. H. Oskay, and M. G. Raizen. Observation of chaos-assisted tunneling between islands of stability. *Science*, 293:274, 2001.
- [25] Ralf Stützle. *Nicht zerfließende Wellenpakete in imaginären Potentialen*. PhD thesis, Ruprecht-Karls-Universität Heidelberg, 2006.
- [26] Martin Göbel. *Propagation von Materiewellen in imaginären Potentialen*. Master's thesis, Ruprecht-Karls-Universität Heidelberg, 2004.
- [27] C. Kittel. *Einführung in die Festkörperphysik*. Oldenbourg, München/Wien, 14th edition, 2006.

- [28] V. I. Balykin and V. S. Letokhov. *Atom Optics with Laser Light*. Harwood Academic, Chur, Switzerland, 1995.
- [29] M. K. Oberthaler, R. Abfalterer, S. Bernet, C. Keller, J. Schmiedmayer, and A. Zeilinger. Dynamical diffraction of atomic matter waves by crystals of light. *Phys. Rev. A*, 60:456, 1999.
- [30] A. Turlapov, A. Tonyushkin, and T. Sleator. Optical mask for laser-cooled atoms. *Phys. Rev. A*, 68:023408, 2003.
- [31] K.S. Johnson, J.H. Thywissen, N.H. Dekker, K.K. Berggren, A.P. Chu, R. Younkin, and M. Prentiss. Localization of metastable atom beams with optical standing waves: Nanolithography at the heisenberg limit. *Science*, 280:1583, 1998.
- [32] Craig Scott. *Introduction to Optics and Optical Imaging*. IEEE Press, 1997.
- [33] B. E. A. Saleh and M. C. Teich. *Fundamentals of photonics*. Wiley, New York, 1991.
- [34] P. J. Martin, B. G. Oldaker, A. H. Miklich, and D. E. Pritchard. Bragg scattering of atoms from a standing light wave. *Phys. Rev. Lett.*, 60:515, 1988.
- [35] P. P. Ewald. Zur Begründung der Kristalloptik. Teil I-III. *Annalen der Physik*, 49,54, 1916/17.
- [36] M. Chapman, C.R. Ekstrom, T. Hammond, J. Schmiedmayer, B. Tannian, S. Wehinger, and D.E. Pritchard. Near-field imaging of atom diffraction gratings: The atomic talbot effect. *Phys. Rev. A*, 51:R14, 1995.
- [37] G. Floquet. Sur les équations différentielles linéaires à coefficients périodiques. *Ann. scientifiques de l'Ecole Norm. Sup., deuxième série*, 12:47, 1883.
- [38] F. Grossmann, P. Jung, T. Dittrich, and P. Hänggi. Tunneling in a periodically driven bistable system. *Z. Physik B*, 84:315, 1991.
- [39] T. Dittrich, P. Hänggi, G.-L. Ingold, B. Kramer, G. Schön, and W. Zwerger. *Quantum Transport and Dissipation*. Wiley-VCH, Weinheim, 1998.
- [40] G. P. Agrawal. *Nonlinear Fiber Optics*. Academic Press, San Diego/London, 1995.
- [41] J. J. Sakurai. *Modern quantum mechanics*. Addison-Wesley, Reading, Mass., 1995.
- [42] W. Rossmann. *Lie groups: an introduction through linear groups*. Oxford University Press, Oxford, 2006.
- [43] James Walker. *Fast Fourier Transform*. CRC Press, Inc., Florida, 2nd edition, 1996.

- [44] J. Andruszkov et al. First observation of self-amplified spontaneous emission in a free-electron laser at 109nm wavelength. *Phys. Rev. Lett.*, 85:3825, 2000.
- [45] Mark Csele. *Fundamentals of Light Sources and Lasers*. Wiley-VCH, Weinheim, 1st edition, 2004.
- [46] Martin Störzer. Realisierung eines langsamen, intensiven Strahls metastabiler Argon-atome. Master's thesis, Universität Konstanz, 2003.
- [47] Thomas Hörner. Propagation von Materiewellen in periodischen Doppelpotentialen. Master's thesis, Ruprecht-Karls-Universität Heidelberg, 2005.
- [48] Ramona Ettig. Beobachtung des Tunnelns massiver Teilchen in Doppelpotentialen. Master's thesis, Ruprecht-Karls-Universität Heidelberg, 2006.
- [49] E. D. Palik, editor. *Handbook of Optical Constants of Solids*. Academic Press, New York, 1985.
- [50] Ute Schnorrberger. Tunneln mit Antrieb. Master's thesis, Ruprecht-Karls-Universität Heidelberg, 2006.
- [51] E. Schrödinger. Der stetige Übergang von der Mikro- zur Makromechanik. *Die Naturwissenschaften*, 14:664, 1926.
- [52] J. A. Yeazell, M. Mallalieu, and Jr. C. R. Stroud. Observation of the collapse and revival of a rydberg electronic wave packet. *Phys. Rev. Lett.*, 64:2007, 1990.
- [53] W. P. Schleich. Sculpting a wavepacket. *Nature*, 397:207, 1999.
- [54] M. V. Fedorov, M. A. Efremov, V. P. Yakovlev, and W. P. Schleich. Dynamics of spontaneous radiation of atoms scattered by a resonance standing light wave. *Journal of Experimental and Theoretical Physics*, 97:522, 2003.
- [55] R. Stützle, M.C. Göbel, Th. Hörner, E. Kierig, I. Mourachko, and M.K. Oberthaler. Observation of nonspreading wave packets in an imaginary potential. *Phys. Rev. Lett.*, 95:110405, 2005.
- [56] E. Kierig, U. Schnorrberger, A. Schietinger, J. Tomkovic, and M.K. Oberthaler. Single particle tunneling in strongly driven double well potentials. *Phys. Rev. Lett.*, 100:190405, 2008.
- [57] A. Eckardt, C. Weiss, and M. Holthaus. *Phys. Rev. Lett.*, 95:260404, 2005.
- [58] R. P. Feynman, R. B. Leighton, and M. Sands.
- [59] H. Schanz, M.F. Otto, R. Ketzmerick, and T. Dittrich. Classical and quantum hamiltonian ratchets. *Phys. Rev. Lett.*, 87:070601, 2001.
- [60] J. Kawanaka, K. Shimizu M. Hagiuda, and H. Takuma. Generation of an intense low-velocity metastable-neon atomic beam. *Applied Physics B*, 56:21, 1993.

-
- [61] F. Shimizu, K. Shimizu, and H. Takuma. A high intensity metastable neon trap. *Chemical Physics*, 145:327, 1990.
 - [62] A. Schnetz. *Aufbau und Charakterisierung einer Magneto-Optischen Falle für metastabile Argon-Atome*. PhD thesis, Universität Konstanz, 1995.
 - [63] A. Scholz, M. Christ, D. Doll, J. Ludwig, and W. Ertmer. Magneto-optical preparation of a slow, cold and bright Ne*atomic beam. *Opt. Comm.*, 111:155, 1994.
 - [64] R. Ries, D. S. Weiss, K. A. Moler, and S. Chu. Atom funnel for the production of a slow high-density atomic beam. *Phys. Rev. Lett.*, 64:1658, 1990.

Acknowledgement

During the realization of the presented work, I was collaborating and getting help from many colleagues and friends. To these people I would like to say thank you:

- I would like to thank Markus Oberthaler not only for the opportunity to work on this experiment, even though I had had no great experience in this field of physics before, but primarily for his never ending, catching enthusiasm for physics, which made it a great pleasure to work with him.
- Prof. Dr. Jian-Wei Pan I would like to thank for agreeing to assess this work as a second referee.
- Ralf Stützle, who initiated working on CDT, I want to thank for inducting me into the topic and into all the machine's voodoo and for his never ending willingness to give further explanations long after leaving the university.
- I would like to thank Thomas Hörner, who started at the same time and helped to pester Ralf with questions about the secrets of the argon beam machine.
- Ramona Ettig I would like to thank for helping to endure a hard time of the experiment.
- Special thanks goes to Ute Schnorrberger, who completed the girls camp and did a great job on finally succeeding in coherently controlling stubborn argon atoms. It has been a great time in the lab.
- Special mention and thanks go to Arne Schietinger and Jirka Tomkovic, who made big contributions to the success of the experiment and together with Joachim Welte managed to create a great atmosphere in the lab that made it even harder to leave.
- I also want to thank all the other group members, who contributed substantially to the great atmosphere in the group.
- My parents I would like to thank for their never-ending support.
- Finally I would like to thank Stefan to have put up with me during all stages of this work.